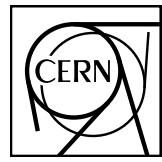


EUROPEAN ORGANIZATION FOR NUCLEAR RESEARCH



June 16, 2017

D-hadron correlations in p-Pb collisions at $\sqrt{s_{\text{NN}}} = 5.02 \text{ TeV}$

F. Colamaria, S. Kumar, M. Mazzilli

Abstract

In this note, we present the analysis of azimuthal correlations of D mesons and primary charged particles performed in the ALICE central barrel in p-Pb collisions at $\sqrt{s_{\text{NN}}} = 5.02 \text{ TeV}$, from 2016 data taking. The analysis is performed in an extended p_T range and with additional observables with respect to p-Pb 2013 data analysis. After a description of the analysis strategy, corrections and systematic uncertainties, the results obtained for prompt D^0 , D^{*+} and D^+ mesons in different ranges of transverse momentum of the D meson and of the associated particles are presented. The results are then compared to Monte Carlo models and also with published 2013 p-Pb analysis results for the common p_T ranges.

1 **Contents**

2	1	Introduction and Motivation	3
3	2	Data/Monte Carlo samples and event selection	4
4	3	Analysis strategy	7
5	3.1	Mass plots and cut optimization	10
6	3.2	Code used for the analysis	14
7	3.3	Further details on corrections	14
8	3.3.1	Event Mixing	14
9	3.3.2	Tracking and D-meson trigger efficiency	18
10	3.3.3	Correction for bias on B to D decay topologies	23
11	3.3.4	Secondary track contamination	28
12	3.3.5	Beauty feed-down	32
13	4	Systematic uncertainties on $\Delta\phi$ correlation distributions	36
14	4.1	Uncertainty on S and B extraction	36
15	4.2	Uncertainty on background correlation shape	36
16	4.3	Uncertainty on D-meson cut stability	40
17	4.4	Uncertainty on tracking efficiency evaluation	40
18	4.5	Uncertainty on secondary particle contamination	44
19	4.6	Uncertainty on feed-down subtraction	45
20	4.7	Uncertainty on correction for the bias on B to D decay topologies	49
21	4.8	Summary table	50
22	5	Results	51
23	5.1	Comparing the three D meson correlation distributions	51
24	5.2	Average of D^0 , D^+ and D^{*+} results	64
25	5.3	Fit observable p_T trends and uncertainties	67
26	5.3.1	Results for near-side yield and width, away-side yield and width, and baseline .	68
27	5.4	Comparison of 2016 p-Pb and 2013 p-Pb results	84
28	5.5	Comparison of 2016 p-Pb and 2010 pp results	84
29	5.6	Comparison of 2016 p-Pb and model expectations	84
30	5.7	Planned results for SQM approvals	84

³¹	6	Bibliography	95
---------------	----------	---------------------	-----------

32 1 Introduction and Motivation

33 The study of the azimuthal correlations of heavy-flavour particles and charged particles at the LHC
 34 energies provides a way to characterize charm production and fragmentation processes in pp collisions.
 35 The measurement also provide a way to probe our understanding of QCD in the perturbative regime,
 36 accessible in a large kinematic range given the large mass of heavy quarks. Flavour conservation in
 37 QCD implies that charm quarks are always produced as pairs of quarks and anti-quarks. The azimuthal
 38 correlations obtained using a meson carrying a heavy quark as trigger particle with the other charged
 39 particles in the same event give the possibility to study the underlying charm production mechanism in
 40 detail. In particular, prompt charm quark-antiquark pair production is back to back in azimuth at first
 41 order in leading-order perturbative-QCD (pQCD). If an hadron from the quark hadronization is taken as
 42 trigger particle, a near-side (at $\Delta\phi = 0$) and an away-side (at $\Delta\phi = \pi$) peak would appear in the azimuthal
 43 correlation distributions, coming from the fragmentation of the quark pair. Heavy quarks produced from
 44 the splitting of a massless gluon can be rather collimated and may generate sprays of hadrons at small
 45 $\Delta\phi$. Finally, for hard-scattering topologies classified as “flavour-excitation”, a charm quark undergoes a
 46 hard interaction from an initial splitting ($g \rightarrow c\bar{c}$), leading to a big separation in rapidity of the hadrons
 47 originating from the antiquark (quark) with respect to the trigger D meson and contribute to a rather flat
 48 term to the $\Delta\phi$ -correlation distribution.

49 Heavy-flavour correlation studies in more complex collision systems, like Pb-Pb, play a crucial role in
 50 studying the modification of the fragmentation of charmed jets due to in-medium (or cold nuclear matter,
 51 in case of p-Pb collisions) effects, in a similar way as it was done for di-hadron correlation studies in
 52 heavy-ion collisions (see for example [1]). Furthermore, the recent observation of long range correlations
 53 in p-Pb for light flavour hadrons ([2], [3]) and for heavy-flavour decay electrons (ALICE preliminary re-
 54 sults) points to possible collective effects or effects originating from gluon saturation in the initial state.
 55 More information could be extracted by the eventual observation of the same effect with D mesons.

56

57 In the following note, we first describe the analysis strategy for the p-Pb 2016 data sample in all its steps,
 58 followed by the list of analysis corrections and the estimation of systematic uncertainties. Finally the
 59 results of $\Delta\phi$ correlations, and quantitative observable extracted to fits to those distributions, obtained for
 60 prompt D^0 , D^+ and D^{*+} in different ranges of transverse momentum for the D-meson (trigger particle)
 61 and the associated particles are presented.

62 The extension of the momentum ranges (both for D mesons and associated particles) with respect to the
 63 2013 p-Pb dataset, as well as the improved precision in the common ranges allow a more thorough inves-
 64 tigation of the charm quark fragmentation properties (multiplicity of tracks as a function of momentum,
 65 geometrical profile of charm jets, p_T distribution of the tracks inside the jet). This can also allow us to
 66 put better constraints on the description of charm fragmentation and charm jet properties provided by
 67 models. The possibility of spotting cold nuclear matter effects affecting the charm fragmentation in p-Pb
 68 was severely limited, in the published paper, by the uncertainties on both pp and p-Pb samples. This will
 69 no longer be the case with the new p-Pb data sample, as soon as a pp sample with equivalent precision
 70 is collected (the pp reference run expected by the end of this year could be of help in this sense). In
 71 addition, the new measurements can be used as solid and precise references in view of an analysis on
 72 a Pb-Pb sample at the same energy (hopefully already in 2018 data taking, otherwise after the ALICE
 73 upgrade).

74 2 Data/Monte Carlo samples and event selection

75 The data samples used for the analyses were the FAST and CENT_woSDD samples from periods LHC16q
 76 and LHC16t (AOD samples). The reason of choosing different types of data samples is explained later
 77 on, in this section. It was verified, by looking at D-meson and associated charged track η and φ distribu-
 78 tions, and at the mixed-event correlation distributions for each subsamples, that no visible differences is
 79 present for the four periods, hence it was possible to perform the analysis directly on the merged samples
 80 without any bias.

81 The Monte Carlo productions adopted for this study were:

- 82 1. LHC17d2a_fast_new, a HIJING production with enrichment of heavy quarks (charm and beauty)
 83 and their decay products in each of the event, performed by PYTHIA6 with Perugia2011 tune,
 84 and with forced hadronic decays of the charmed hadrons. This production was used for D-meson
 85 efficiency evaluation, purity estimation and Monte Carlo closure test.
- 86 2. LHC17f2b_cent_woSDD and LHC17f2b_fast, minimum-bias samples produced with DPMJET
 87 generator, are used for the evaluation of the tracking efficiencies.

88 Table 1 shows the list of runs used for the analysis, for each of the data taking periods, and of the Monte
 89 Carlo productions used to evaluate the corrections:

90 The trigger mask request for the event selection is kINT7. Only events with a reconstructed primary
 91 vertex within 10 cm from the centre of the detector along the beam line are considered. This choice max-
 92 imises the detector coverage of the selected events, considering the longitudinal size of the interaction
 93 region, and the detector pseudorapidity acceptances. In the analysis, the center-of-mass reference frame
 94 of the nucleon-nucleon collision is shifted in rapidity by $y_{NN} = 0.465$ in the proton direction with re-
 95 spect to the laboratory frame, due to the different per-nucleon energies of the proton and the lead beams.
 96 Beam-gas events are removed by offline selections based on the timing information provided by the V0
 97 and the Zero Degree Calorimeters, and the correlation between the number of hits and track segments in
 98 the SPD detector. This is automatically performed in the Physic Selection, a positive outcome of which
 99 is required during our event selection. The pile-up cuts for out-of-bunch pile-up protection are also in-
 100 volved when calling the Physics Selection task. The minimum-bias trigger efficiency is 100% for events
 101 with D mesons with $p_T > 1 \text{ GeV}/c$. For the analyzed data samples, the probability of pile-up from col-
 102 lisions in the same bunch crossing is below 2% per triggered event (in most of the runs, well below 1%).
 103 Events in which more than one primary interaction vertex is reconstructed with the SPD detector (with
 104 minimum of 5 contributors, and a z distance greater than 0.8 cm) are rejected, which effectively removes
 105 the impact of in-bunch pile-up events on the analysis. Out-of-bunch tracks are effectively rejected by the
 106 Physics Selection pile-up cuts, and also by the request of at least one point in the SPD, which has a very
 107 limited time acquisition window (300 ns). Indeed, though the default associated track selection requires
 108 a minimum of 2 points in the ITS, as it will be shown later on full compatibility of the corrected results
 109 with 2 and 3 minimum ITS clusters are obtained. For FAST and CENT_woSDD samples, the latter case
 110 indirectly forces the presence of a point in the SPD.

111 Since data collected during p-Pb 2016 data taking are distinguished into two categories - one including
 112 SDD detector (CENT_wSDD sample) and the second one without the SDD in the reconstruction, or
 113 in the acquisition (CENT_woSDD and FAST samples, respectively), a study of performance of the D-
 114 hadron correlation analysis with respect to the data samples employed has been carried out for D^{*+} and
 115 D^+ mesons (more sensitive to the presence of the SDD w.r.t. the D^0 , due to their reconstruction from
 116 three decay tracks).

117 For this reason, the D-hadron correlation distribution has been compared on LHC16q_pass1_CENT_wSDD
 118 and LHC16q_pass1_CENT_woSDD and the relative statistical uncertainty has been estimated in order to

Type	Production	Run list	nEvents
Monte-Carlo	LHC17d2a_fast_new (c/b enriched), LHC17f2b_fast (MB), LHC17f2b_cent_woSDD (MB)	267166, 267165, 267164, 267163, 265525, 265521, 265501, 265500, 265499, 265435, 265427, 265426, 265425, 265424, 265422, 265421, 265420, 265419, 265388, 265387, 265385, 265384, 265383, 265381, 265378, 265377, 265344, 265343, 265342, 265339, 265338, 265336, 265335, 265334, 265332, 265309 = [36 runs]	50M
Data	LHC16q, pass1_CENT_woSDD	265525, 265521, 265501, 265500, 265499, 265435, 265427, 265426, 265425, 265424, 265422, 265421, 265420, 265419, 265388, 265387, 265385, 265384, 265383, 265381, 265378, 265377, 265344, 265343, 265342, 265339, 265338, 265336, 265335, 265334, 265332, 265309 = [32 runs]	261M total
	LHC16q, pass1_FAST	265525, 265521, 265501, 265500, 265499, 265435, 265427, 265426, 265425, 265424, 265422, 265421, 265420, 265419, 265388, 265387, 265385, 265384, 265383, 265381, 265378, 265377, 265344, 265343, 265342, 265339, 265338, 265336, 265335, 265334, 265332, 265309 = [32 runs]	260M
	LHC16t, pass1_CENT_woSDD	267166, 267165, 267164, 267163 = [4 runs]	40M
	LHC16t, pass1_FAST	267166, 267165, 267164, 267163 = [4 runs]	41M

Table 1: Data Set and Run list

understand if it was better to perform the analysis separately on the two data sample, applying in this case different corrections, or not. In particular, it was crucial for the correlation analysis involving the D^{*+} meson because the track reconstruction efficiency of the soft pion is $\approx 10\%$ higher employing also the SDD information. Figure 1 shows the normalized azimuthal correlation distribution for low, mid and high p_T for D^{*+} meson. Blue points are referred to the woSDD sample while red points represents wSDD data. Figure 2 shows the relative statistical uncertainty extracted from the azimuthal correlation distributions for the D^{*+} in different kinematic ranges.

It can be observed that the data sample that includes the SDD information is characterized by $\approx 10 - 15\%$ more statistics in each p_T ranges analyzed. This difference is related to the larger efficiency in track reconstruction with the wSDD sample - a larger number of tracks survives to the selection request of 3 points in the ITS, which is part of the selection requests applied on the previous D-h analysis.

As a result, the wSDD sample is also affected by a slightly lower relative statistical uncertainty (about 12-15%) due to several reasons: the larger tracking efficiency, the larger number of signal entries in the invariant mass distributions (again an effect of the larger tracking efficiency) and a slight increase of S/B, which reflects in a slight decrease of uncertainty from the sideband subtraction. It has also to be considered that, on the full sample including also the FAST cluster, the increase in performance would be further reduced. The overall statistical uncertainty difference resulting from the comparison is not

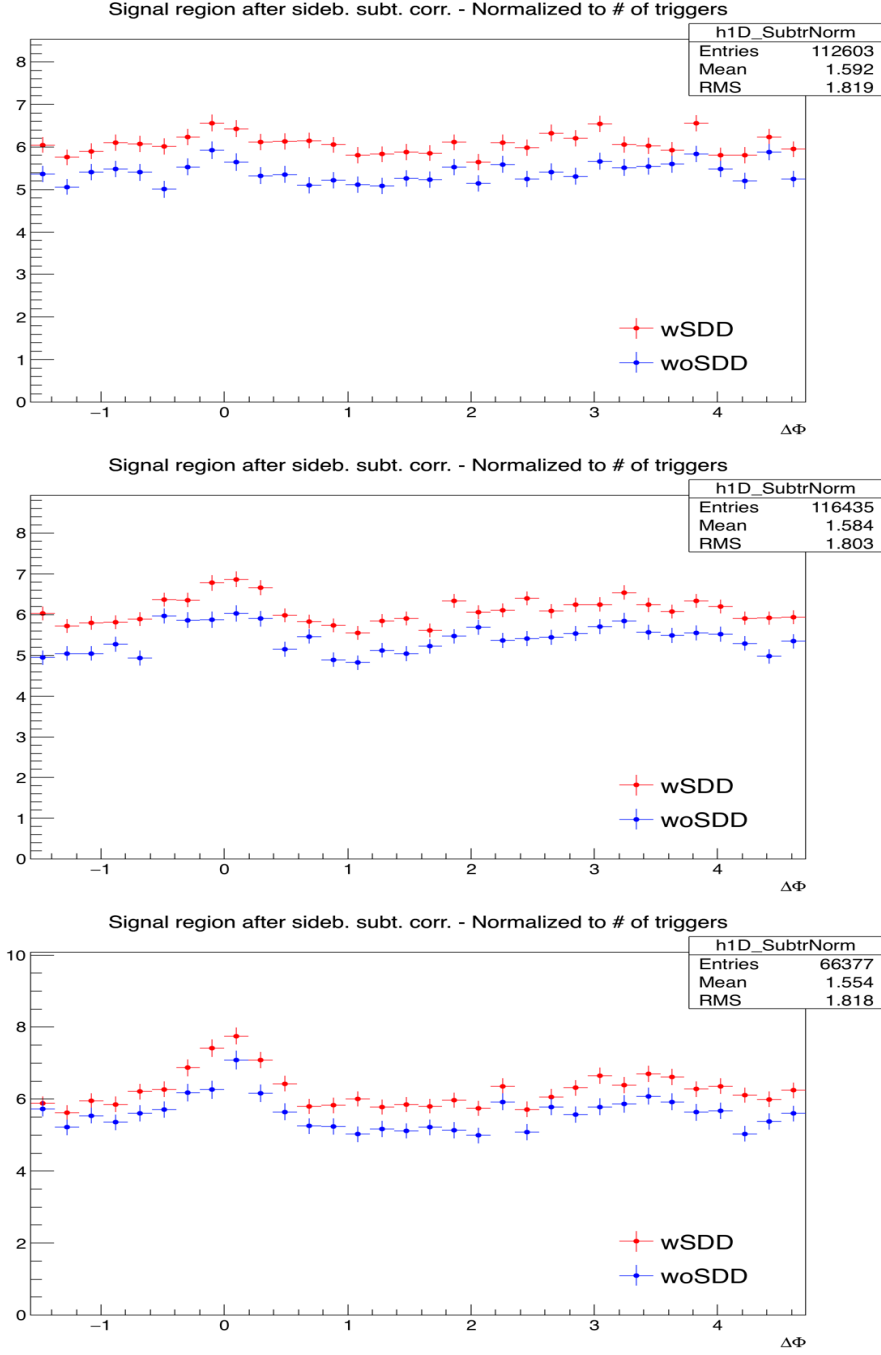


Figure 1: Normalized azimuthal correlation distribution of D^{*+} for low p_T ($3 < p_T(D^{*+}) < 5 \text{ GeV}/c$) on the top panel, mid p_T ($5 < p_T(D^{*+}) < 8 \text{ GeV}/c$) on the middle panel and high p_T ($8 < p_T(D^{*+}) < 16 \text{ GeV}/c$) on the bottom panel with a p_T threshold for associated tracks of $p_T(\text{assoc}) > 0.3 \text{ GeV}/c$. Blue points are referred to the woSDD sample while red points represent wSDD data.

136 enough to justify the implementation of two different analysis and two subsequent different corrections
 137 either for D^{*+} and D^+ .

138 In order to, to cope with the lower tracking efficiency w.r.t. 2013 data sample, after this study, it was
 139 decided to reduce the ITS request for the associated tracks from 3 (used on 2013 data) to 2 ITS clusters
 140 as default selection criterion.

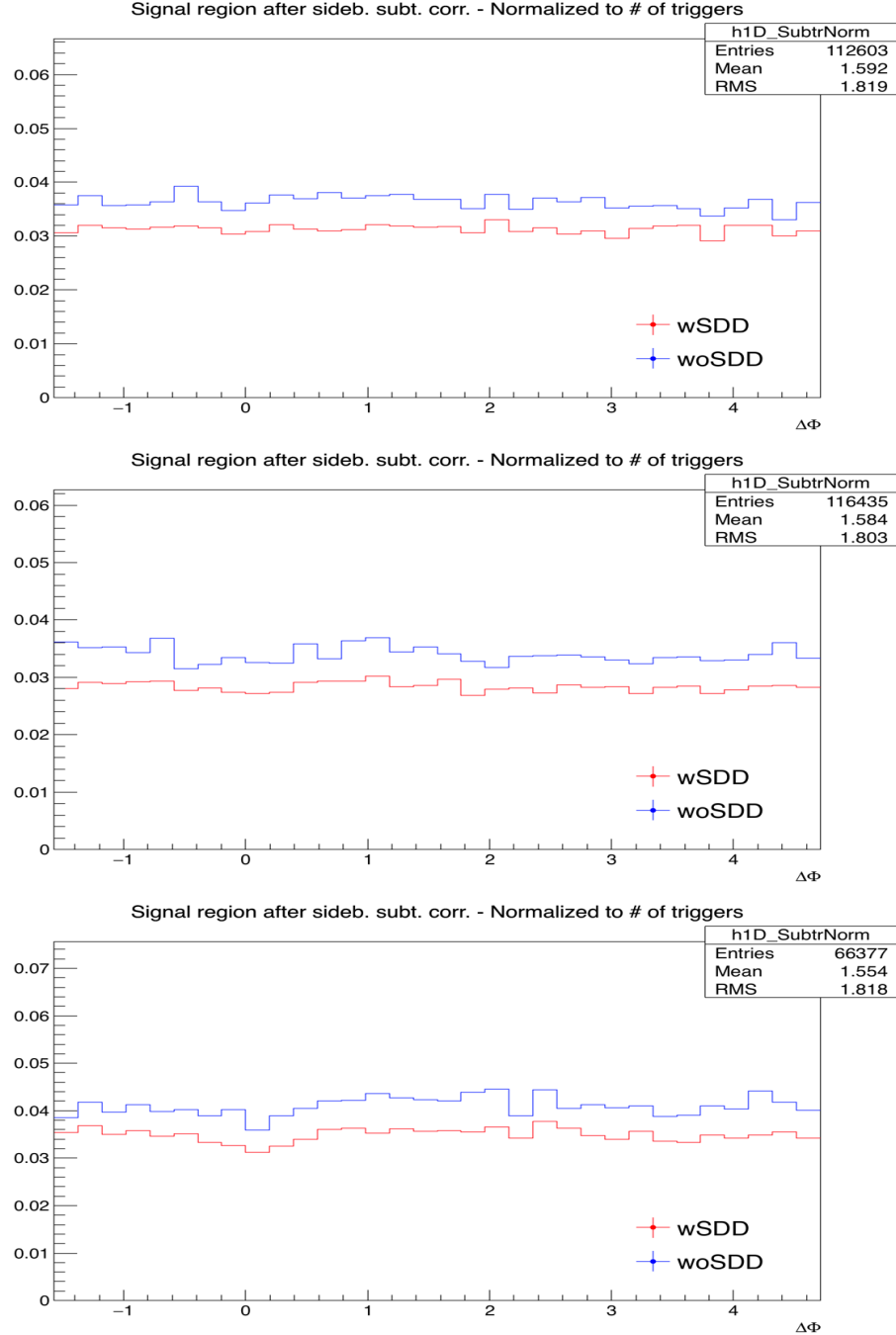


Figure 2: Statistical uncertainty extracted from the azimuthal correlation distribution of D^{*+} with associated charged particles. Top panel: $3 < p_T(D^{*+}) < 5 \text{ GeV}/c$. Mid panel: $5 < p_T(D^{*+}) < 8 \text{ GeV}/c$. Bottom panel: $8 < p_T(D^{*+}) < 16 \text{ GeV}/c$. Blue line is referred to the woSDD sample while the red line represents wSDD data.

141 3 Analysis strategy

142 The analysis follows the same strategy one used in 2013 p-Pb data sample (see published paper [4])
 143 and analysis notes [6], [7]). Correlation pairs are formed by trigger particles (D mesons) reconstructed
 144 and selected in the following p_T^{trig} ranges: $3 < p_T^{\text{trig}} < 5 \text{ GeV}/c$, $5 < p_T^{\text{trig}} < 8 \text{ GeV}/c$, $8 < p_T^{\text{trig}} < 16$
 145 GeV/c , $16 < p_T^{\text{trig}} < 24 \text{ GeV}/c$, and associated particles (charged tracks) for the following p_T^{assoc} re-
 146 gions: $p_T^{\text{assoc}} > 0.3 \text{ GeV}/c$, $0.3 < p_T^{\text{assoc}} < 1 \text{ GeV}/c$, $1 < p_T^{\text{assoc}} < 2 \text{ GeV}/c$, $2 < p_T^{\text{assoc}} < 3 \text{ GeV}/c$,
 147 $p_T^{\text{assoc}} > 3 \text{ GeV}/c$ (with the addition of $p_T^{\text{assoc}} > 1 \text{ GeV}/c$ for comparison with p-Pb 2013 results). In this

148 analysis, the particle identification defines the trigger particle rather than a momentum cut and therefore
 149 the momentum range of the associated particles is not constrained by that of the trigger particle. Our
 150 definition of associated particle includes any charged particle coming from the primary vertex of interac-
 151 tion, including those coming from strong and electromagnetic decay of unstable particles, and particles
 152 deriving from the decay of hadrons with charm or beauty. We therefore include any charged particle
 153 except those coming from weak decays of strange particles and particles produced in the interaction
 154 with the detector material. This definition corresponds to that used in the method AliAODMCParticle::
 155 IsPyphysicalPrimary(). All associated particles surviving the selection cuts and not matching the
 156 adopted criterion are considered as a contamination whose contribution has to be corrected for.

157

158 The analysis is performed through the following steps:

- 159 1. **D meson selection and signal extraction.** For each single event, “trigger” particles are defined
 160 as the selected D meson candidates (D^0 , D^+ and D^{*+}) within a given p_T^{trig} range. The detection
 161 strategy for D mesons at central rapidity is the same performed for the analyses of the D-meson
 162 production at central rapidity [5], and also applied for the D-h analysis on 2010 pp and 2013 p-Pb
 163 samples [4]. It is based on the reconstruction of decay vertices displayed from the primary vertex
 164 by a few hundred μm and on the identification of the decay-particle species. The identification
 165 of the charged kaon and pion in the TPC and TOF detectors is also used, to further reduce the
 166 background at low p_T . An invariant-mass analysis is then used to extract the raw signal yield,
 167 using the same fit functions described in [4]. The D mesons are selected in the rapidity range
 168 varying from $|y| < 0.5$ at low p_T to $|y| < 0.8$ for $p_T > 5 \text{ GeV}/c$.
- 169 2. **Correlation of D candidates with associated tracks.** Particle pairs are formed by correlating each
 170 trigger particle with the charged primary particles passing the track selection (excluding those
 171 coming from the decay of the D-meson candidate) in a specified p_T^{assoc} interval (which can overlap
 172 with the p_T^{trig} range) and in the pseudo-rapidity range $|\eta| < 0.8$. For the D^0 meson, also the low-
 173 momentum pion tracks from feed-down of D^{*+} mesons are removed via 3σ invariant mass cut on
 174 the $M(K\pi\pi) - M(K\pi)$ difference. This because these soft pion are not related to the charm quark
 175 fragmentation chain. For D meson candidates in the invariant mass signal region, defined by a \pm
 176 2σ interval around the D meson mass peak, the azimuthal angle difference $\varphi^{\text{assoc}} - \varphi^{\text{trigg}} \equiv \Delta\varphi$ and
 177 the pseudorapidity difference $\eta^{\text{assoc}} - \eta^{\text{trig}} \equiv \Delta\eta$ are evaluated and stored to build two-dimensional
 178 correlation distribution.
- 179 3. **Correction for limited acceptance and detector inhomogeneities with Event Mixing** The angular
 180 correlation distribution may be affected, even for uncorrelated pair of particles, by structures
 181 not due to physical effects, but originating from the limited detector acceptance, as well as from
 182 angular inhomogeneities in the trigger and track reconstruction efficiencies as a function of $\Delta\varphi$
 183 and $\Delta\eta$. Effects of this kind are removed using the Event Mixing technique. In this technique, the
 184 analysis is executed on the same data sample of the standard one (called “same event” analysis,
 185 SE), but the trigger particles found in each event are correlated to charged particles reconstructed
 186 in different events (“Mixed Events” analysis, ME) with similar characteristic, in particular con-
 187 cerning the event multiplicity and z position of the primary vertex (see Section 3.3.1).

188

189 The differential yield of associated particles per trigger particle is obtained by

$$\frac{1}{N_{\text{trig}}} \frac{d^2N^{\text{pair}}}{d\Delta\eta d\Delta\varphi} = B_{\text{ME}}(0, 0) \times \frac{S(\Delta\eta, \Delta\varphi)}{B_{\text{ME}}(\Delta\eta, \Delta\varphi)}, \quad (1)$$

190 where N^{pair} is the total number of correlated D-hadron pairs. The functions $S(\Delta\eta, \Delta\varphi)$ and $B_{\text{ME}}(\Delta\eta, \Delta\varphi)$
 191 are the signal and the mixed event background distributions, respectively. The later is normalized

192 to its value in $(\Delta\eta, \Delta\phi) = (0, 0)$, i.e. $(B(0, 0))$. Further details on the mixed-event correction are
193 provided in the next section.

194 **4. Subtraction of background correlation from signal distribution.** The invariant mass signal re-
195 gion also includes background D-meson candidates. Their contribution to the raw correlation
196 distribution is subtracted as follows. For each p_T bin, the mean and the sigma of the invariant mass
197 spectrum are extracted. For D^0 and D^+ , a “background” region is defined in the sidebands of the
198 mass distribution as the interval $4 \text{ GeV}/c^2 < |m - m^{\text{pdg}}| < 8 \text{ GeV}/c^2$ (for the D^{*+} meson, only
199 the right sideband is used). The angular correlation distribution for background candidates in this
200 region is extracted and normalized with respect to the background in the signal region estimated
201 from the mass fit. This normalized background correlation distribution is then subtracted from
202 the raw signal one to obtain the signal correlation distribution. The normalization factor is the
203 ratio of the number of background candidates under the signal peak (obtained by integrating the
204 background of the fit function within the signal region) over the number of background candidates
205 in the sidebands (obtained via bin-counting in the sideband region). An example of the signal re-
206 gion, sideband and sideband-subtracted 1D correlation distributions (along $\Delta\phi$) is shown in figure
207 3, together with the comparison of the three distributions after the normalization to the number of
208 triggers.

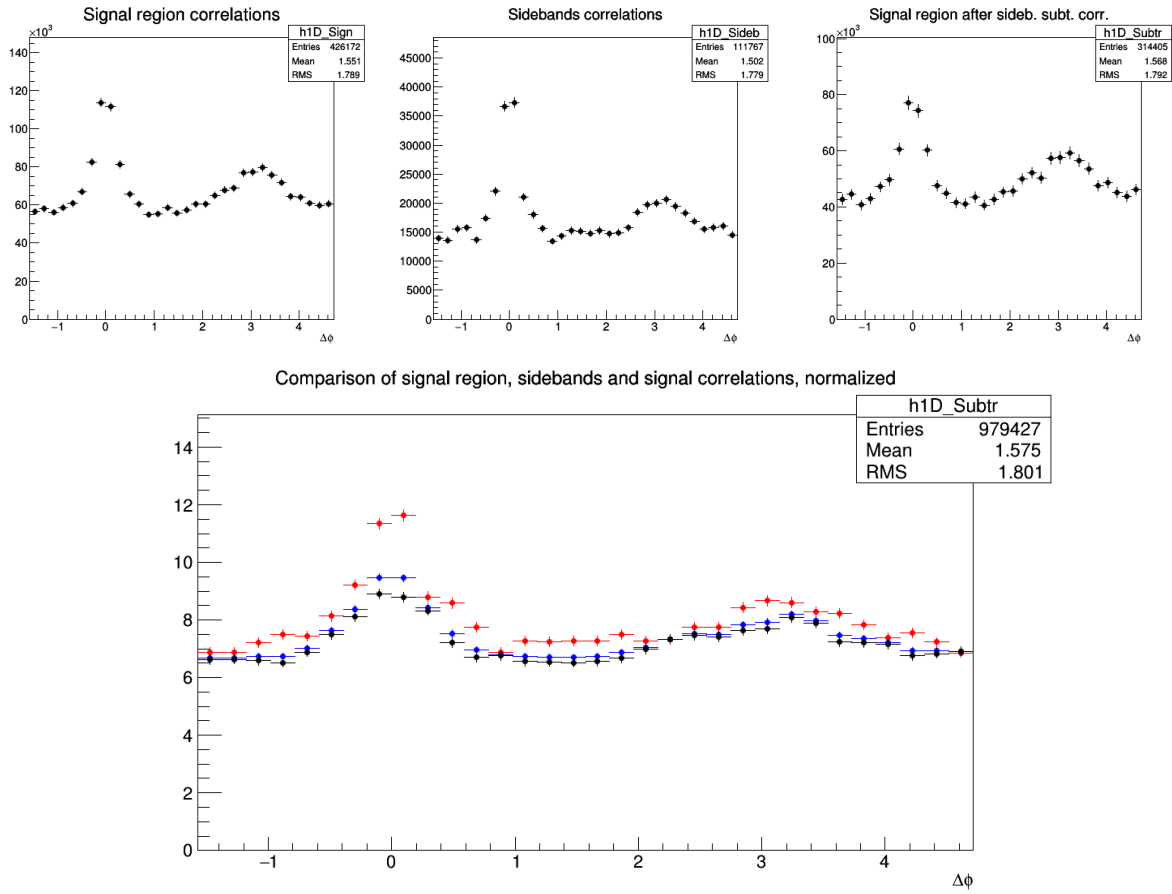


Figure 3: Top: Example of D^0 -h signal region (left), sideband (middle), and signal minus sideband (right) correlation distributions. Bottom: signal region per-trigger normalized correlation distribution (blue), sideband region per-trigger normalized correlation distribution (red), background-subtracted per-trigger normalized correlation distribution (black).

209 **5. Correction for D meson efficiency and associated track efficiency.** After filling the signal and
210 background correlation distributions, it is necessary to take into account also for the correlations

with tracks, those are not reconstructed, or not passing the quality selection due to poor reconstruction. In the same way, the loss of D-mesons which are not reconstructed, or do not pass the selection, impacts the correlation distribution shape. Hence, each pair is weighted by the inverse of the product of the associated track and D meson reconstruction efficiency, ε_{trk} and ε_{trig} . Further details are provided later on in this section.

6. **Projection in $\Delta\varphi$.** The limited statistics available does not allow to study the two dimensional $(\Delta\eta, \Delta\varphi)$ distribution, which is therefore projected to the $\Delta\varphi$ axis by integrating on $|\Delta\eta| < 1$. Despite, in principle, our maximum $\Delta\eta$ acceptance is of $|\Delta\eta| < 1.6$, removing the large $|\Delta\eta|$ regions allow us to reject angular regions with very low statistics, where fluctuations would be amplified by a large mixed-event correction, and avoid the so-called wings effect.

As the difference in the azimuthal angle is periodic ($\Delta\varphi = 0 = 2\pi$), the $\Delta\varphi$ -range is limited to the essential range of 2π . The $\Delta\varphi$ -limits are chosen to be $[-\pi/2, 3\pi/2]$ in order to provide a good visibility of the correlation pattern, which peaks around 0 and π .

7. **Correction for the contamination of secondary particles** The DCA to primary vertex cut, applied during the associated track selection, has the role of removing the secondary particles from the associated track sample. Secondary particles are indeed produced either from long-lived strange hadrons or from interaction of particles with the detector material. A residual contamination from secondary tracks is hence expected in the correlation distributions. This contamination is estimated from Monte Carlo simulation based on Pythia as described more in detail in the next section. The background-subtracted event-mixing corrected correlations are multiplied by a purity factor to encounter this contribution.

8. **Correction for bias on B to D decay topologies** The presence of the topological cuts for the D-meson selection indirectly induce a bias on the topology of the B to D decay topologies, favouring cases with a small opening angle between the D-meson and the other tracks from the B decay. This affects the feed-down component of the data correlation distributions. This effect is corrected for with a procedure described in the subsection 3.3.3. Note that this correction is a novelty with respect to the previous analyses, where only a quite conservative systematic uncertainty was applied to take into account this effect.

9. **Correction for feed-down of D meson from b-hadron decay** The selection strategy employed for the D meson candidates selection enhances the fraction of reconstructed D mesons coming from the decay of a b-hadron. Typical values, with the cuts used for the D-meson selection, are of the order of 10% or less. The correlation distribution of these secondary D mesons will be sensitive to the properties of beauty jets and beauty hadron decay, which in general differ from those relative to charm jets and hadrons. The procedure used to subtract this contribution is described in the next paragraphs of this section.

10. **Study of correlation properties.** The properties of the azimuthal correlation distribution are quantified by fitting the distribution with a function composed of two Gaussian functions, modelling the near and the away side peaks, and a constant term describing the baseline. The mean of the Gaussian are fixed at $\Delta\varphi = 0$ and $\Delta\varphi = \pi$. To accomplish the 2π periodicity of the $\Delta\varphi$ variable, the Gaussian functions are “duplicated” with mean at $\Delta\varphi = 2\pi$ and $\Delta\varphi = -\pi$. The fitting procedure is described in details in Section 5.

3.1 Mass plots and cut optimization

The invariant mass distributions of D^0 , D^{*+} and D^+ in the various pt ranges are shown in Figure 4, 5 and 6 respectively. Note that the distributions are weighted by the D-meson selection and reconstruction efficiency, to allow a correct normalization of the correlation distributions, which have also these weights.

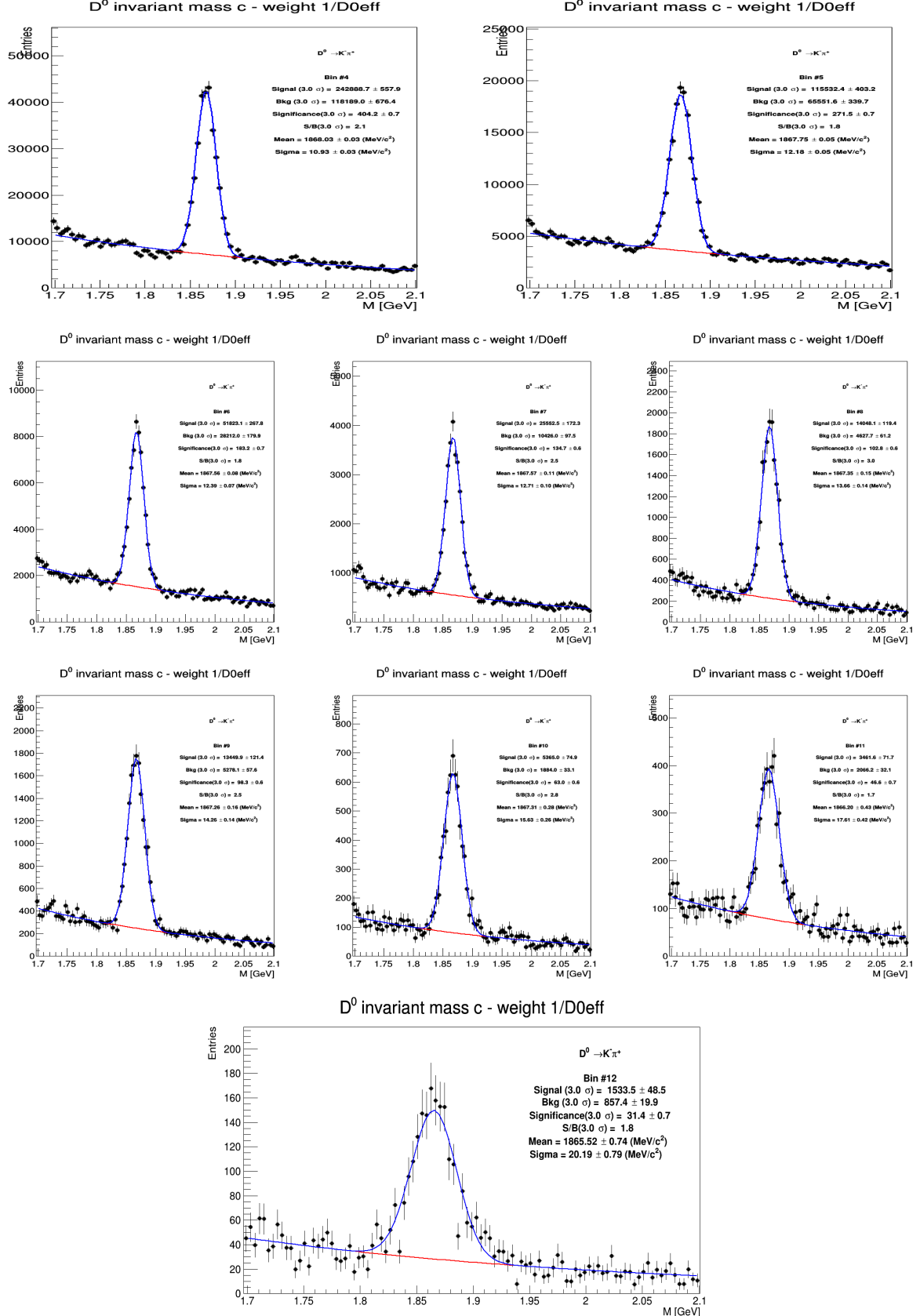


Figure 4: Invariant mass distributions of D^0 corrected with efficiency in different p_T regions. Top: $3 < p_T^D < 4 \text{ GeV}/c$ (left), $4 < p_T^D < 5 \text{ GeV}/c$ right), Mid 1: $5 < p_T^D < 6 \text{ GeV}/c$ (left), $6 < p_T^D < 7 \text{ GeV}/c$ (middle), $7 < p_T^D < 8 \text{ GeV}/c$ (right); Mid2: $8 < p_T^D < 10 \text{ GeV}/c$, $10 < p_T^D < 12 \text{ GeV}/c$ (middle), $12 < p_T^D < 16 \text{ GeV}/c$ (right) and Bottom: $16 < p_T^D < 24 \text{ GeV}/c$.

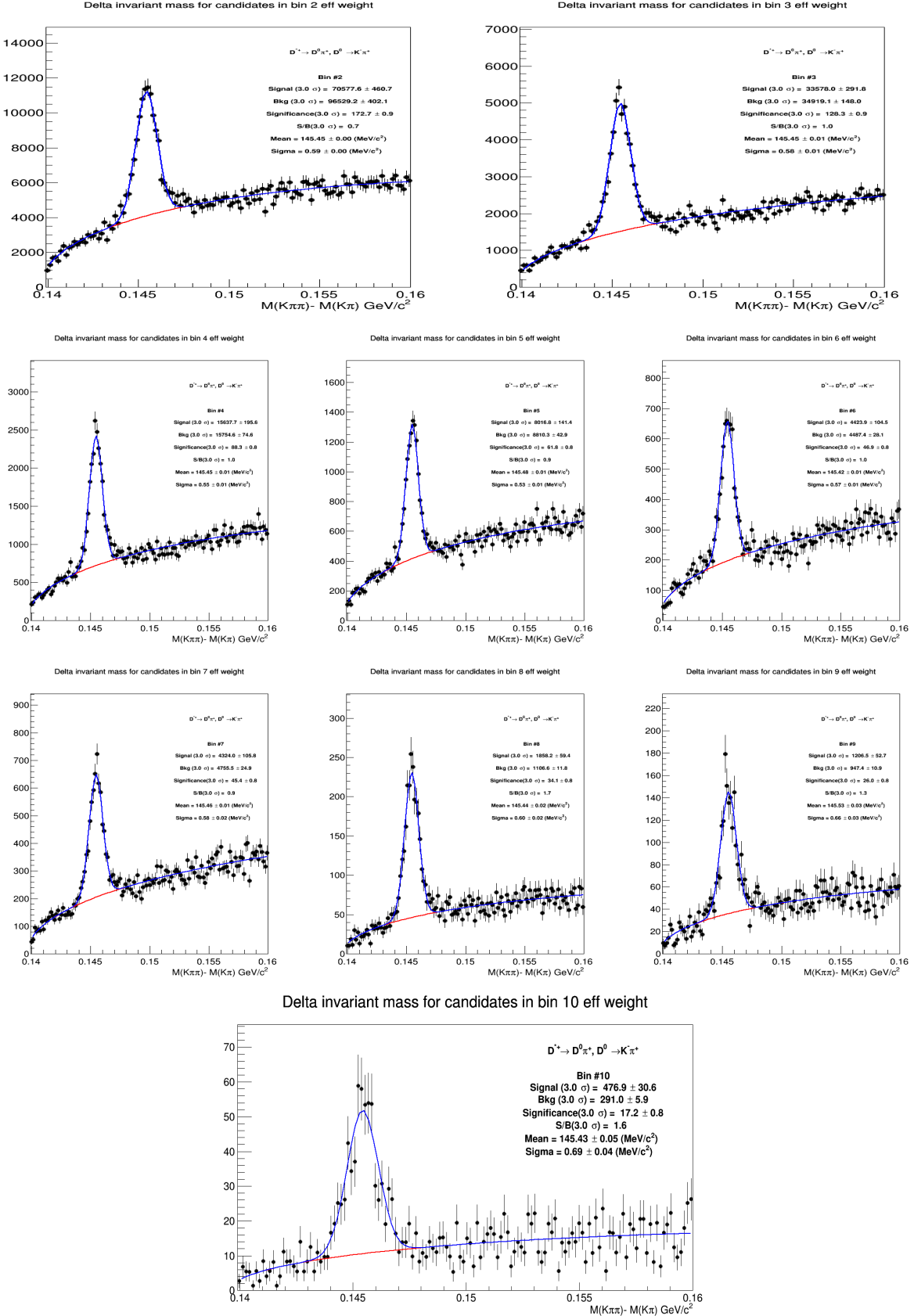


Figure 5: Invariant mass distributions of D^{*+} corrected with efficiency in different p_T regions. Top: $3 < p_T^D < 4$ GeV/c (left), $4 < p_T^D < 5$ GeV/c (right), Mid 1: $5 < p_T^D < 6$ GeV/c (left), $6 < p_T^D < 7$ GeV/c (middle), $7 < p_T^D < 8$ GeV/c (right); Mid 2: $8 < p_T^D < 10$ GeV/c, $10 < p_T^D < 12$ GeV/c (middle), $12 < p_T^D < 16$ GeV/c (right) and Bottom: $16 < p_T^D < 24$ GeV/c .

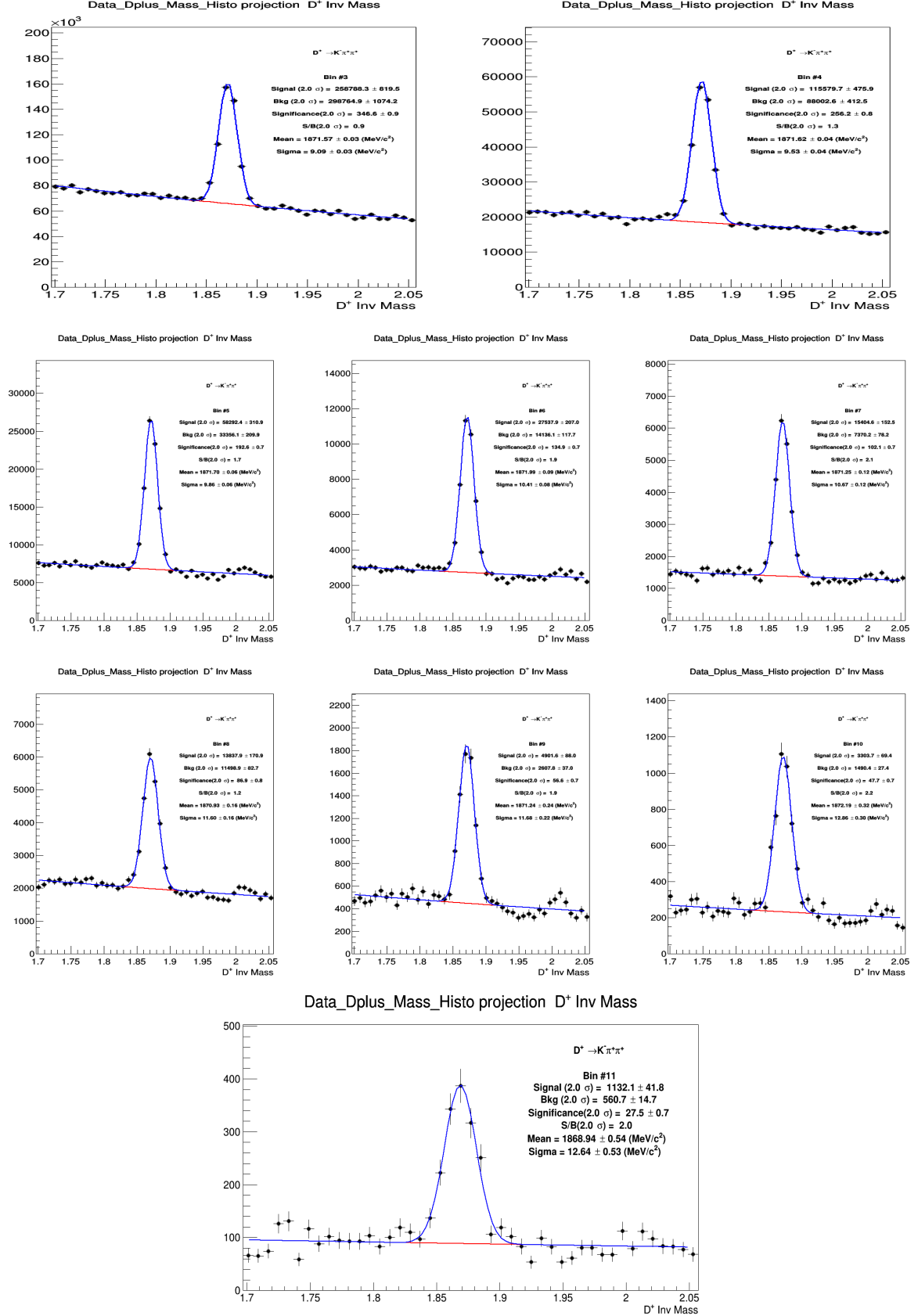


Figure 6: Invariant mass distribution of D⁺ corrected with efficiency in different p_T regions. Top: 3 < p_T^D < 4 GeV/c (left), 4 < p_T^D < 5 GeV/c (right), Mid 1: 5 < p_T^D < 6 GeV/c (left), 6 < p_T^D < 7 GeV/c (middle), 7 < p_T^D < 8 GeV/c (right); Mid2: 8 < p_T^D < 10 GeV/c, 10 < p_T^D < 12 GeV/c (middle), 12 < p_T^D < 16 GeV/c (right) and Bottom: 16 < p_T^D < 24 GeV/c .

For D^{*+} , the standard D2H p-Pb cuts (for the 2013 cross section analysis, [8]) were used. The same holds for the D^+ , but with the addition of cuts on the normalized decay length in xy plane and of the normalized difference between measured and expected daughter track impact parameters (topomatic cut). A particular cut optimization was instead performed for the D^0 meson. Twelve cut sets were tried, with the goal of increasing the S/B factor, in order to reduce fluctuations induced by the sideband subtraction (the limiting factor for the analysis performance). In Figure 7 the D^0 -h correlation distributions are shown for the different cut sets, in exemplary kinematic regions (left column), together with the bin-by-bin relative statistical uncertainty on the data points (right column). The best cut set (option G) was defined from the standard cuts used for the p-Pb 2013 cross section analysis, with a tightened selection on the cosine of the pointing angle, and with the addition of a cut on the normalized decay length in xy plane and of a selection on the normalized difference between measured and expected daughter track impact parameters (topomatic cut).

3.2 Code used for the analysis

The code used for D meson-hadron correlation analysis is fully committed in AliPhysics. The analysis classes can be found in `$ALICE_ROOT/PWGHF/correlationHF/`. The D meson specific classes where the aforementioned steps are carried out are `AliAnalysisTaskDStarCorrelations`, `AliAnalysisTaskSED0Correlations` and `AliAnalysisTaskDplusCorrelations`. The classes which are common to the D meson specific analysis which includes the associated particle cuts and the correlation observables are `AliiHFAssociatedTrackCuts`, `AliHFCorrelator`, `AliHFOfflineCorrelator`, `AliReducedParticle` and `AliDhCorrelationExtraction`. Several additional classes and macros in the same folder deal with the correction steps.

The final results presented here are extracted are the HFCJ pPb (n. 88) train runs 254-257 (for D^0 and D^+) and 268-271 (for D^{*+}).

3.3 Further details on corrections

3.3.1 Event Mixing

The event-mixing technique is used for correcting the raw correlation distribution for effects arising from the detector limited acceptance in rapidity and detector spatial inhomogeneities. The calculation of the Event Mixing correlation distribution is performed online. An event pool is created, where events preceding the one containing a D candidate are stored based on their properties (position of the vertex along the z axis and multiplicity). Each time a D meson candidate is found in an event, only the events contained in the same pool as the event under analysis is used to evaluate the correlations for the event mixing correction.

For D^0 and D^+ , an offline approach for the mixed-event correction has been developed. In this approach, D-meson triggers and associated tracks from every analyzed event are stored in dedicated TTree, together with the needed kinematic information to build correlation distributions, and with identifiers of the events to which they belong. In this way, it is possible to correlate each D meson with all the tracks belonging to the same pool over the full event sample, and not being limited to the same subjob as for the online analysis. This allows to increase the statistics of the mixed-event correlation distributions. It was verified that online and offline approaches are fully compatible within the statistical uncertainties.

The multiplicity and z vertex position bins for the pools used in the p-Pb analysis (for both approaches) are the following:

- Multiplicity bins: $(0, 35); (35, 55); (55, +\infty)$
- Vertex z (cm) = $(-10, -1.5); (-1.5, 3.5); (3.5, 10)$

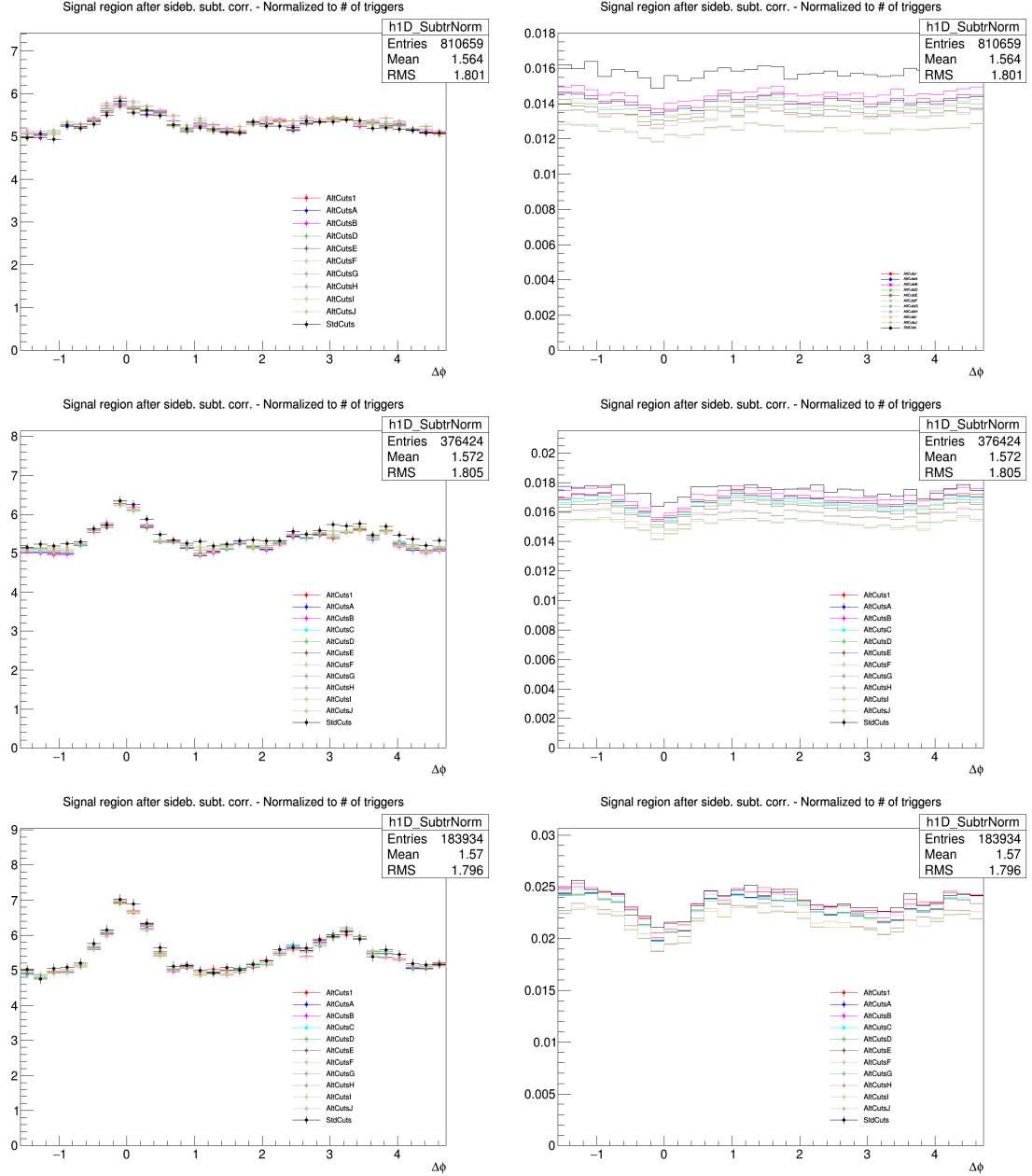


Figure 7: D^0 - h correlation distributions with different cut options (left) and point-by-point relative statistical uncertainty (right) for $3 < p_T^D < 5 \text{ GeV}/c$ (top), $5 < p_T^D < 8 \text{ GeV}/c$ (middle), $8 < p_T^D < 16 \text{ GeV}/c$ (bottom), in all cases with associated track $p_T > 0.3 \text{ GeV}/c$.

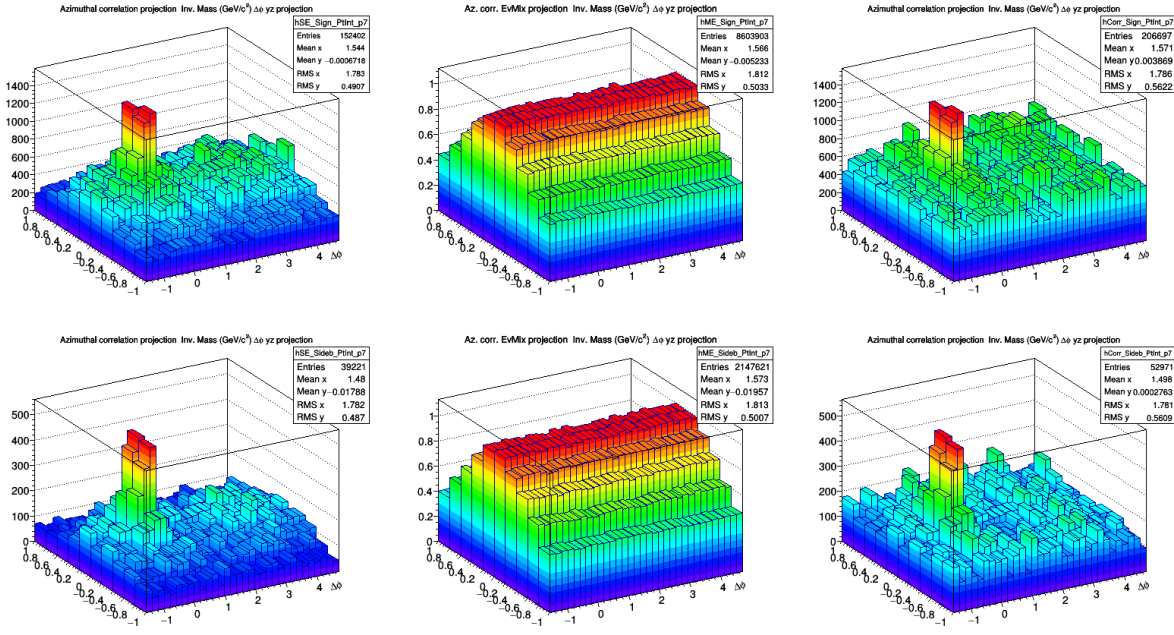


Figure 8: D^0 meson ($\Delta\varphi$, $\Delta\eta$) correlation for in the signal region (top row) and sidebands (bottom row) from Single Event (left) and Mixed Event analysis (center) for high p_T : $8 < p_T < 16$ GeV/c with associated $p_T > 0.3$ GeV/c. The right column shows the SE/ME corrected distributions.

299 In an ideal case, the mixed event distribution is expected to have a constant flat distribution as function
300 of $\Delta\varphi$ and a triangular shaped distribution in $\Delta\eta$ deriving from the limited η acceptance of the detector.
301 In case, instead of detector inefficient regions, or holes, in the same angular position for D meson and
302 associated tracks, these structures produce an excess of correlations at $\Delta\varphi = 0$ in the $\Delta\varphi$ distribution. The
303 obtained distribution is used as a weight in each correlation bin, i.e, the corrected correlation distribution
304 is calculated as follows:

$$\frac{dN^{corr}(\Delta\varphi\Delta\eta)}{d\Delta\varphi d\Delta\eta} = \frac{\frac{dN^{SE}(\Delta\varphi\Delta\eta)}{d\Delta\varphi d\Delta\eta}}{\frac{dN^{ME}(\Delta\varphi\Delta\eta)}{d\Delta\varphi d\Delta\eta}} \frac{dN^{ME}(0,0)}{d\Delta\varphi d\Delta\eta} \quad (2)$$

305 In Eq.2, the last term stands for the average of the bins in the region $-0.2 < \Delta\eta < 0.2$, $-0.2 < \Delta\varphi < 0.2$
306 (multiple bins are used to minimize the effect of statistical fluctuations on the normalization of the mixed-
307 event plots). This kind of normalization, adopted in the analysis of hadron-hadron correlations, relies
308 on the fact that at $(\Delta\eta, \Delta\varphi) = (0,0)$ the trigger and associated particle experience the same detector
309 effects. In the D meson case this is true only on average and not at very low p_T , since D mesons are
310 reconstructed from particles that can go in different detector region. However, $(\Delta\eta, \Delta\varphi) = (0,0)$ is in
311 any case the region with maximum efficiency for the pairs (both correlated and uncorrelated). Thus the
312 same convention was adopted.

313 The mixed-event correlation distributions are built in both D meson signal and sideband regions. Both
314 are corrected with the relative distributions. An example of the mixed-event distributions, and of the
315 outcome of the mixed-event correction, is provided in Figures 8 and 9. The expected triangular shape
316 in $\Delta\eta$, for the mixed-event distributions, addresses the effect of the limited detector pseudo-rapidity
317 acceptance. Note that the mixed-event distribution is limited to the interval $|\Delta\eta| < 1$: the decision to
318 limit the mixed-event correction, and thus the whole analysis, to this range was taken in order to avoid
319 the so-called “wing effect”, i.e. the wing-like structures arising in the correlation distribution at large $\Delta\eta$
320 due to the limited filling of the correlation bins in that region.

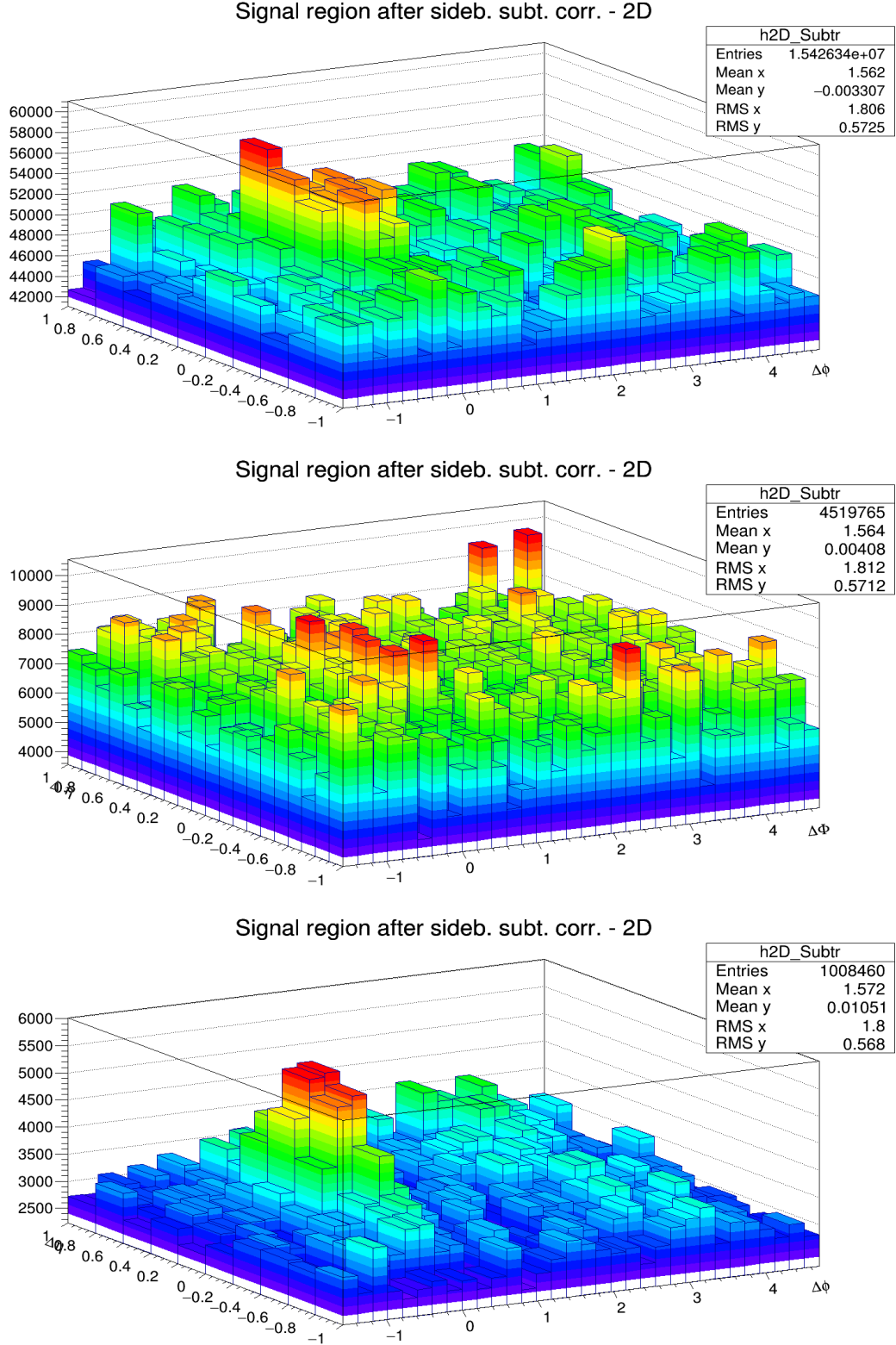


Figure 9: Top: $(\Delta\phi, \Delta\eta)$ correlation distribution of D^0 -h with $3 < p_T < 5$ GeV/c and associated track kinematic range: $0.3 < p_T < 1.0$ GeV/c Mid: $(\Delta\phi, \Delta\eta)$ correlation distribution of D^{*+} -h with $3 < p_T < 5$ GeV/c and associated track p_T Threshold: $p_T > 0.3$ GeV/c Bottom: $(\Delta\phi, \Delta\eta)$ correlation distribution of D^+ -h with $8 < p_T < 16$ GeV/c and associated track p_T threshold: $p_T > 0.3$ GeV/c. All the plots are shown after the mixed-event correction and the sideband subtraction.

321 **3.3.2 Tracking and D-meson trigger efficiency**

322 **(i) Tracking efficiency** - The tracking efficiency was calculated by obtaining the ratio between the yield
 323 at the reconstructed level and generated level, for a defined “type” of particles (in our case non-identified
 324 particles) and it is estimated differentially in p_T , η , and z_{vtx} of the charged particles.

325
 326 Tracking efficiency maps were produced as TH3D histograms (p_T , η , z_{vtx}) obtained from MC analysis on
 327 the minimum-bias samples LHC17f2b_fast and LHC17f2b_cent_woSDD, and applying at reconstructed
 328 level the track selections (summarized in Table. 2). These efficiency maps were used in the analysis
 329 tasks to extract single track efficiencies; each correlation pairs found in the data analysis was inserted in
 330 correlation plots with a weight of **1/efficiency value**. Example plots of the p_T dependence of the tracking
 331 efficiency for two different track selections (the standard on top, a tighter selection used for systematics
 332 on bottom) are shown in Fig. 10.

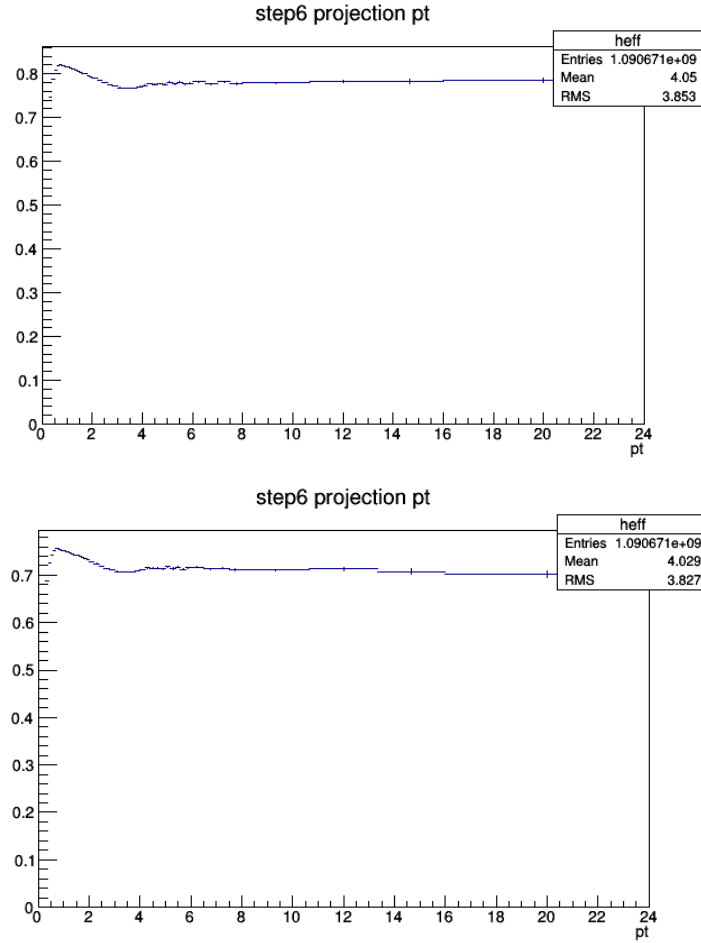


Figure 10: p_T efficiency map for standard track selection (2 ITS clusters) on top panel, and alternate track selection, used for systematics (3 ITS clusters, filterbit4, ITS refit) on bottom panel.

³³³ Details of cuts at event level and particle/track selection at different steps are listed in Table 2.

MC Generated	
Stages	Cuts
1. MC Part with Generated Cuts	After Event Selection Charge PDG Code Physical Primary Kinematics Cuts $-0.8 < \eta < 0.8$ $p_T > 0.3$ (GeV/c)
2. MC Part with Kine Cuts	
MC Reconstructed	
4. Reco tracks	After Event Selection Physical Primary Kinematics Cuts $-0.8 < \eta < 0.8$ $p_T > 0.3$ (GeV/c)
5. Reco tracks with Kine Cuts	
6. MC true with Quality Cuts	Quality Cuts SetRequireSigmaToVertex(kFALSE) SetDCAToVertex2D(kFALSE) SetMinNCrossedRowsTPC(70) SetMinRatioCrossedRowsOverFindableClustersTPC(0.8) SetMinNClustersITS(2) SetMaxChi2PerClusterTPC(4) SetMaxDCAToVertexZ(1) SetMaxDCAToVertexXY(1) SetRequireTPCRefit(TRUE) SetRequireITSRefit(FALSE) Same as step 6
7. Reco tracks with Quality Cuts	

Table 2: The list of event and particle/track selection cuts used in the estimation of single track efficiency

³³⁴

³³⁵ **(ii) D meson efficiency** - Due to limited statistics, the correlation analysis is performed in quite wide p_T bins and in each of them the reconstruction and selection efficiency of D mesons is not flat, in particular in the lower p_T region. We correct for the p_T dependence of the trigger efficiency within each p_T -bin.

³³⁸ This correction is applied online, by using a map of D meson efficiency as a function of p_T and event ³³⁹ multiplicity (in terms of SPD tracklets in $|\eta| < 1$) extracted from the enriched Monte Carlo sample ³⁴⁰ LHC17d2a_fast_new. The η dependence was neglected due to the statistics of the available Monte Carlo ³⁴¹ sample, which rule out the possibility of performing a 3D study.

³⁴² To properly count the number of trigger particles used to normalize the correlation distributions, N_{trig} , ³⁴³ each D meson is weighted with the inverse of its efficiency in the invariant mass distribution. The main ³⁴⁴ role of the correction for the D meson efficiency is to account for the p_T dependence of the correlation ³⁴⁵ distribution within a given D meson p_T interval. Indeed, only the p_T shape of the D meson efficiency ³⁴⁶ within the correlation p_T^{trig} ranges is relevant while the average value in the p_T range is simplified due to ³⁴⁷ the normalization of the correlation distribution to the number of trigger particles.

348 Efficiency plots for D^0 , D^+ and D^{*+} mesons are shown in Figs. 11 and 12.

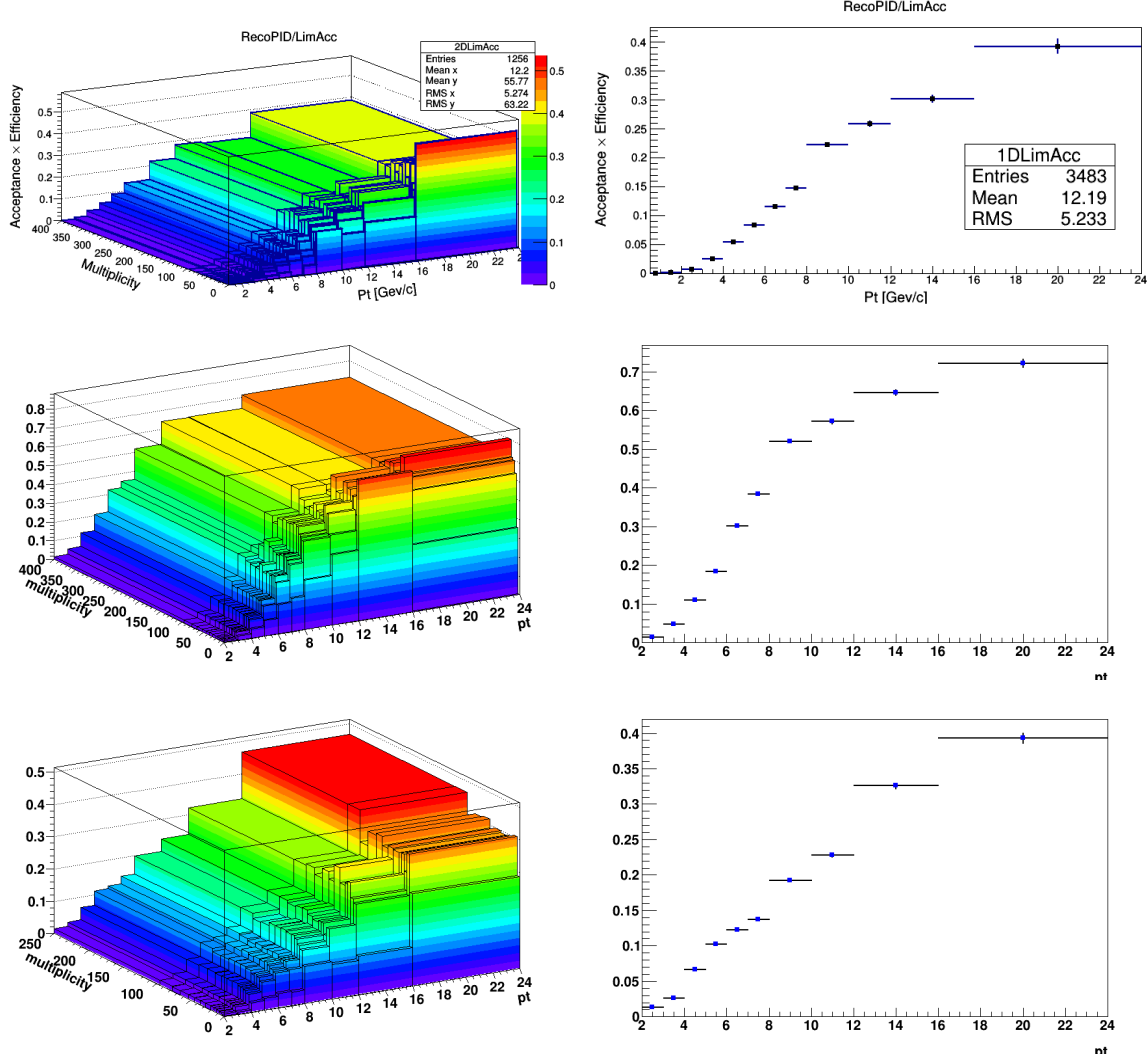


Figure 11: Top panel: (p_T , multiplicity) dependence (left) and p_T dependence (right) of prompt D^+ meson efficiency. Mid panel: (p_T , multiplicity) dependence (left) and p_T dependence (right) of prompt D^{*+} meson efficiency. Bottom panel: (p_T , multiplicity) dependence (left) and p_T dependence (right) of prompt D^0 meson efficiency.

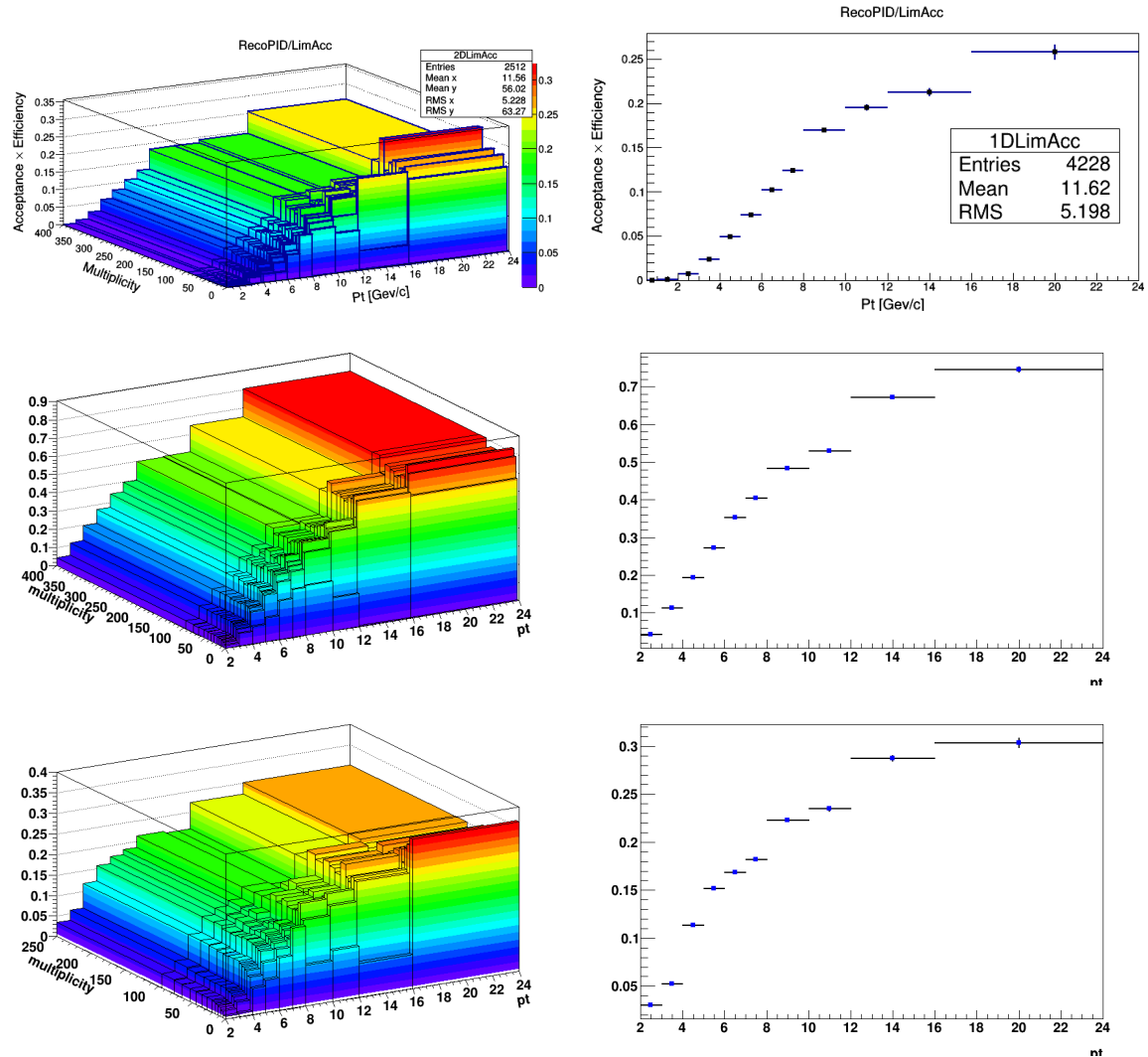


Figure 12: Top panel: (p_T , multiplicity) dependence (left) and p_T dependence (right) of feed-down D^+ meson efficiency. Mid panel: (p_T , multiplicity) dependence (left) and p_T dependence (right) of feed-down D^{*+} meson efficiency. Bottom panel: (p_T , multiplicity) dependence (left) and p_T dependence (right) of feed-down D^0 meson efficiency.

349 It was observed that multiplicity dependence of the efficiency does not bias the extraction of the signal
 350 yield from the invariant mass distributions (which, as anticipated, are also weighted in the same manner).
 351 In addition, the multiplicity dependence of the efficiencies (shown for the D^0 , in integrated p_T range, in
 352 Fig. 13) is rather flat in the range 20-80 tracklets, where about 90% of the reconstructed D -mesons are
 found, which explains why it has a negligible effect on the correlation distributions on this data sample.

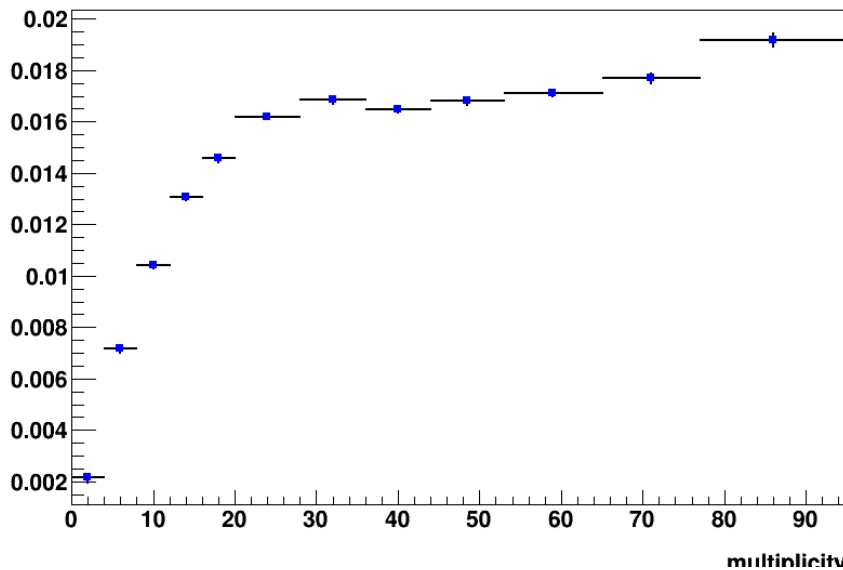


Figure 13: Prompt D^0 meson efficiency as a function of multiplicity (SPD tracklet in $|\eta| < 1$).

354 3.3.3 Correction for bias on B to D decay topologies

355 To verify the consistency of the analysis chain and of the corrections applied to the correlation distributions extracted from data, a Monte Carlo closure test was setup and tried on the D^0 - h analysis.

357 On the Monte Carlo enriched with charm and beauty quarks (LHC17d2a_fast_new), the correlation analysis was performed both at kinematic level and at reconstructed level. At kinematic level, only acceptance

358 cuts were applied on the D mesons and the associated particles, using the Monte Carlo information for

359 the identification of the D mesons and the hadrons in the event and rejecting the non-primary particles.

361 At reconstructed level, the analysis was performed as if it were executed on data, applying the event se-

362 lection, the acceptance cuts for D mesons and the associated particles, selecting the D meson candidates

363 with filtering cuts on their daughters, topological cuts and PID selection, and then keeping only the true

364 D mesons by matching with the Monte Carlo truth; non-primary particles were rejected by means of

365 the DCA selection. Event mixing correction was applied both at reconstructed and at kinematic level,

366 where it takes into account just the effects of the acceptance cuts. In addition, at reconstructed level, the

367 efficiency corrections for D mesons and associated tracks were also applied.

368 Examples of correlation plots at both steps are shown in Figures 14 and 15, separating the correlation

369 contribution of associated tracks and D mesons from different origins, as described in the legend of the

370 plots.

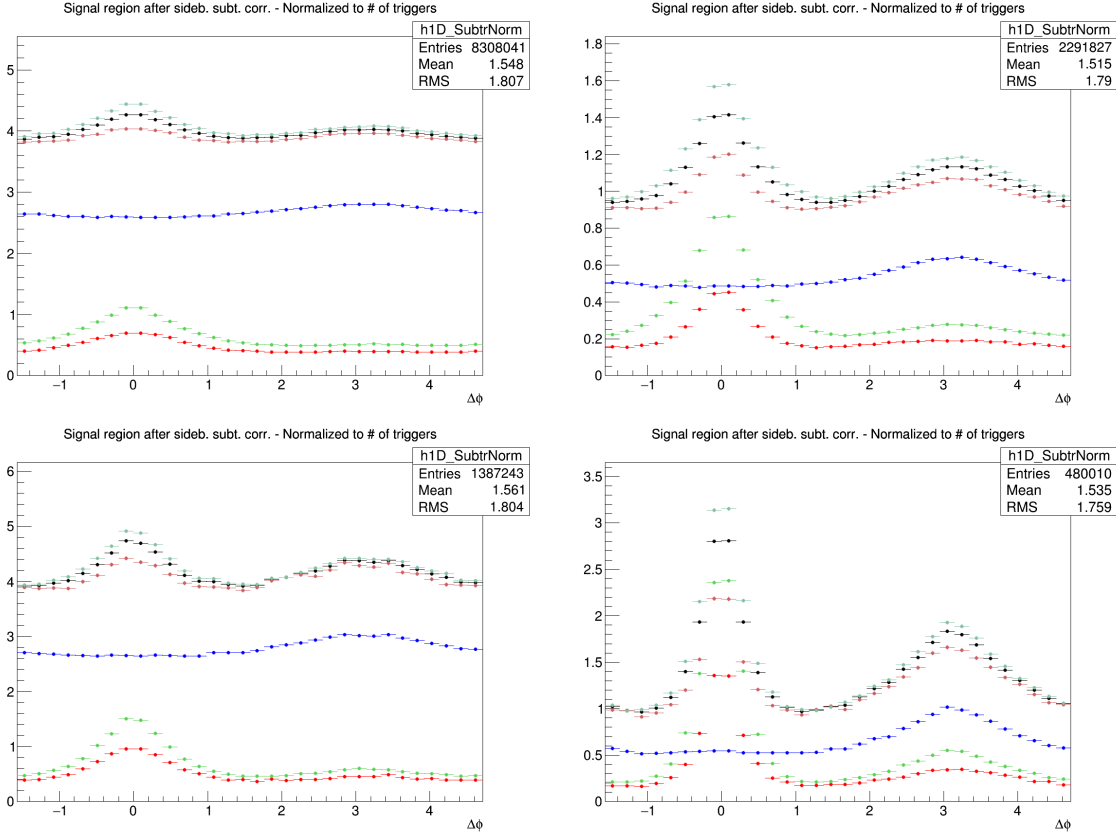


Figure 14: D^0 -hadrons azimuthal correlation distribution obtained from Monte Carlo, at kinematic step. Black points: All D^0 -all hadrons, normalized by all D^0 triggers; light red points: D^0 from c-hadrons from c, normalized by c- D^0 triggers; dark red points: D^0 from c-all hadrons, normalized by c- D^0 triggers; light green points: D^0 from b-hadrons from b, normalized by b- D^0 triggers; dark green points: D^0 from b-all hadrons, normalized by b- D^0 triggers; blue points: All D^0 -hadrons from light quarks, normalized by all D^0 triggers. The panels show the ranges: $3 < p_T(D) < 5 \text{ GeV}/c$, $0.3 < p_T(\text{assoc}) < 1 \text{ GeV}/c$ (top-left); $3 < p_T(D) < 5 \text{ GeV}/c$, $p_T(\text{assoc}) > 1 \text{ GeV}/c$ (top-right); $8 < p_T(D) < 16 \text{ GeV}/c$, $0.3 < p_T(\text{assoc}) < 1 \text{ GeV}/c$ (bottom-left); $8 < p_T(D) < 16 \text{ GeV}/c$, $p_T(\text{assoc}) > 1 \text{ GeV}/c$ (bottom-right).

371 The consistency check was performed to verify whether, after having applied all the corrections to the
 372 azimuthal correlation plots at reconstructed level, the results were compatible with the ones at kinematic
 373 level. Hence, the ratios of fully corrected reconstructed plots over kinematic plots were evaluated in all
 374 the D^0 p_T bins and for the various p_T thresholds for the associated tracks, separating the contributions for
 375 the different origins of particles and triggers. The ratios, shown in Figure 16, denote a good compatibility
 376 with 1, within the uncertainties, with the only exception being due to some structures in the near side
 377 region for the beauty origin case. These structures were already found in the pp 2010 and p-Pb 2013
 378 analysis, and it was verified that they are induced by our topological selection for the D mesons. Indeed,
 379 in cases in which the D meson triggers come from B hadrons, applying the topological cuts (especially
 380 the cosine of the pointing angle) tends to favour cases with a small angular opening between the products
 381 of the B hadron decay (i.e. the D meson trigger itself and other particles), with respect to cases where
 382 the B decay particles are less collinear.

383 In the Monte Carlo closure test, this situation is reflected in the correlation distributions at reconstructed
 384 level, where the topological selection is applied, while it does not occur at kinematic level. Hence, in
 385 the reconstructed/kinematic ratio, the distribution would show an excess for $\Delta\phi = 0$ (due to the favoured
 386 decays with small opening angle), which is then compensated by a depletion for larger values of $\Delta\phi = 0$

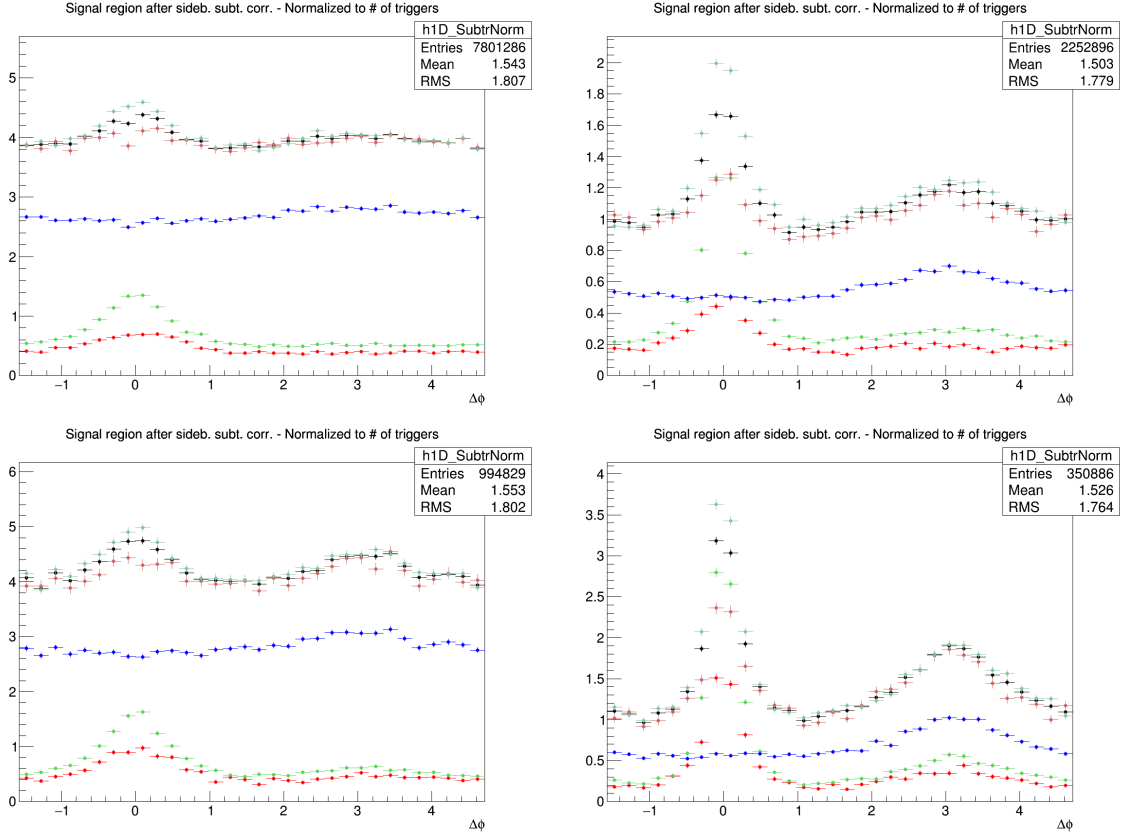


Figure 15: D^0 -hadrons azimuthal correlation distribution obtained from Monte Carlo, at reconstructed step. Black points: All D^0 -all hadrons, normalized by all D^0 triggers; light red points: D^0 from c-hadrons from c, normalized by c- D^0 triggers; dark red points: D^0 from c-all hadrons, normalized by c- D^0 triggers; light green points: D^0 from b-hadrons from b, normalized by b- D^0 triggers; dark green points: D^0 from b-all hadrons, normalized by b- D^0 triggers; blue points: All D^0 -hadrons from light quarks, normalized by all D^0 triggers. The panels show the ranges: $3 < p_T(D) < 5 \text{ GeV}/c$, $0.3 < p_T(\text{assoc}) < 1 \text{ GeV}/c$ (top-left); $3 < p_T(D) < 5 \text{ GeV}/c$, $p_T(\text{assoc}) > 1 \text{ GeV}/c$ (top-right); $8 < p_T(D) < 16 \text{ GeV}/c$, $0.3 < p_T(\text{assoc}) < 1 \text{ GeV}/c$ (bottom-left); $8 < p_T(D) < 16 \text{ GeV}/c$, $p_T(\text{assoc}) > 1 \text{ GeV}/c$ (bottom-right).

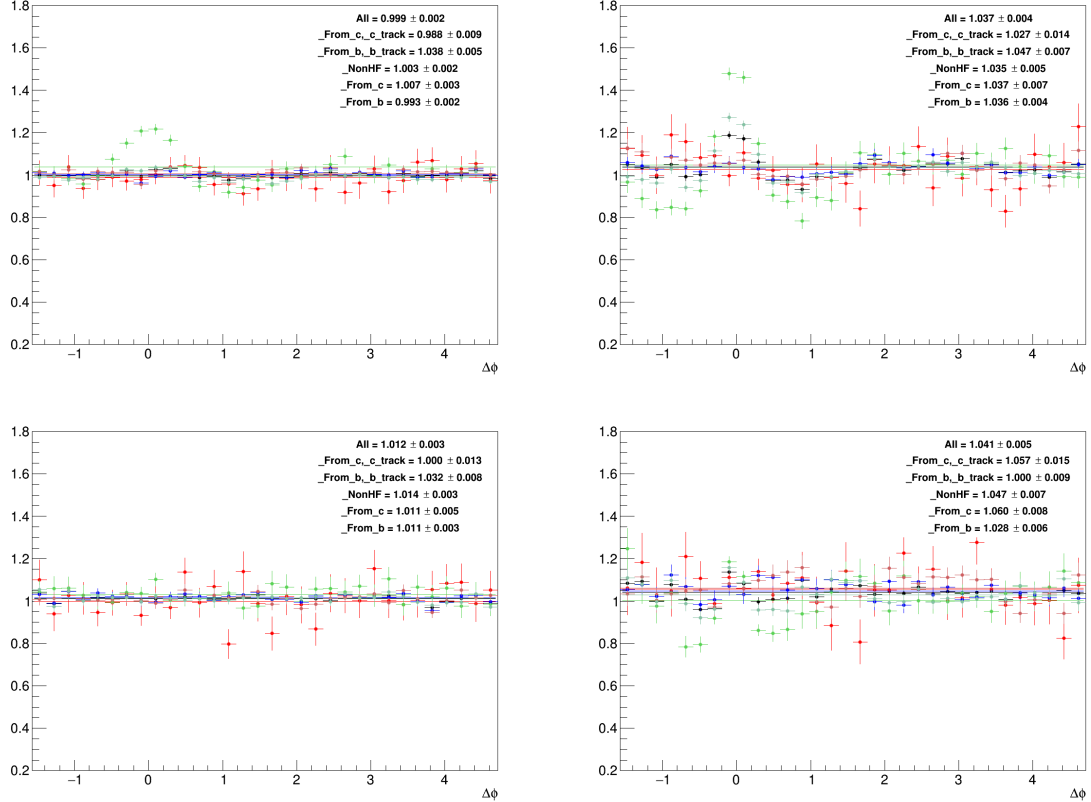


Figure 16: Ratios of fully corrected azimuthal correlation plots at reconstructed level over azimuthal correlation plots at kinematic level, in the two D^0 p_T bins, for the different associated p_T ranges. Black points: All D^0 -all hadrons, normalized by all D^0 triggers; light red points: D^0 from c-hadrons from c, normalized by c- D^0 triggers; dark red points: D^0 from c-all hadrons, normalized by c- D^0 triggers; light green points: D^0 from b-hadrons from b, normalized by b- D^0 triggers; dark green points: D^0 from b-all hadrons, normalized by b- D^0 triggers; blue points: All D^0 -hadrons from light quarks, normalized by all D^0 triggers. The panels show the ranges: $3 < p_T(D) < 5 \text{ GeV}/c$, $0.3 < p_T(\text{assoc}) < 1 \text{ GeV}/c$ (top-left); $3 < p_T(D) < 5 \text{ GeV}/c$, $p_T(\text{assoc}) > 1 \text{ GeV}/c$ (top-right); $8 < p_T(D) < 16 \text{ GeV}/c$, $0.3 < p_T(\text{assoc}) < 1 \text{ GeV}/c$ (bottom-left); $8 < p_T(D) < 16 \text{ GeV}/c$, $p_T(\text{assoc}) > 1 \text{ GeV}/c$ (bottom-right).

(corresponding to B decays with larger angles, which are disfavoured). These structures are prominent at low $D^0 p_T$, where the topological cuts are tighter, and tend to disappear at higher p_T , where the selections are released. They are also larger in the higher associated track p_T ranges, where the fraction of B-hadron decay tracks dominate the overall correlation distributions.

The data correlation distribution need to be corrected for this bias, and in particular for the enhancement of b-origin correlation pairs at the centre of the near side region, which would influence the near-side peak features. In order to do this, the amount of the b-origin excess is evaluated from the Reco/Kine ratio, by considering the b- D^0 -all tracks case (dark green points). The excess at Reco level (affecting data) is quantified as a $\Delta\varphi$ modulation **modul** for the five points an each side of the $\Delta\varphi = 0$ value (or, equivalently, on the first five points of the reflected distributions, which start from $\Delta\varphi = 0$). This is done separately in each p_T range. Then, the correction is done by applying this modulation to the data correlation distributions, but taking into account that only the correlation entries from $B \rightarrow D$ are affected, while the $c \rightarrow D$ correlations need to be left unaltered. In particular, it has to be considered that:

- On data, the $B \rightarrow D$ correlation pairs are only a fraction ($1 - f_{\text{prompt}}$) of the total.
- The amplitude of $B \rightarrow D|_{\text{amplit}}$ correlation pattern is different (greater) than the amplitude of the $c \rightarrow D|_{\text{amplit}}$ correlation pattern:

Thus, the following equation is applied to get the corrected $C(\Delta\varphi)_{\text{corr}}$ data points starting from the raw ones, $C(\Delta\varphi)_{\text{raw}}$:

$$C(\Delta\varphi)_{\text{corr}} = C(\Delta\varphi)_{\text{raw}} \cdot \left[\frac{c \rightarrow D|_{\text{amplit}}}{(B + c) \rightarrow D|_{\text{amplit}}} \cdot f_{\text{prompt}} + \frac{B \rightarrow D|_{\text{amplit}}}{(B + c) \rightarrow D|_{\text{amplit}}} \cdot (1 - f_{\text{prompt}}) \cdot \frac{1}{\mathbf{modul}} \right] \quad (3)$$

where $(B + c) \rightarrow D|_{\text{amplit}} = c \rightarrow D|_{\text{amplit}} \cdot f_{\text{prompt}} + B \rightarrow D|_{\text{amplit}} \cdot (1 - f_{\text{prompt}})$, and where the two amplitudes are evaluated from the Monte Carlo distributions of Figure 15 at reconstructed level (so, including the bias), and f_{prompt} with the procedure described in 3.3.5. Applying the **modul** factor to the beauty part of the data correlation distributions brings its value back to the generated level case, effectively removing the bias. The effect of the correction is a shift of the data points in the near-side region (in general, downward in the first and second points, the upward in the others). The maximum value of the shift is of about 5%, at the centre of the near-side peak, for the lowest D-meson p_T range ($3 < p_T < 5 \text{ GeV}/c$) and the highest associated track p_T range ($p_T > 3 \text{ GeV}/c$). The typical values are instead of a couple of percentage points. The correction is zero in the highest D-meson p_T range. To take into account for possible inaccuracies in the definition of the modulations, or in their rescaling, a systematic uncertainty is applied on the corrected data points, with value $|C(\Delta\varphi)_{\text{corr}} - C(\Delta\varphi)_{\text{raw}}| / \sqrt{12}$, on each side of the data points affected by the bias (symmetric uncertainty).

417 **3.3.4 Secondary track contamination**

418 The secondary tracks inside the associated track sample, due to interaction of primary track with the de-
 419 tector material or to decays of strange hadrons, are mostly removed by the DCA cuts applied during the
 420 cut selection phase ($DCA(xy) < 1 \text{ cm}$, $DCA(z) < 1 \text{ cm}$). Anyway, a small fraction of secondary tracks
 421 survives this cut, and the data correlation distributions have to be corrected for this residual contami-
 422 nation. The fraction of surviving secondary tracks is evaluated via a study on the LHC17d2a_fast_new
 423 sample, by counting the number of tracks accepted by the selection whose corresponding generated-
 424 level track doesn't satisfy the `IsPhysicalPrimary()` call, and dividing this number by the total number
 425 of accepted tracks. The outcome of the check is reported in Figure 17. As it's visible, no more than
 426 5% secondary tracks pass the selection. Moreover, the fraction of residual secondary tracks is flat along
 427 the $\Delta\varphi$ axis, as shown, for exemplary p_T regions, in Figure 18, where the inhomogeneities are always
 428 below 1%. For this reason, it is possible to directly scale the data correlation distributions by their purity
 429 fraction (i.e. 1 - secondary contamination). This is done with an associated p_T dependence, due to the
 430 increase of the purity with the track p_T , while the purity fraction is taken flat versus the D-meson p_T .
 431 The purity values that were chosen are the following:

- 432 – $p_T(\text{assoc}) > 0.3 \text{ GeV}/c : 0.958$
- 433 – $p_T(\text{assoc}) > 1 \text{ GeV}/c : 0.973$
- 434 – $0.3 < p_T(\text{assoc}) < 1 \text{ GeV}/c : 0.953$
- 435 – $1 < p_T(\text{assoc}) < 2 \text{ GeV}/c : 0.969$
- 436 – $2 < p_T(\text{assoc}) < 3 \text{ GeV}/c : 0.982$
- 437 – $p_T(\text{assoc}) > 3 \text{ GeV}/c : 0.990$

438 It was also verified with the same Monte Carlo study that applying the DCA selection rejects less than
 439 0.2% primary tracks (tagged as false positives) from the associated track sample, again with a flat az-
 440 imuthal distribution, inducing hence a fully negligible bias on the data correlation distributions. This is
 441 shown in Figure 19. This was also verified for specific charm-origin and beauty-origin tracks, due to
 442 their larger DCA with respect to primary tracks from light quarks. In this case, the fraction of rejected
 443 charm and beauty tracks stays below 1% in all the kinematic ranges apart from the associated track p_T
 444 regions 0.3-1 and $> 0.3 \text{ GeV}/c$, where the rejection can be as high as 2%. In these kinematic ranges,
 445 though, the data correlation distributions are dominated by non-heavy-flavour tracks, as it was verified
 446 from the simulations, hence the overall bias is still contained below 1%, thus negligible.

447 These studies were performed on an enriched Monte Carlo sample, which could not fully reproduce
 448 the relative abundancies of the species. Anyway, for events with a reconstructed D-meson, this bias is
 449 expected to be minor, and only these events are used in the data analysis. In any case, the percentages
 450 obtained from the study were found to be consistent within 1% with the outcome of the studies for the
 451 p-Pb 2013 analysis, which reassures us on the full validity of these results.

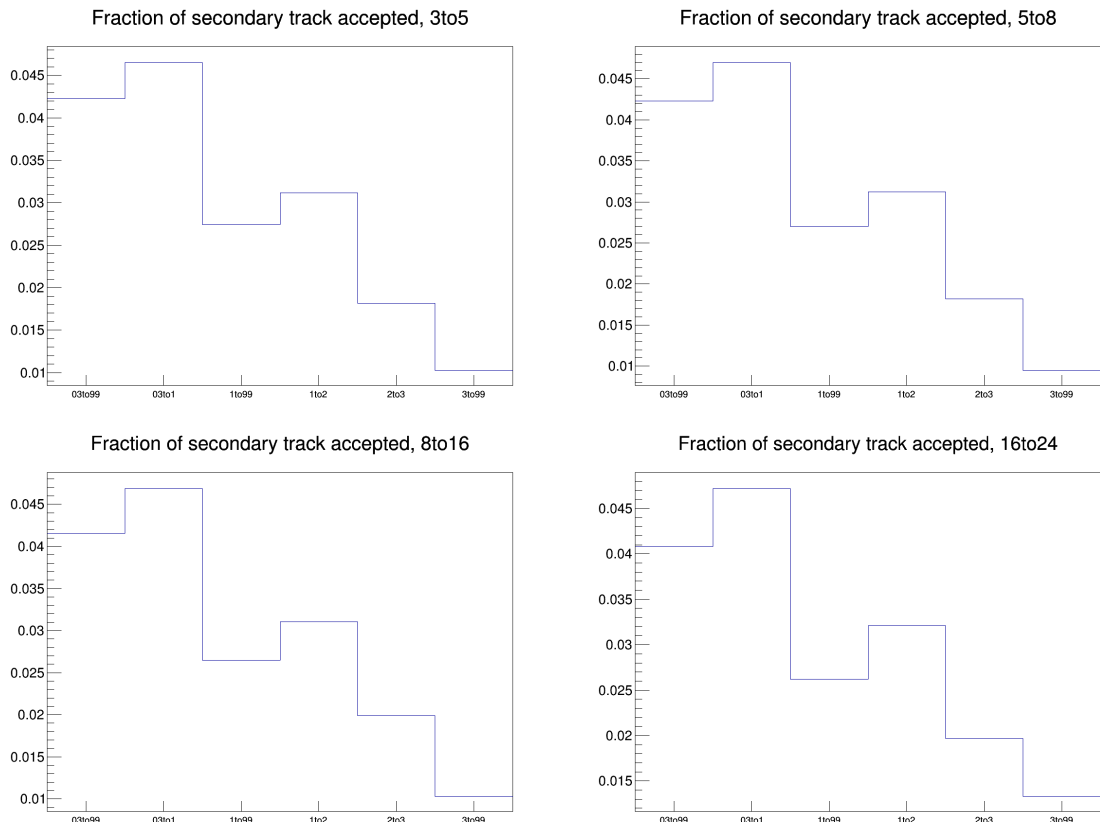


Figure 17: Fraction of secondary tracks over total amount of tracks which pass the DCA selection. The four panel show the fractions for the D-meson p_T ranges: 3-5, 5-8, 8-16, 16-24, respectively. Inside each panel, the associated track p_T ranges are shown on the x -axis.

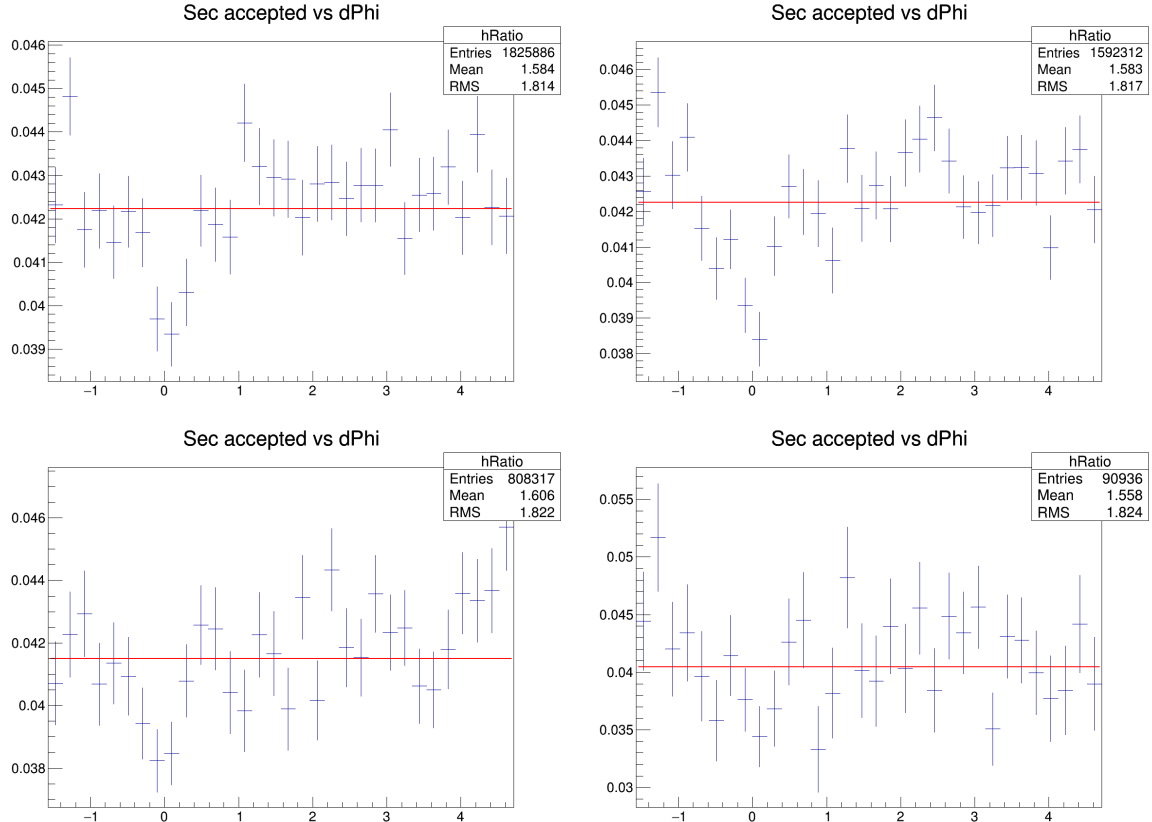


Figure 18: $\Delta\phi$ dependence of the fraction of secondary tracks in the D^0 - h correlation distributions. The four panel show the fractions for the D -meson p_T ranges: 3-5, 5-8, 8-16, 16-24, respectively. The associated track p_T ranges are the integrated one, i.e. $p_T > 0.3 \text{ GeV}/c$.

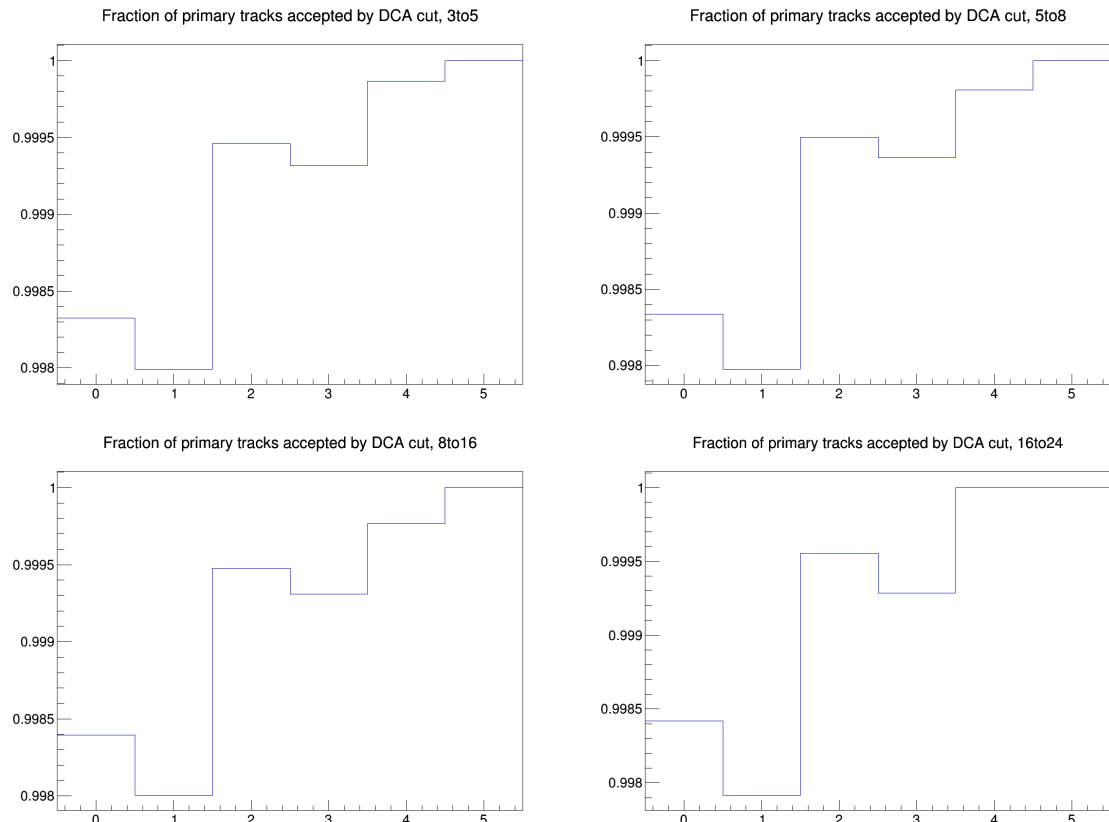


Figure 19: Fraction of primary tracks rejected by the DCA selection. The four panel show the fractions for the D-meson p_T ranges: 3-5, 5-8, 8-16, 16-24, respectively. Inside each panel, the associated track p_T ranges are shown on the x -axis.

452 **3.3.5 Beauty feed-down**

453 The contribution of correlations of D meson from b-hadron decay is subtracted from the data correlation
 454 distributions as:

$$\tilde{C}_{\text{prompt D}}(\Delta\varphi) = \frac{1}{f_{\text{prompt}}} \left(\tilde{C}_{\text{inclusive}}(\Delta\varphi) - (1 - f_{\text{prompt}}) \tilde{C}_{\text{feed-down}}^{\text{MC templ}}(\Delta\varphi) \right). \quad (4)$$

455 In the above equation, $\tilde{C}_{\text{inclusive}}(\Delta\varphi)$ and $\tilde{C}_{\text{prompt D}}(\Delta\varphi)$ are per-trigger azimuthal correlation distribu-
 456 tions before and after feed-down contribution subtraction, f_{prompt} is the fraction of prompt D meson
 457 and $\tilde{C}_{\text{feed-down}}^{\text{MC templ}}$ is a template of the azimuthal correlation distribution for the feed-down component ob-
 458 tained from home-made Monte Carlo simulation at generated level, using PYTHIA6 with Perugia2011
 459 tune. In order to avoid biases related to the different event multiplicity in real and simulated events,
 460 the correlation distribution was shifted to have its minimum coinciding with the baseline of the data
 461 azimuthal-correlation distribution before feed-down subtraction.

462 The value of f_{prompt} (Figure 20), which depends on D-meson species and varies as a function of the p_T ,
 463 is estimated on the basis of FONLL predictions for the production of feed-down D mesons at central
 464 rapidity, in pp collisions at $\sqrt{(s)} = 5$ TeV, and using the reconstruction efficiency of prompt and feed-
 465 down D mesons, following the so-called N_b approach defined in [5]. Typical values are about 8-10%
 466 for the D^0 , about 4-7% for the D^+ and about 5-8% for the D^{*+} . The procedure adopted is the same
 467 as what done in the past analysis [6]: however, in p-Pb, in order to consider a possible non-zero v_2 -
 468 like modulation of the baseline, a range of $0 < v_2 < 0.2$ values for tracks and for secondary D mesons
 469 is considered for the systematic uncertainty evaluation (using an hypothesis of no modulation for both
 470 cases for central values).

471 Examples of the PYTHIA templates used for the feed-down contribution subtraction are shown in Figures
 472 21 (Figure 22 shows the same templates but for prompt D mesons).

473 The feed-down subtraction was performed after rescaling the data correlation distributions for the purity
 474 fraction, and correcting them by the near-side modulation induced by the bias on the B decay topology.

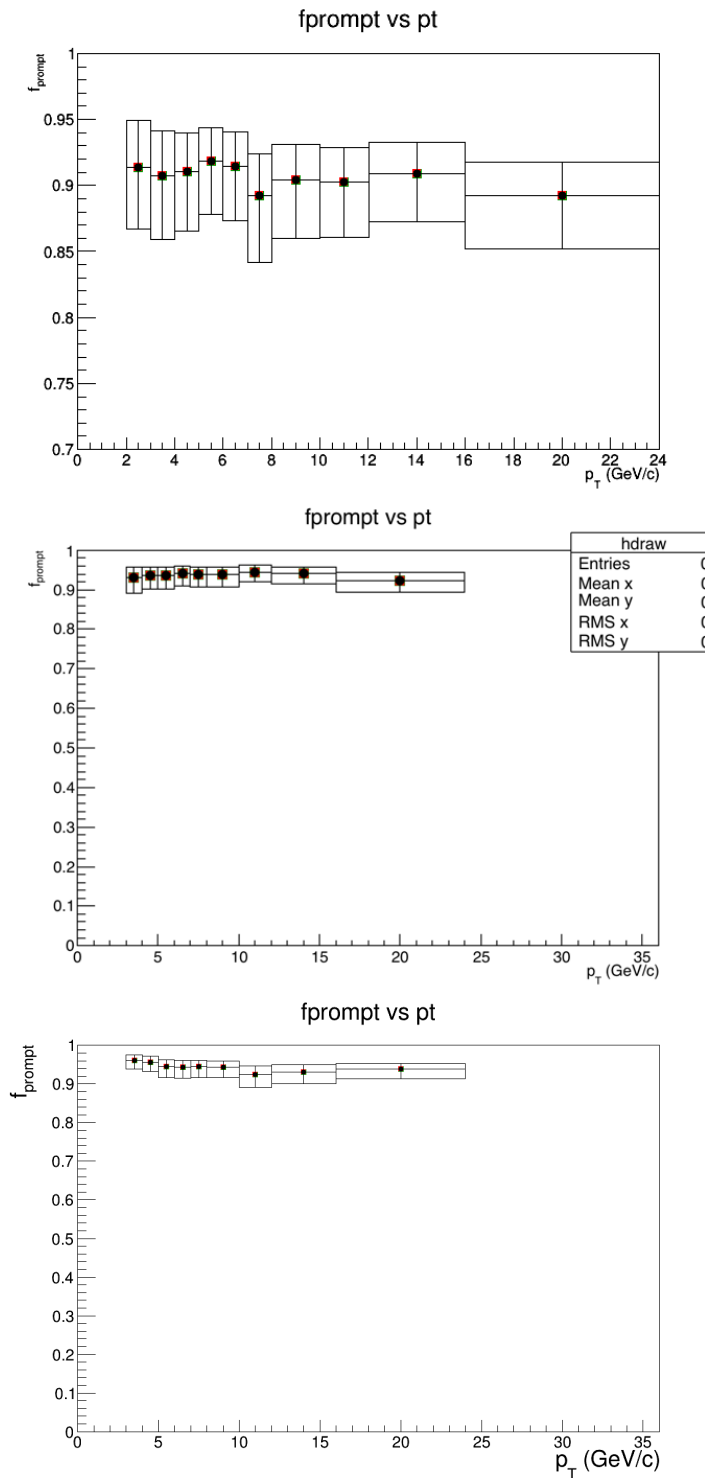


Figure 20: f_{prompt} as a function of the p_T for D^0 (top), D^{*+} (mid) and D^+ (bottom) estimated on the basis of FONLL predictions

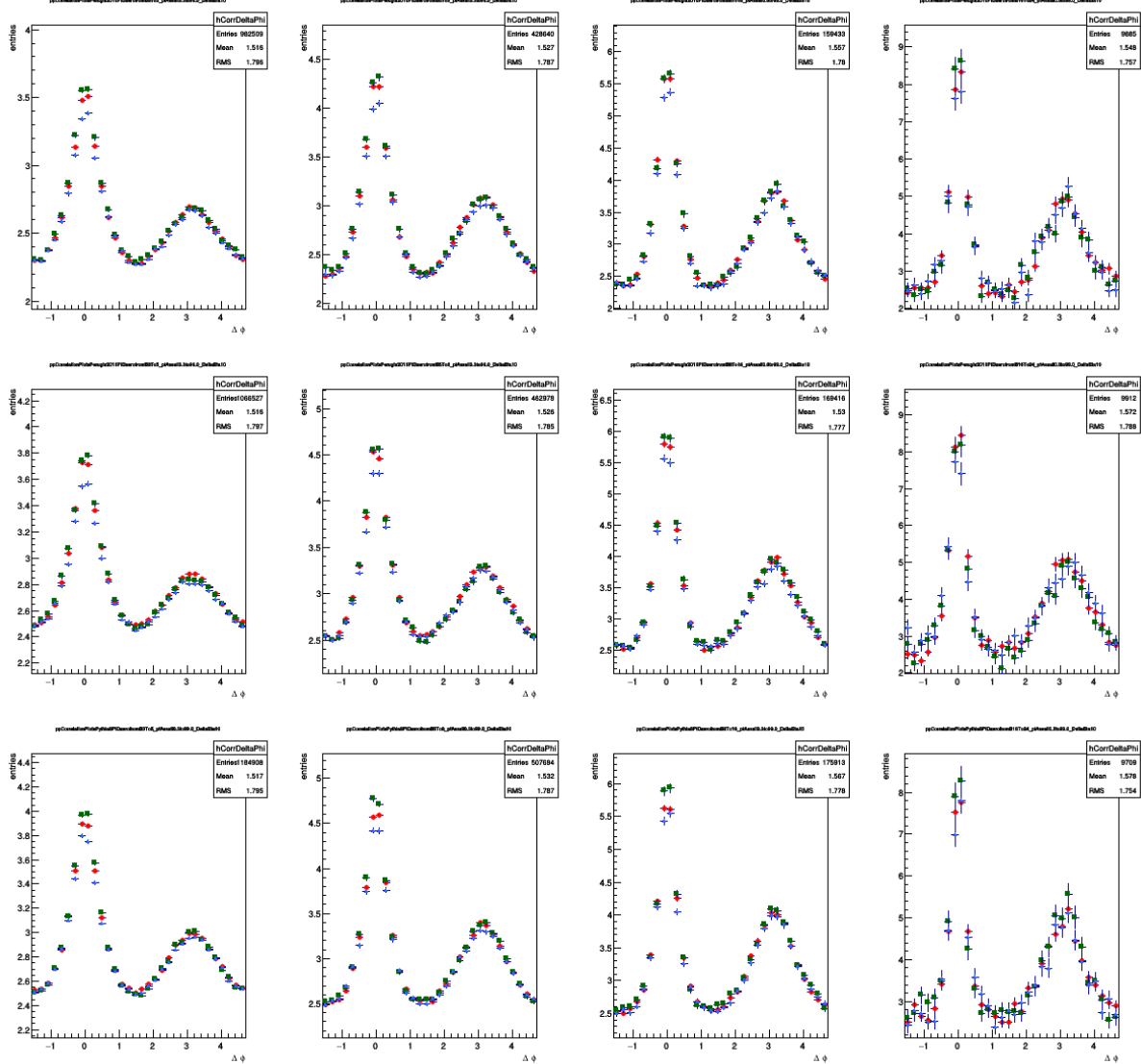


Figure 21: Azimuthal correlation distribution between D meson from b-hadron decay and charged particles obtained from Monte Carlo simulations based on Pythia-Perugia2010 tune (row1), Pythia-Perugia2011 tune (row2), Pythia8 tune 4C (row3) for associated track $p_T > 0.3$ GeV/ c and D-meson p_T ranges: 3-5, 5-8, 8-16, 16-24 GeV/ c . D^0 in blue, D^+ in green, D^{*+} in red.

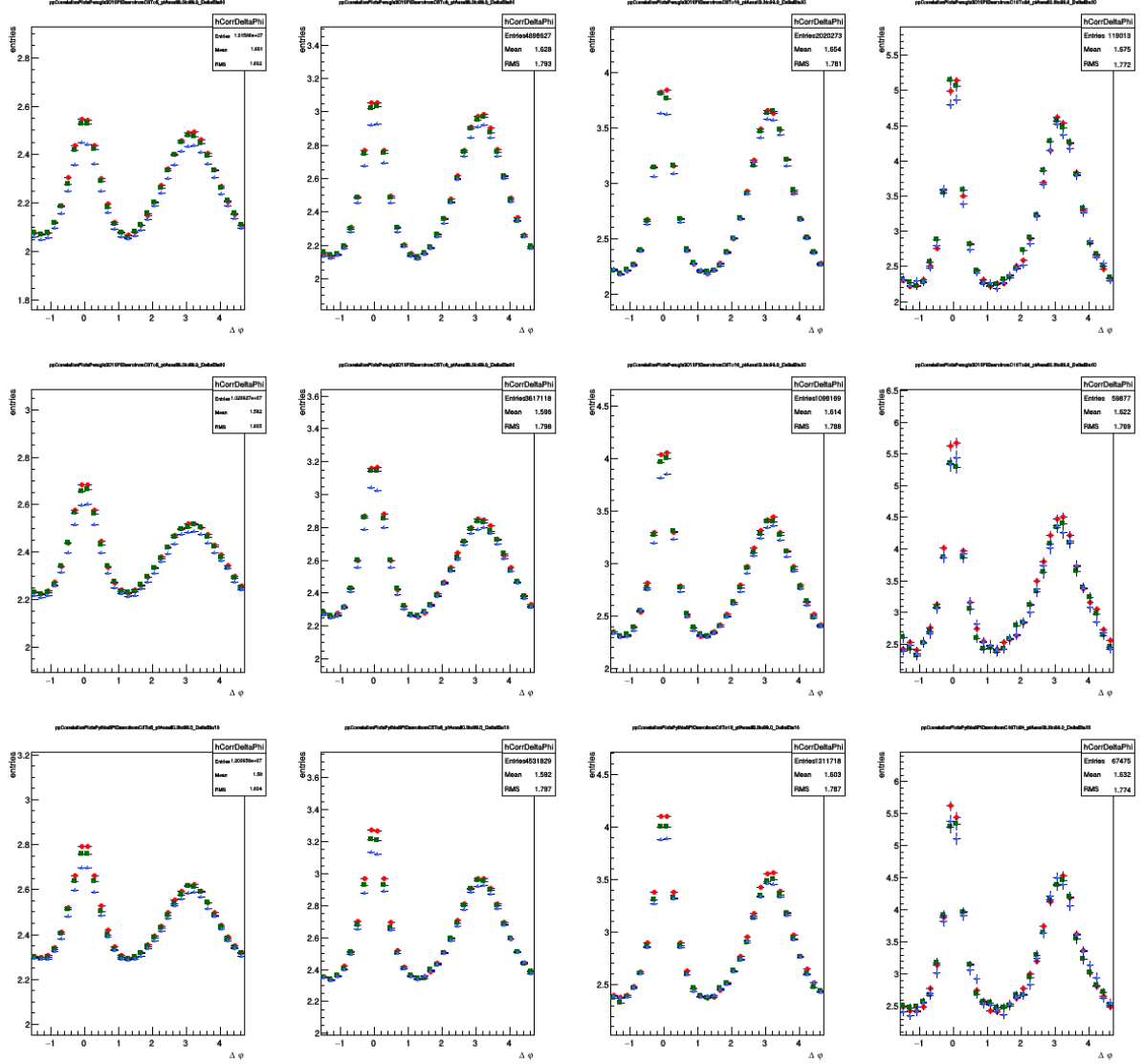


Figure 22: Azimuthal correlation distribution between prompt D meson and charged particles obtained from Monte Carlo simulations based on Pythia-Perugia2010 tune (row1), Pythia-Perugia2011 tune (row2), Pythia8 tune 4C (row3) for associated track $p_T > 0.3$ GeV/ c and D-meson p_T ranges: 3-5, 5-8, 8-16, 16-24 GeV/ c . D⁰ in blue, D⁺ in green, D^{*+} in red.

4 Systematic uncertainties on $\Delta\phi$ correlation distributions

4.1 Uncertainty on S and B extraction

The systematic uncertainty for the D meson yield extraction was determined separately for the three mesons. It was obtained by evaluating the value of the signal candidate from the invariant mass spectra with the following differences with respect to the standard approach:

- Changing the background fit function, for D^0 and D^+ (tried with polynomials of 1st and 2nd order) and for D^{*+} (tried with polynomials of 2nd order and a power function);
- Changing the range in which the signal is extracted from the Gaussian fit;
- Reducing the range of invariant mass axis in which the signal region is defined (and S and B are extracted);
- Rebinning the invariant mass distributions before the fit for D^0 and D^+
- Extracting S and B via integral of the fit functions or B via bin counting and S via integral of the Gaussian function.

Both the value of the yield and the sidebands correlations normalization factor are affected by changing the yield extraction approach, while the rest of the procedure to extract the azimuthal correlation distribution is the same as in the standard analysis. The fully corrected azimuthal correlation plots were evaluated, for each of these approaches, in all D meson p_T bins and for each value of associated tracks p_T threshold. The ratios of the correlation distributions obtained with the standard yield extraction procedure and by differentiating the approach were evaluated. From the average of these ratios, which are found to be flat versus $\Delta\phi$, a systematic uncertainty can be extracted, which was taken of 1% for $3 < p_T(D) < 16 \text{ GeV}/c$ and of 2% in $16 < p_T(D) < 24 \text{ GeV}/c$ (3% for D^0). No dependence versus the associated track p_T was assumed, since from a physics point of view we don't expect a modification of the signal and sideband values to have a dependence of this kind. Figures 23, show the ratios obtained by the above mentioned procedure for exemplary p_T ranges, which anyway span over the full kinematic ranges analyzed, for D^0 -h correlations. Figures 24 and 25 show the same ratios for D^{*+} -h, D^+ -h as well.

4.2 Uncertainty on background correlation shape

The systematic uncertainty for the subtraction of the background correlations includes the effects due to a potentially biased description of the background correlation shape, which is evaluated from of the sidebands correlations. In particular, the background correlation shape could present some hidden invariant mass dependence. To estimate this uncertainty, the invariant mass range of the sidebands definitions was varied with respect to the default values. For the D^0 meson, the usual range of the sidebands is 4 to 8 σ from the centre of the peak of the Gaussian fit and it was modified, for both sidebands to:

- inner half (4 to 6 σ from the centre of the peak);
- outer half (6 to 8 σ from the centre of the peak)
- extended to 4 to 10 σ (in case this is possible without exceeding the fitting range of the mass plots)

Slightly different variations, but with the same reasoning, were considered for the D^+ meson.

For the D^{*+} meson, the usual range of sideband in invariant mass spectra is 5 to 10 σ (only on the right side) from the centre of the peak of the Gaussian fit of the invariant mass spectra, and it was modified to:

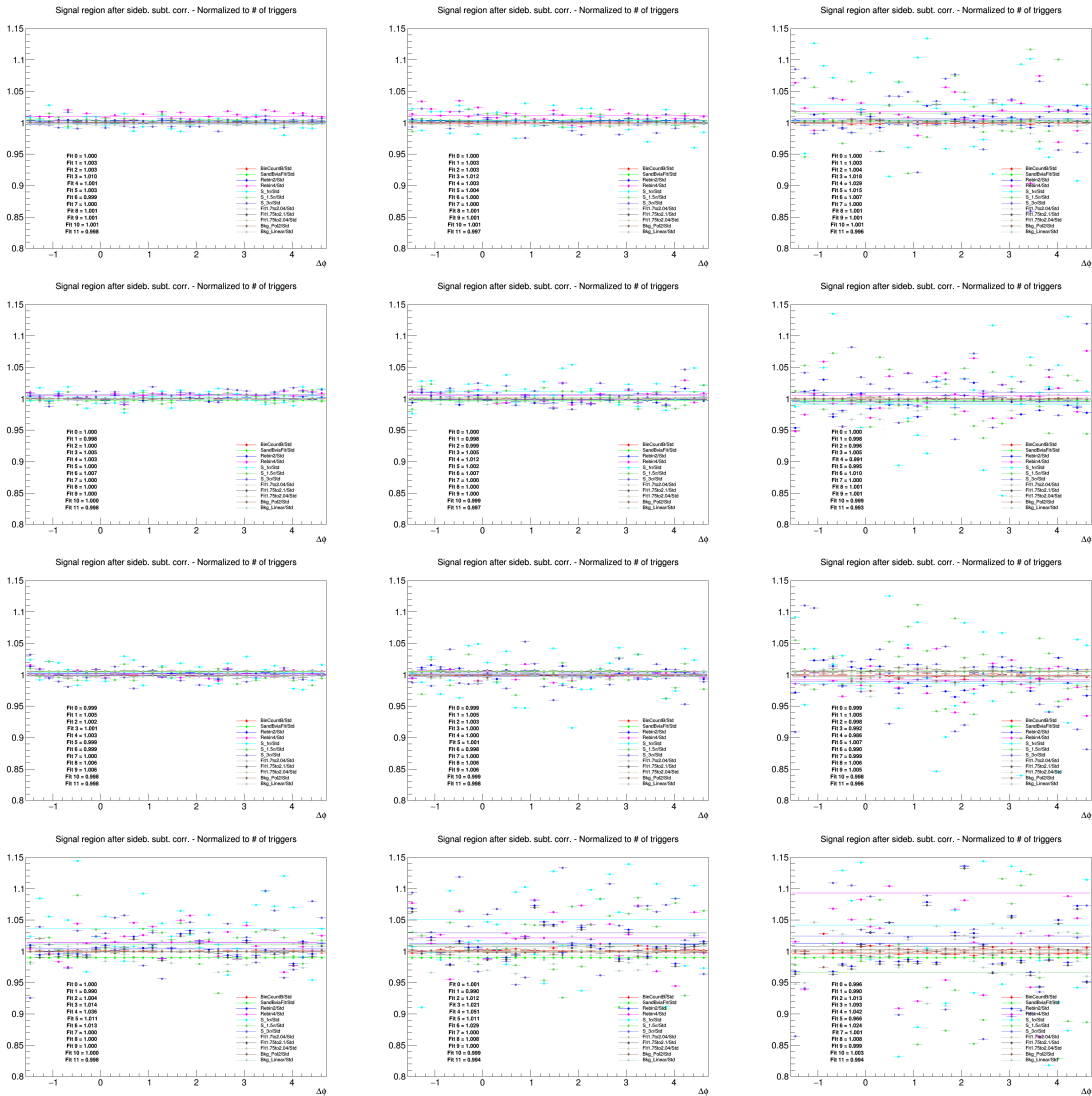


Figure 23: Ratios of D^0 - h correlation plots obtained changing S and B extraction procedure over those obtained with standard yield extraction procedure. Rows: $p_T(D^0)$ 3-5, 5-8, 8-16, 16-24 GeV/c . In each row, the panels show the associated track p_T ranges 0.3-1, 1-2, $>3 \text{ GeV}/c$, respectively.

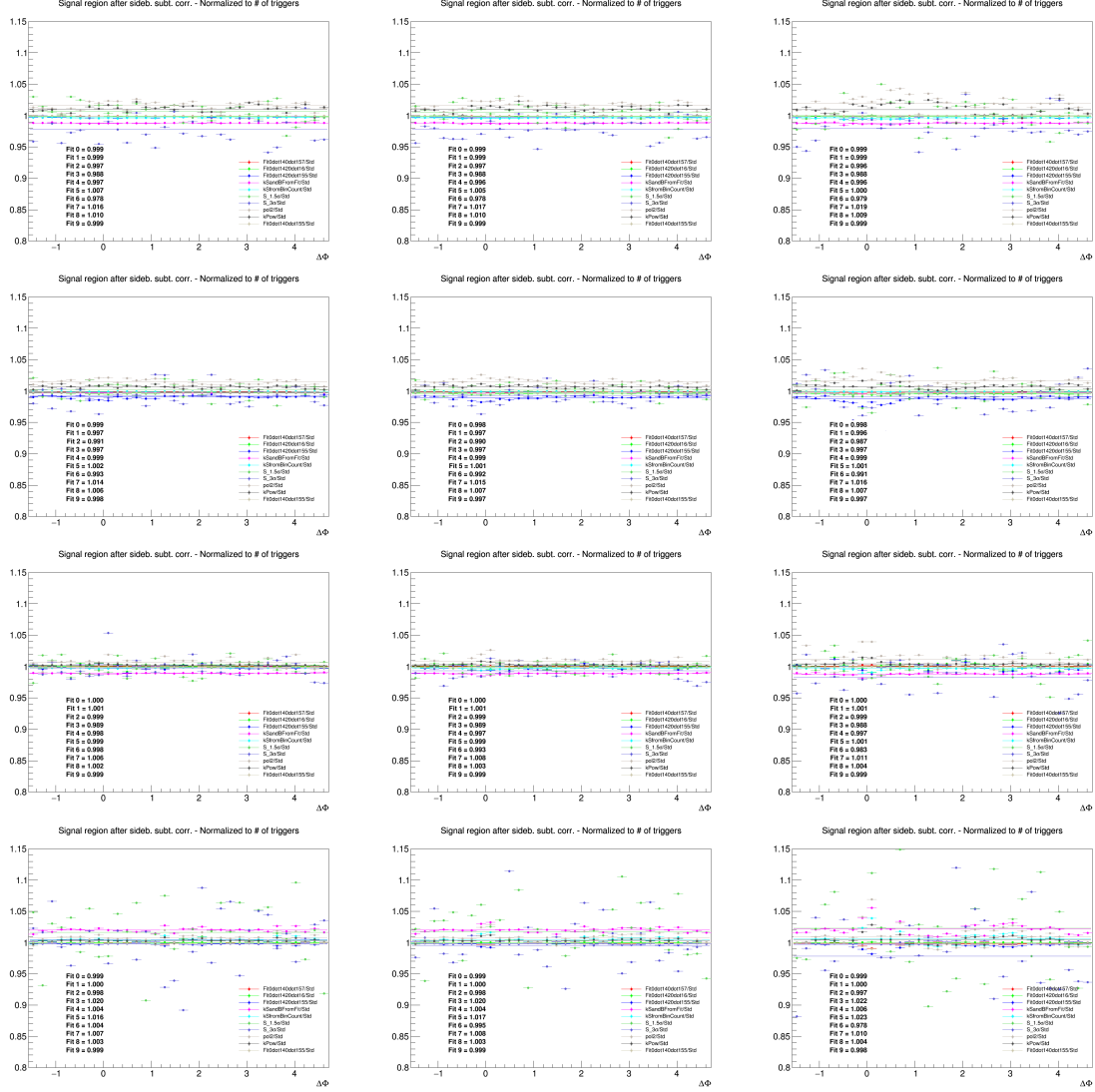


Figure 24: Ratios of D^{*+} - h correlation plots obtained changing S and B extraction procedure over those obtained with standard yield extraction procedure. Rows: $p_T(D^{*+})$ 3-5, 5-8, 8-16, 16-24 GeV/c . In each row, the panels show the associated track p_T ranges $>0.3 \text{ GeV}/c$, $0.3-1 \text{ GeV}/c$ and $>1 \text{ GeV}/c$, respectively.

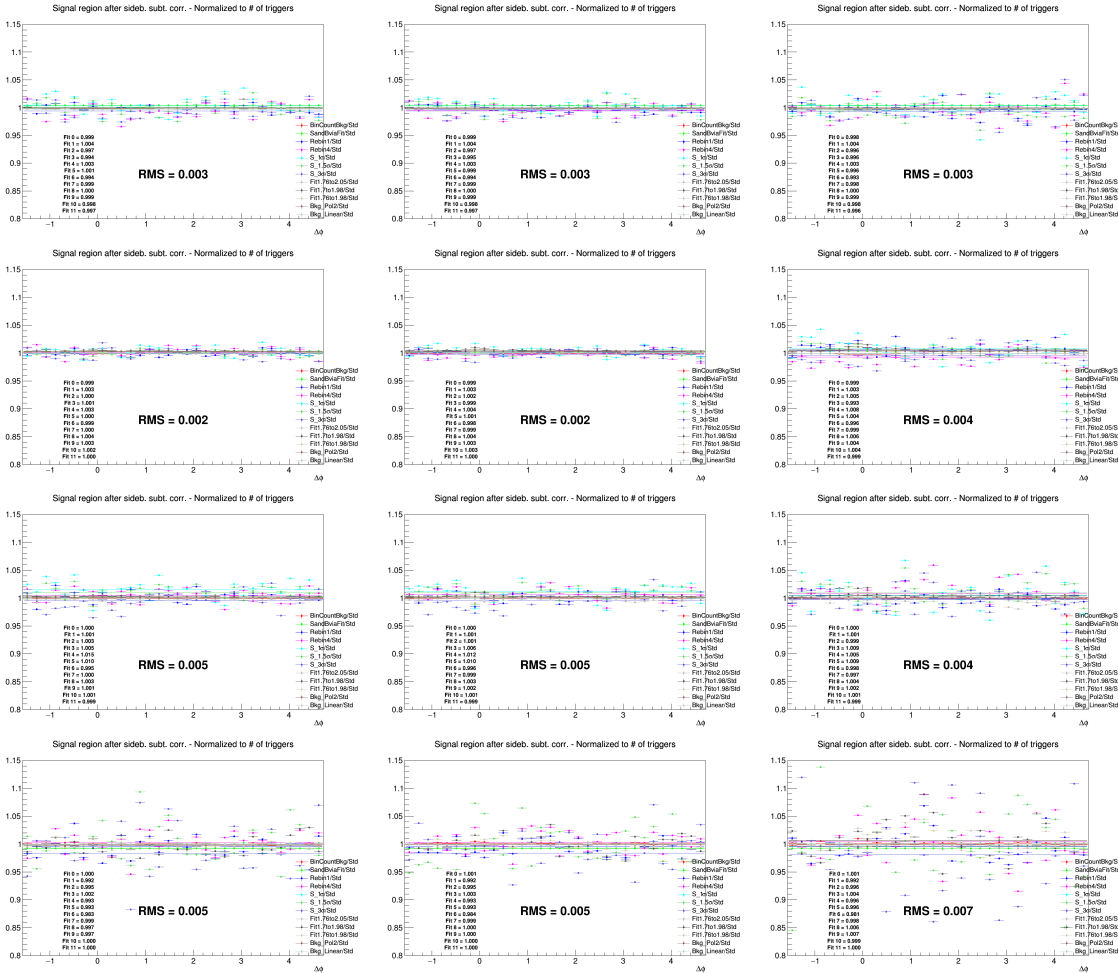


Figure 25: Ratios of D⁺-h correlation plots obtained changing S and B extraction procedure over those obtained with standard yield extraction procedure. Rows: $p_T(D^+)$ 3-5, 5-8, 8-16, 16-24 GeV/c. In each row, the panels show the associated track p_T ranges 0.3-1 GeV/c, >0.3 GeV/c, and >1 GeV/c, respectively.

- inner half (5 to 8 σ from the centre of the peak);
- outer half (8 to 13 σ from the centre of the peak);
- extended to 5 to 13 σ from the centre of the peak;
- extended to 6 to 16 σ from the centre of the peak.

The rest of the procedure for the azimuthal correlations distribution was unchanged, and the ratios of the fully corrected azimuthal correlation plots obtained with the standard sidebands range and the correlation plots extracted with different sidebands definitions, were evaluated for each D-meson p_T bin and associated tracks p_T threshold. Results of this check are shown in Figures 26, 27 and 28 for D^0 , D^{*+} , D^+ respectively, for exemplary p_T ranges, spanning over the full kinematic regions analysis. From the values of the ratios extracted from the checks, which do not show any azimuthal dependence a systematic uncertainty for the background subtraction can be evaluated. Also no dependence versus the associated track p_T was assumed also in this case. The uncertainty was hence taken of 1% for $3 < p_T(D) < 16$ GeV/ c and 3% for $16 < p_T(D) < 24$ GeV/ c for the three D mesons.

4.3 Uncertainty on D-meson cut stability

To study the systematics due to the topological selections on the D meson, the cut variation approach was used. For each D-meson, alternate sets of released and tightened selection cuts were applied to extract the correlation distribution, varying in particular the cosine of the pointing angle, the maximum DCA among the daughter tracks and the product of the daughter track impact parameters. For each set of cuts new 2D (p_T vs multiplicity), D meson efficiency map was computed. In Figures 29, 30, 31 (for D^0 , D^{*+} and D^+ , respectively) the ratio of the different 1D efficiencies with the alternate cuts with respect to the default cut selection is chosen, to highlight how the different selections effectively varied the efficiency values, especially at low p_T , where cuts are more effective.

Figure 32, 33, 34 show the ratio of the correlation distributions with alternate cut sets over those with the standard approach, for exemplary p_T ranges covering the full kinematic region of interest for the analyses. The ratios are reasonably flat in $\Delta\phi$, hence a flat systematic was evaluated as systematic uncertainty from D-meson the cut variations. For the D^0 , the uncertainty was considered of 2% for all the p_T ranges of trigger and tracks analyzed. For the D^{*+} , the uncertainty was considered of 1.5% for $3 < p_T(D) < 8$ GeV/ c and of 1% for $8 < p_T(D) < 24$ GeV/ c . For the D^+ , the uncertainty was considered of 1% for $3 < p_T(D) < 16$ GeV/ c and of 3% for $16 < p_T(D) < 24$ GeV/ c .

4.4 Uncertainty on tracking efficiency evaluation

The systematic uncertainty for the tracking efficiency includes the effects related to the set of filtering cuts defined for the associated tracks selection (mainly requests on the quality of reconstructed tracks for the TPC and ITS detectors). This uncertainty was determined by repeating the full analysis using different selections for the cuts on the associated tracks with respect to the usual selection (TPC only tracks with at least 2 points in the ITS). The alternative selections were: pure TPConly selection, meaning TPC tracks with no requests on the number of hits in the ITS, and TPC+ITS selection, which requires filterbit 4 with, in addition, at least 3 points in the ITS, ITS refit and a hit in at least an SPD layer. The ratios of the azimuthal correlation distributions with different sets of tracks selection over distributions with standard selection were evaluated, and are shown in Figures 35 and 36 for D^0 -h correlations. Their values were used to determine a systematic uncertainty, which as the previous ones could be assigned flat in $\Delta\phi$, and which was estimated of 3% in all the ranges of p_T analyzed.

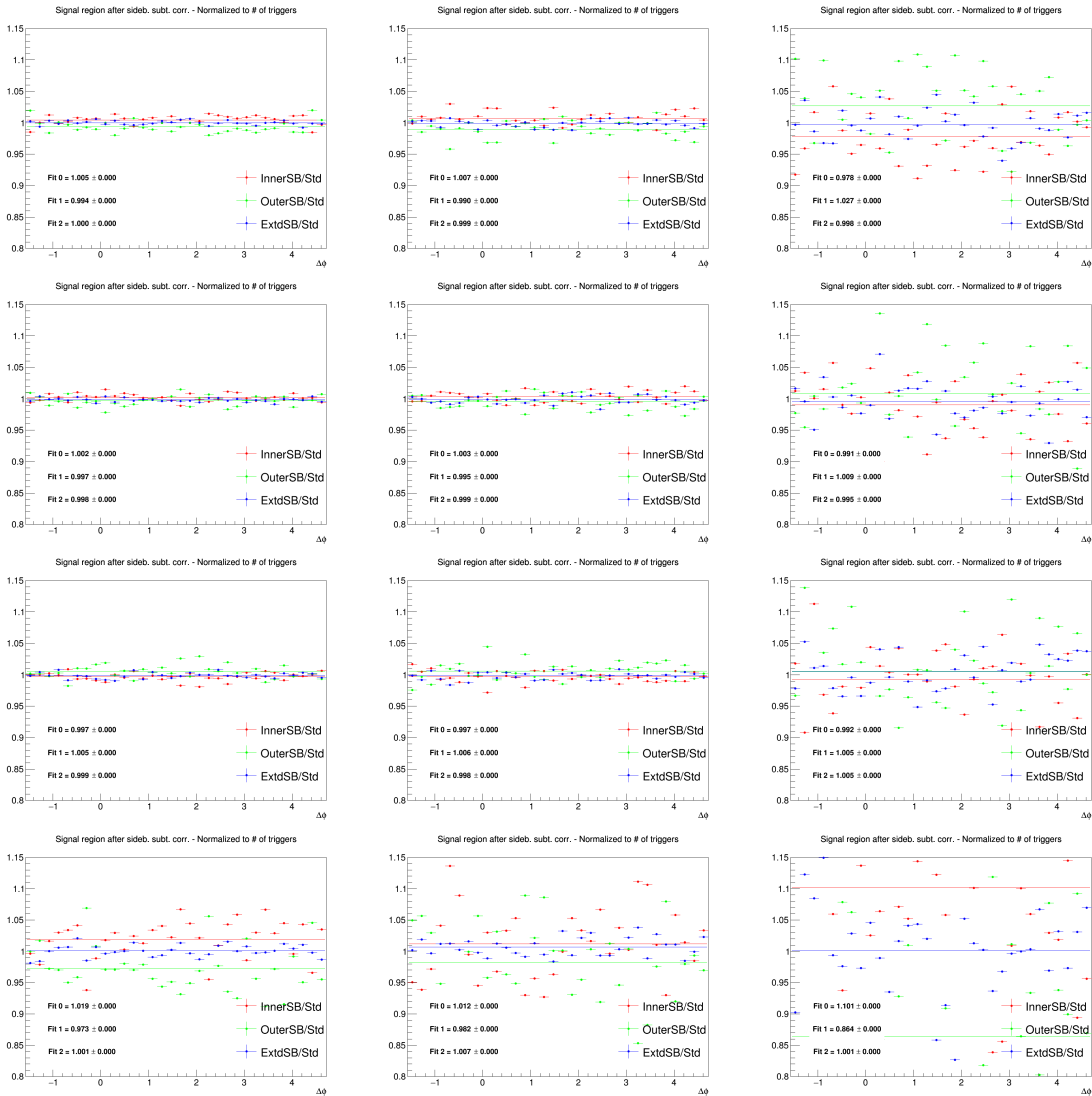


Figure 26: Ratios of D^0 - h correlation plots obtained by changing the sideband ranges over those obtained with standard sideband ranges. Rows: $p_T(D^0)$ 3-5, 5-8, 8-16, 16-24 GeV/ c . In each row, the panels show the associated track p_T ranges 0.3-1, 1-2, >3 GeV/ c , respectively.

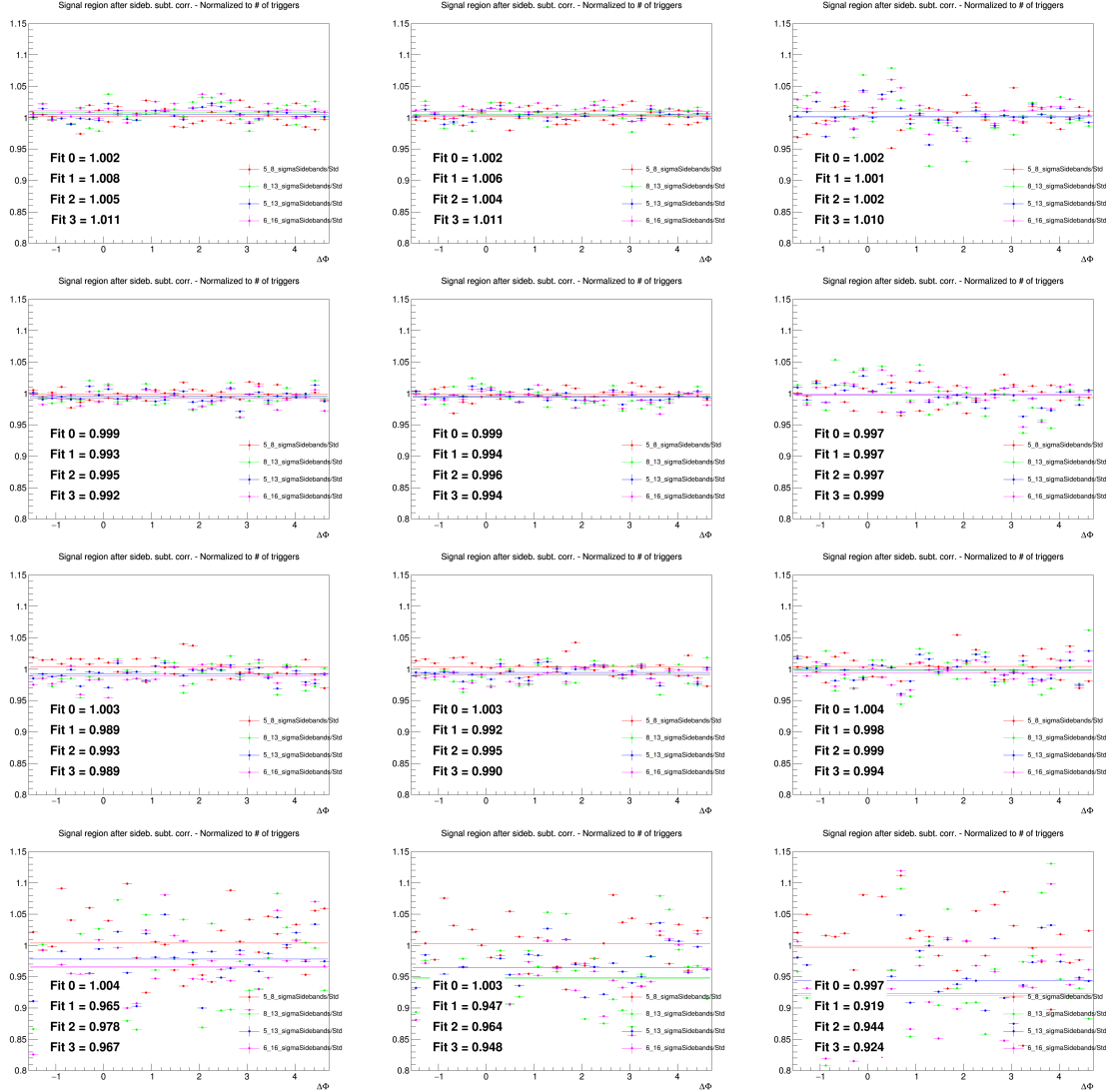


Figure 27: Ratios of $D^*+ - h$ correlation plots obtained by changing the sideband ranges over those obtained with standard sideband ranges. Rows: $p_T(D^*)$ 3-5, 5-8, 8-16, 16-24 GeV/c. In each row, the panels show the associated track p_T ranges 0.3-1, >0.3 GeV/c and >1 GeV/c, respectively.

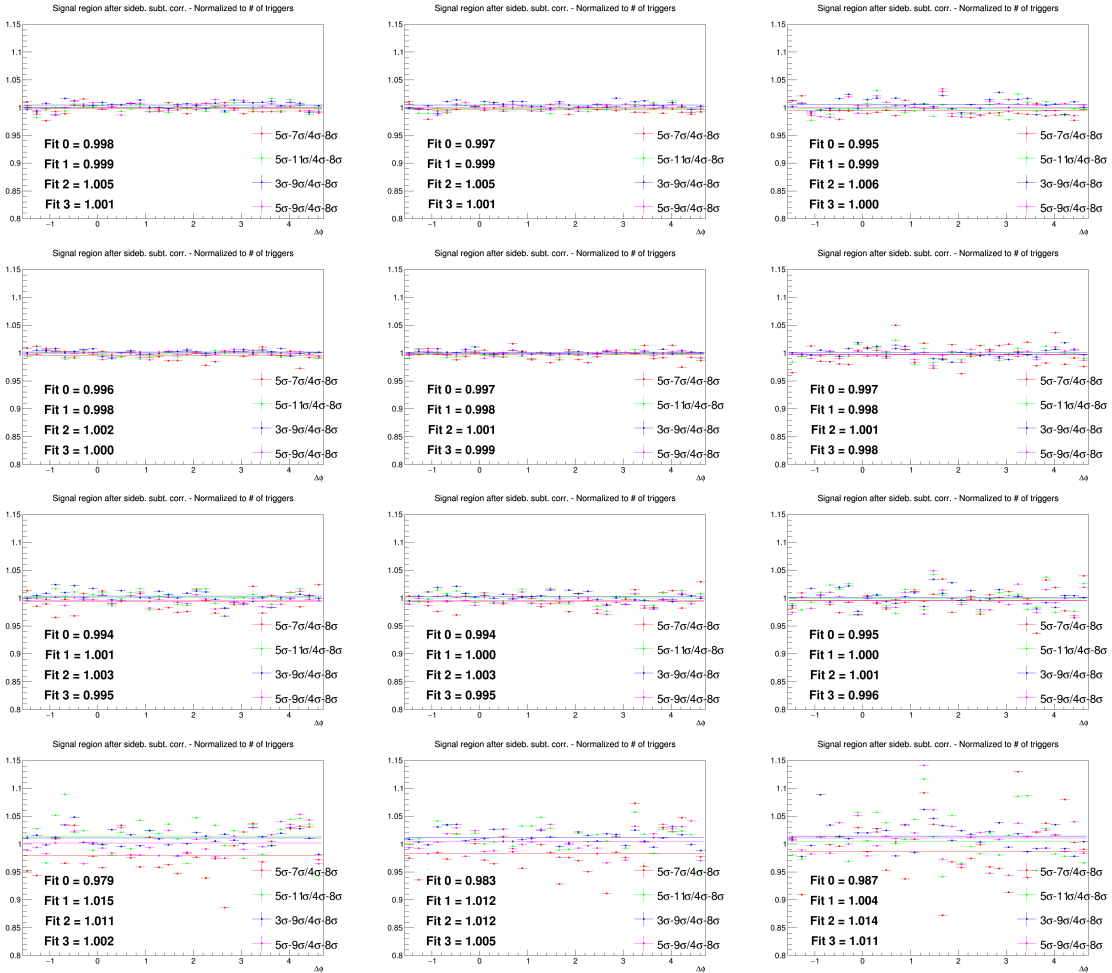


Figure 28: Ratios of D⁺-h correlation plots obtained by changing the sideband ranges over those obtained with standard sideband ranges. Rows: p_T(D⁺) 3-5, 5-8, 8-16, 16-24 GeV/c. In each row, the panels show the associated track p_T ranges 0.3-1, >0.3 GeV/c and >1 GeV/c, respectively.

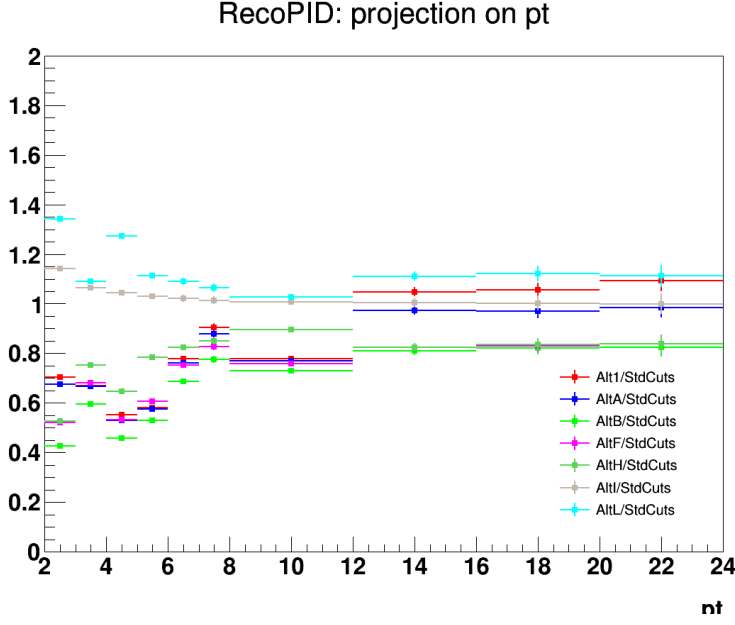


Figure 29: Ratio of D^0 efficiencies with alternate cut variations w.r.t. the standard cut used for the analysis.

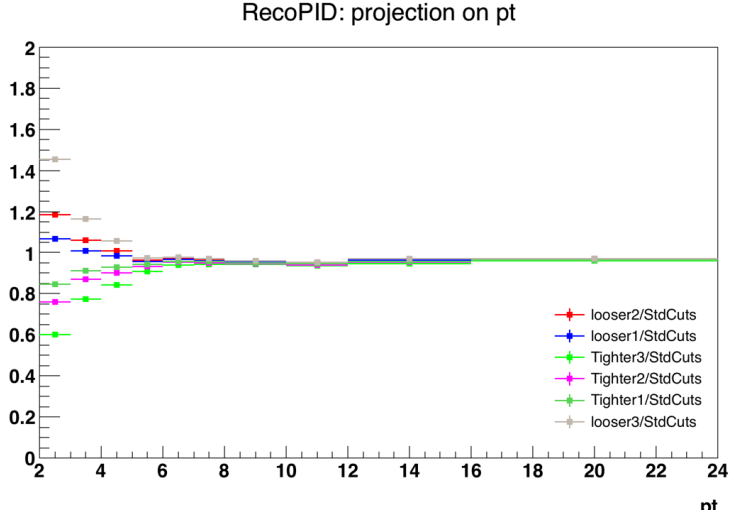


Figure 30: Ratio of D^{*+} efficiencies with alternate cut variations w.r.t. the standard cut used for the analysis.

554 4.5 Uncertainty on secondary particle contamination

555 Secondary particles, i.e. particles coming from strange hadrons decays or particles produced in inter-
 556 actions with the material, are expected to be tagged and removed by means of a distance of closest
 557 approach (DCA) from primary vertex cut. The uncertainty arising from the residual contamination of
 558 secondary tracks can be estimated from a Monte Carlo study, at reconstructed level. The number of
 559 primary/secondary tracks which are accepted/rejected from the DCA cut was determined for different
 560 values of the DCA selection, and the correlation distributions for the various cases were evaluated. The
 561 variations were done in the xy direction, where the DCA resolution is better, and the following cases
 562 were tried (in addition to the default 1 cm cut): 0.1 cm, 0.25 cm, 0.5 cm, filtering DCA cut (i.e. 2.4 cm).

563 Figure 37 shows the amount of secondary tracks which are accepted by the DCA cut, over the total
 564 number of tracks (primary and secondary) accepted by the selection, for the various DCA selections that
 565 were tried. This is shown for the exemplary case of $5 < p_T < 8 \text{ GeV}/c$ (there's no $p_T(D)$ dependence) and
 566 as a function of the associated track p_T ranges. Hence, this quantity represents the residual contamination

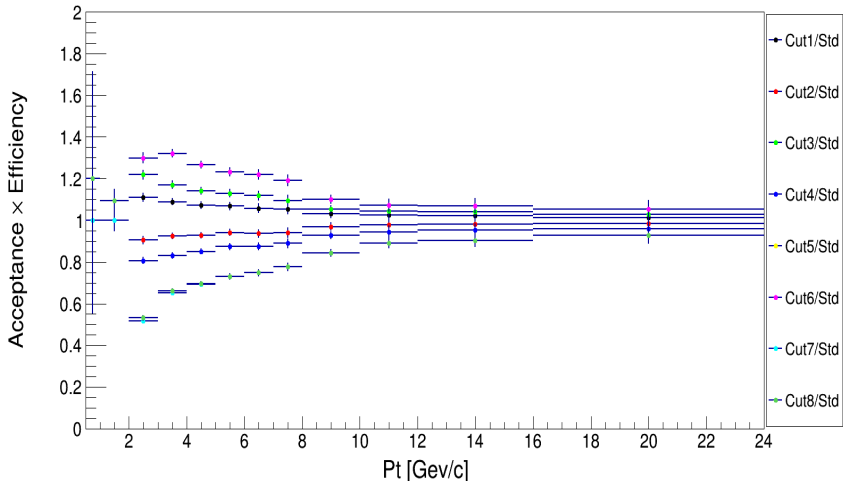


Figure 31: Ratio of D^+ efficiencies with alternate cut variations w.r.t. the standard cut used for the analysis.

of secondary tracks in our reconstructed track sample. From these values, the corresponding primary track purities (1-contamination) were extracted, in each of the momentum ranges. It was also verified that, for all the cut selections, the $\Delta\varphi$ distributions of the residual contaminations were flat within 1%.

As a second step of the procedure to verify the DCA cut stability, the D^0 -h data analysis was performed with all the different DCA selection (each time with the proper tracking efficiency map). After having extracted the correlation distributions, these were rescaled for the corresponding purities and compared with the purity-corrected correlation distributions obtained with the standard DCA selection. The ratios of the alternate selections over the standard selection, after the purity correction of both, are shown in Figures 38 and 39.

The ratios show a flat trend along the $\Delta\varphi$ axis and, in general, a discrepancy from the value of 1 of no more than 3% (the worst case being the 0.3-1 GeV/c range for the associated track). Hence, a flat and symmetric 3% systematical uncertainty on the evaluation of the secondary contamination was assigned on the base of this check in 0.3-1 GeV/c, reduced to 2.5% in > 0.3 GeV/c and to 1.5% for the other ranges. This amount also covers possible biases in the estimation of the purity (the $\Delta\varphi$ distribution of the residual contamination is always contained inside 1%, as previously said).

4.6 Uncertainty on feed-down subtraction

As described in the 3.3.5 section, the feed-down subtraction from the data distributions is performed by means of simulation templates of $B \rightarrow D$ -h correlation distributions from PYTHIA6 generator, with Perugia2011 tune, and considering the central value of f_{prompt} to extract the feed-down D-meson contribution. In order to evaluate a systematic uncertainty on this procedure, the feed-down subtraction procedure was repeated considering, together with PYTHIA6+Perugia2011 templates, also PYTHIA6+Perugia2010 and PYTHIA8 simulations. In each case, not only the central value of the measured f_{prompt} was considered to rescale the distributions, but also the maximum and minimum values of its total uncertainty.

Then, the envelope of nine the different cases obtained by varying the templates and the f_{prompt} assumption was considered, and a value of the systematics defined as the envelope spread divided by $\sqrt{3}$ was taken as systematic uncertainty. This uncertainty was assumed uncorrelated among the different $\Delta\varphi$ points.

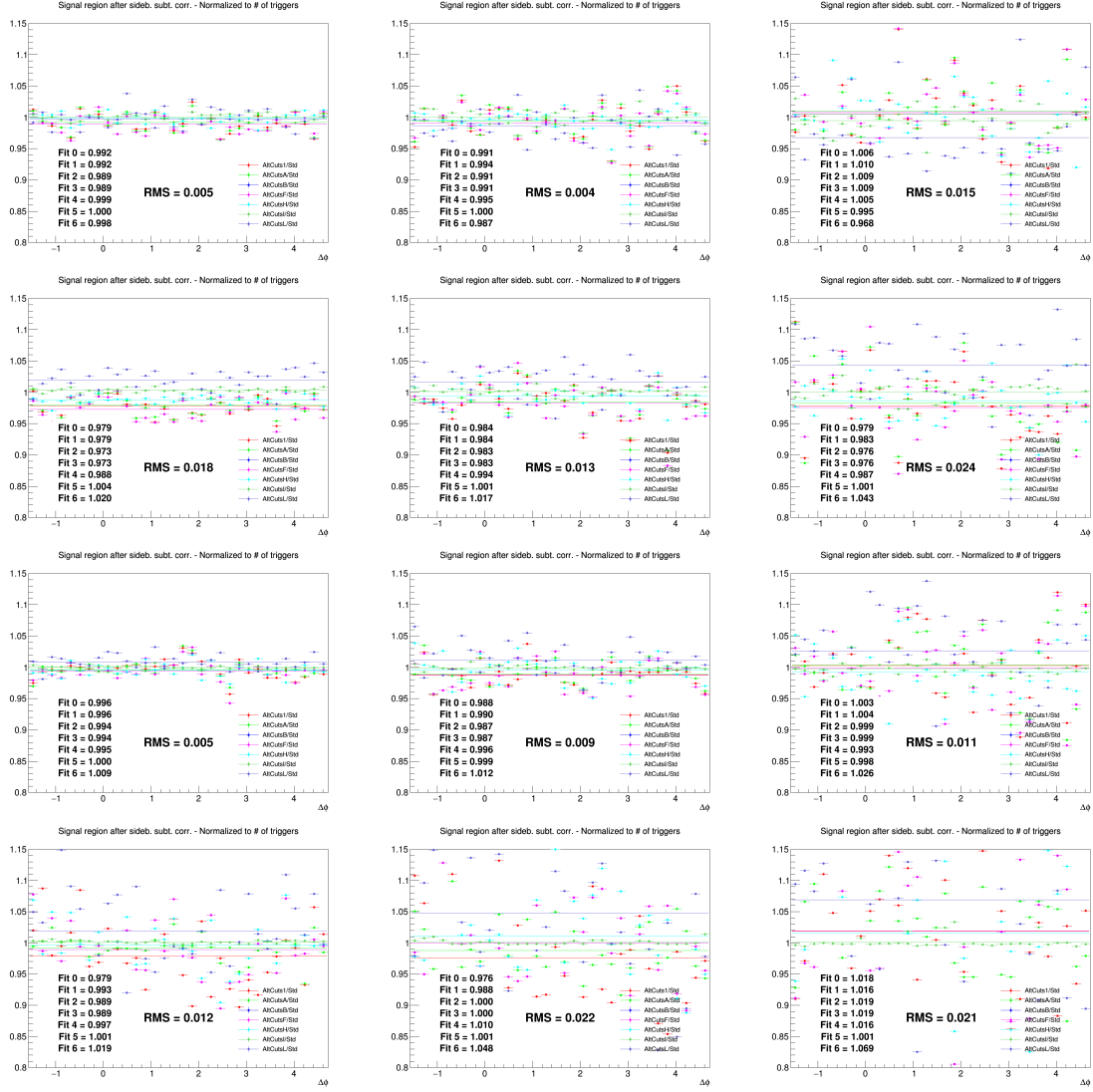


Figure 32: Ratios of D⁰-h correlation plots obtained with alternate D-meson cut sets over those obtained with standard selection. Rows: $p_T(D^0)$ 3-5, 5-8, 8-16, 16-24 GeV/ c . In each row, the panels show the associated track p_T ranges 0.3-1, 1-2, 2-3 GeV/ c , respectively.

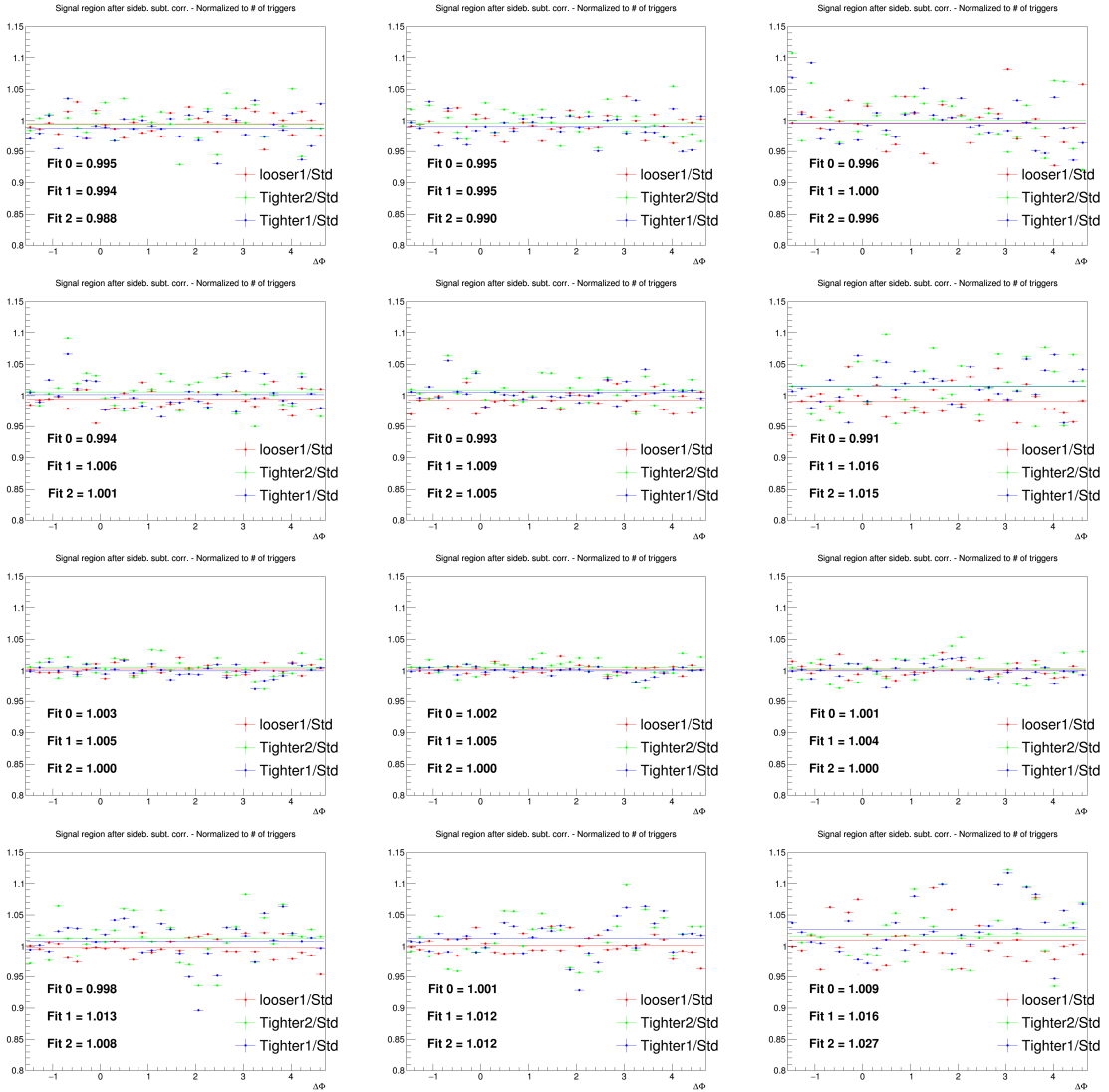


Figure 33: Ratios of D^{*+} - h correlation plots obtained with alternate D-meson cut sets over those obtained with standard selection. Rows: $p_T(D^{*+})$ 3-5, 5-8, 8-16, 16-24 GeV/c . In each row, the panels show the associated track p_T ranges 0.3-1, $>0.3 \text{ GeV}/c$, $>1 \text{ GeV}/c$, respectively.

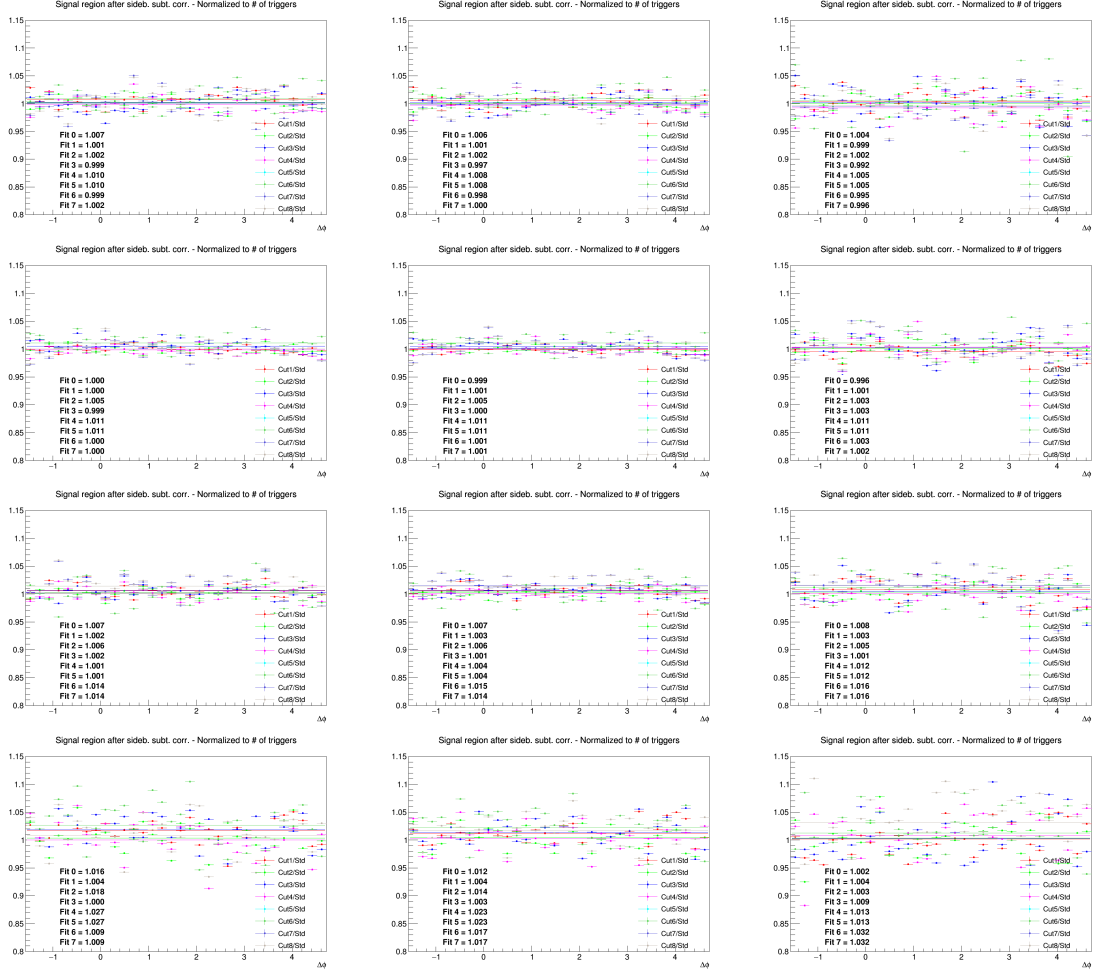


Figure 34: Ratios of D⁺-h correlation plots obtained with alternate D-meson cut sets over those obtained with standard selection. Rows: $p_T(D^+)$ 3-5, 5-8, 8-16, 16-24 GeV/c. In each row, the panels show the associated track p_T ranges 0.3-1, >0.3 GeV/c, >1 GeV/c, respectively.

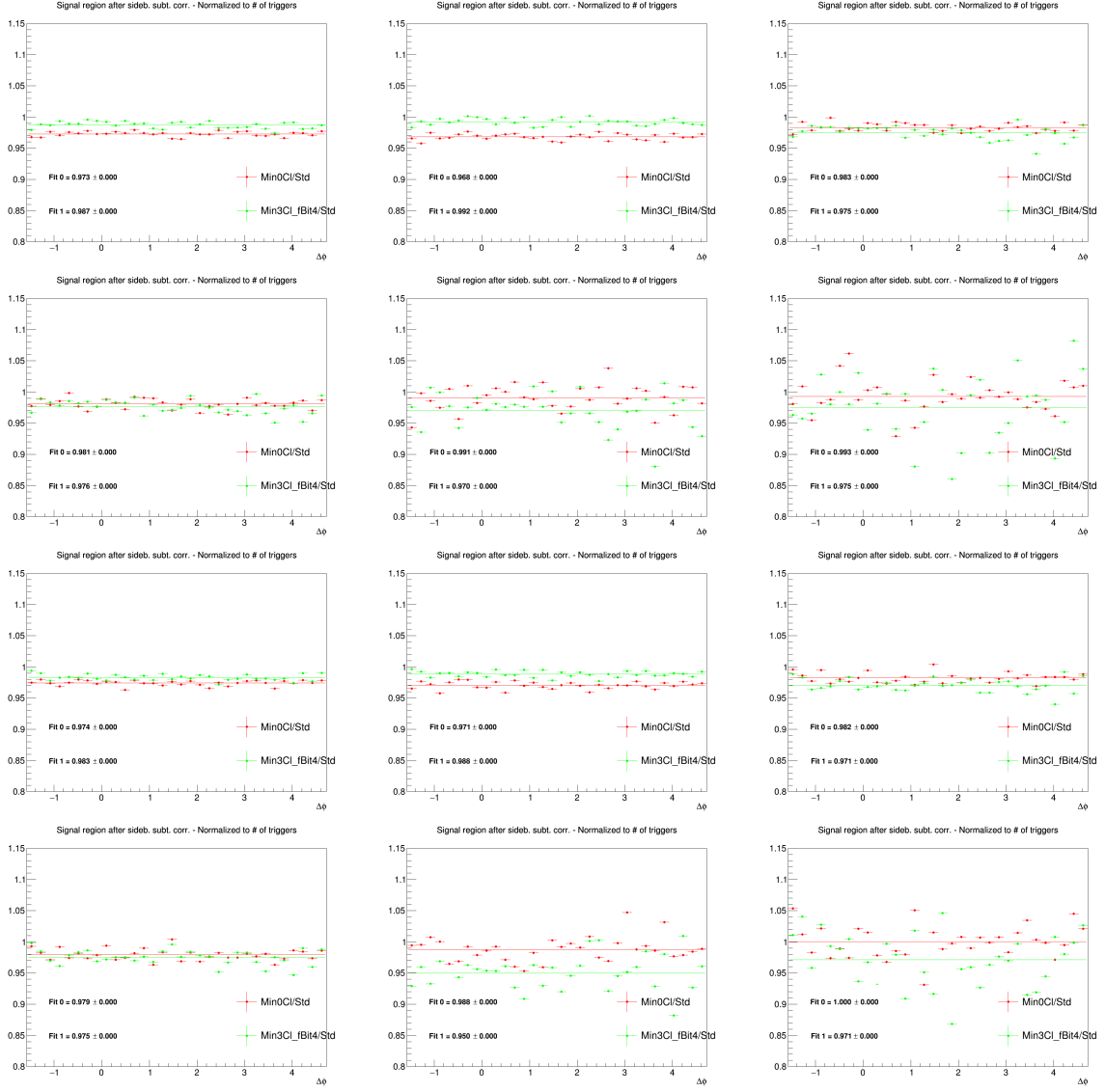


Figure 35: Ratios of D⁰-h correlation plots obtained with different associated tracks filtering selections. First 6 plots: $p_T(D)$ 3-5 GeV/c, next 6 plots: $p_T(D)$ 5-8 GeV/c. Each bunch of 6 plots has $p_T(\text{assoc})$ of >0.3, 0.3-1, >1, 1-2, 2-3, <3 GeV/c, respectively.

594 4.7 Uncertainty on correction for the bias on B to D decay topologies

595 The evaluation of this systematic uncertainty was already explained in Section 3.3.3. For each of the
 596 five data points close to the center of the near-side peak, which are affected by the bias, a bilateral and
 597 symmetric uncertainty of amplitude $|C(\Delta\phi)_{\text{corr}} - C(\Delta\phi)_{\text{raw}}|/\sqrt{12}$ was assigned.

598 This because the uncorrected data points are expected to be the extreme (with the current D-meson
 599 selection, the bias is always upwards at the centre of the peak, and always upwards on its sides). We
 600 then assume that, if the correction is properly evaluated, the corrected data points are at the centre of the
 601 possible spread of the true unbiased results. In this case, the span of the possible true results (in case
 602 of underestimation/overestimation of the bias) goes from the uncorrected data points to its symmetric
 603 value, with respect to the corrected data point, on the other direction. If this distribution is uniform,
 604 and constrained by these two values, the 1σ confidence region for the position of the is in a bilateral
 605 $|C(\Delta\phi)_{\text{corr}} - C(\Delta\phi)_{\text{raw}}|/\sqrt{12}$ window, centered on the $C(\Delta\phi)_{\text{corr}}$ points.



Figure 36: Ratios of D^0 - h correlation plots obtained with different associated tracks filtering selections. First 6 plots: $p_T(D) = 8\text{-}16 \text{ GeV}/c$, next 6 plots: $p_T(D) = 16\text{-}24 \text{ GeV}/c$. Each bunch of 6 plots has $p_T(\text{assoc})$ of >0.3 , $0.3\text{-}1$, >1 , $1\text{-}2$, $2\text{-}3$, $<3 \text{ GeV}/c$, respectively.

606 This source of uncertainty was assumed uncorrelated among the $\Delta\phi$ points.

607 4.8 Summary table

608 A summary of the $\Delta\phi$ -correlated uncertainties affecting the correlation distributions is show in Figure
609 40. They are the S and B extraction uncertainty, the background shape uncertainty, the cut variation
610 uncertainty, the tracking efficiency uncertainty and the secondary particle contamination uncertainty.

611 The overall amount of $\Delta\phi$ -correlated uncertainties is about 5-6% (depending on the p_T bin) for the single
612 D-meson cases; when evaluating the averages of the distributions (see next section), this uncertainty
613 shrinks to 4-5%. This uncertainty is a global scale factor of the distributions, and is quoted as a label in
614 the plots.

615 The systematics uncertainties from feed-down subtraction and $B\rightarrow D$ decay topology bias, instead are
616 $\Delta\phi$ dependent, and are hence reported as uncorrelated boxes in the plots. They do not amount to more
617 than 4%, in every bin of all the kinematic ranges studied.

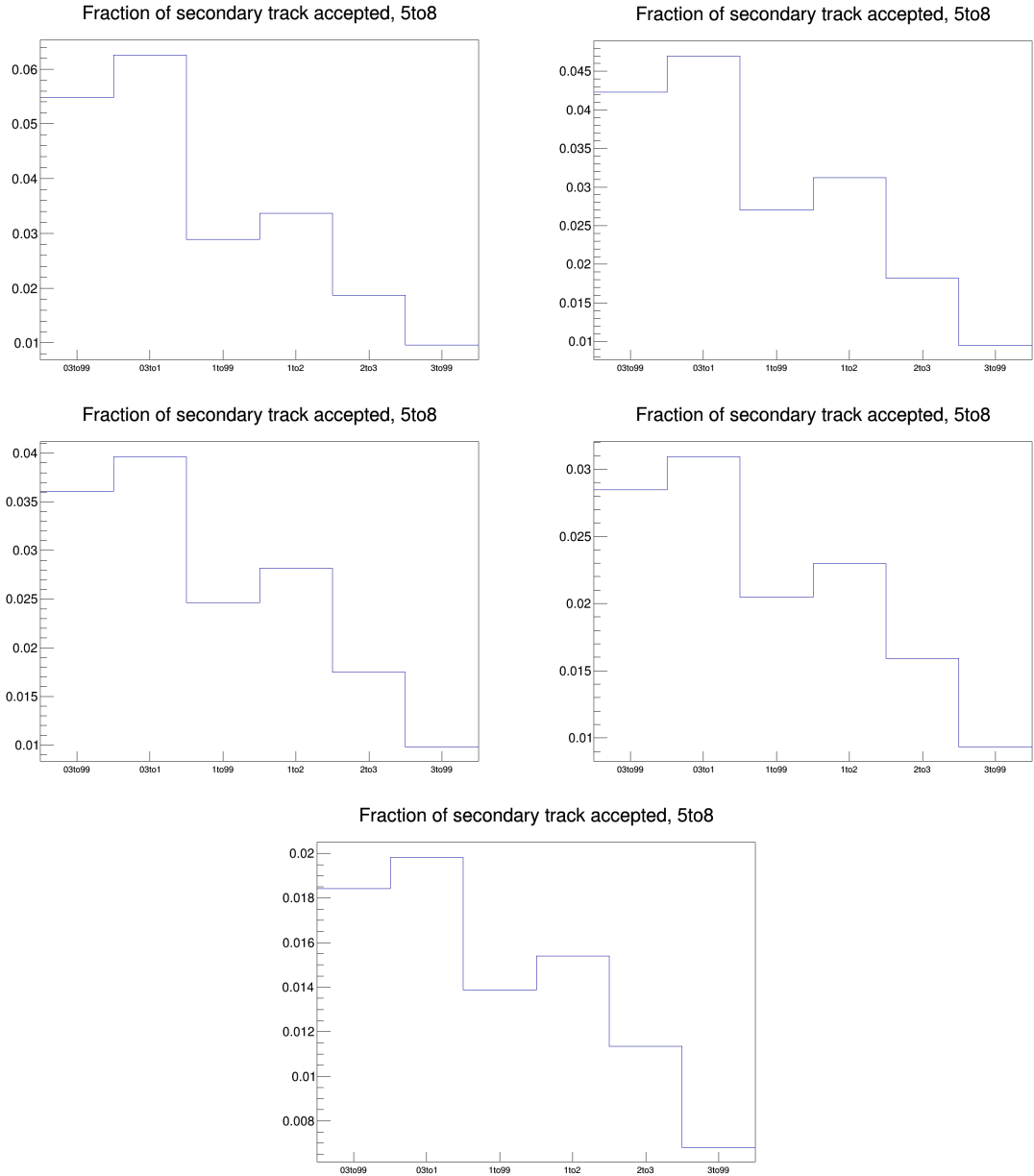


Figure 37: Secondary track contamination as a function of the associated track p_T , for the various DCA selections tried. The plots are ordered from the loosest to the tightest selection, i.e.: $\text{DCA}(xy) < 2.4 \text{ cm}$, $< 1 \text{ cm}$, $< 0.5 \text{ cm}$, $< 0.25 \text{ cm}$, $< 0.1 \text{ cm}$.

618 5 Results

619 5.1 Comparing the three D meson correlation distributions

620 To check the compatibility of three D meson analyses, Figure 41 shows the corrected azimuthal corre-
 621 lation distributions (except for the feed-down subtraction and the secondary contamination removal) for
 622 $D^0\text{-}h$, $D^{*+}\text{-}h$ and $D^+\text{-}h$, in each column, on the data sample used in the analysis. Results are shown for
 623 $3 < D p_T < 5 \text{ GeV}/c$, $5 < D p_T < 8 \text{ GeV}/c$, $8 < D p_T < 16 \text{ GeV}/c$ and $16 < D p_T < 24 \text{ GeV}/c$ with
 624 associated tracks $p_T > 0.3$, $p_T > 1$, $0.3 < p_T < 1 \text{ GeV}/c$, $1 < p_T < 2 \text{ GeV}/c$, $2 < p_T < 3 \text{ GeV}/c$ and
 625 $p_T > 3 \text{ GeV}/c$.

626 Figures 42, 43, 44, 45 show the superimposed correlation distributions from the single-meson analyses

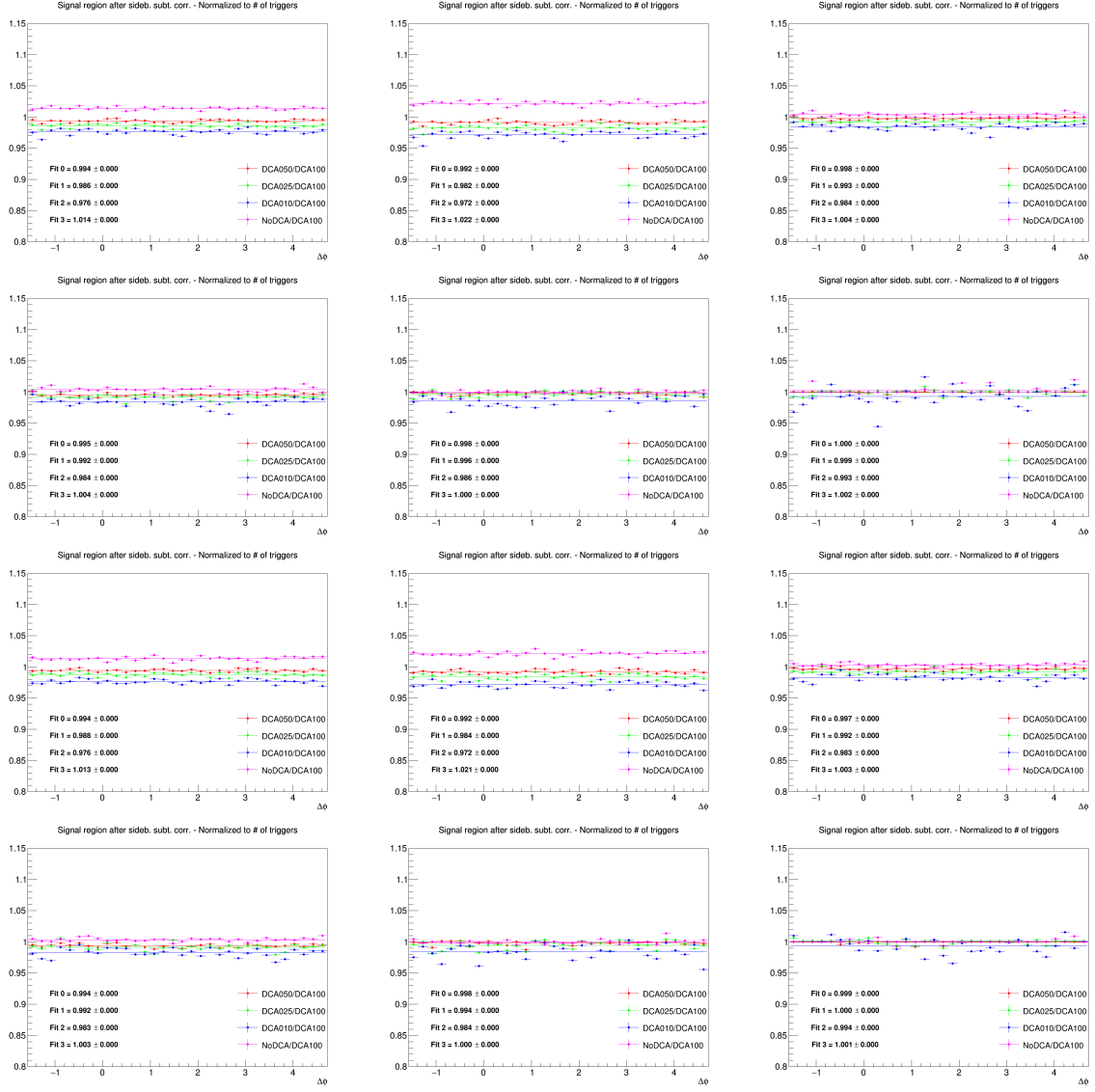


Figure 38: Ratios of correlation plots (with D^0 as trigger meson) obtained with different associated DCA selections, after purity correction. First 6 plots: $p_T(D)$ 3-5 GeV/ c , next 6 plots: $p_T(D)$ 5-8 GeV/ c . Each bunch of 6 plots has $p_T(\text{assoc})$ of >0.3 , 0.3-1, >1 , 1-2, 2-3, <3 GeV/ c , respectively.

627 (same plots as previous figure) for better visualize the agreement among the different D-meson species
628 results.

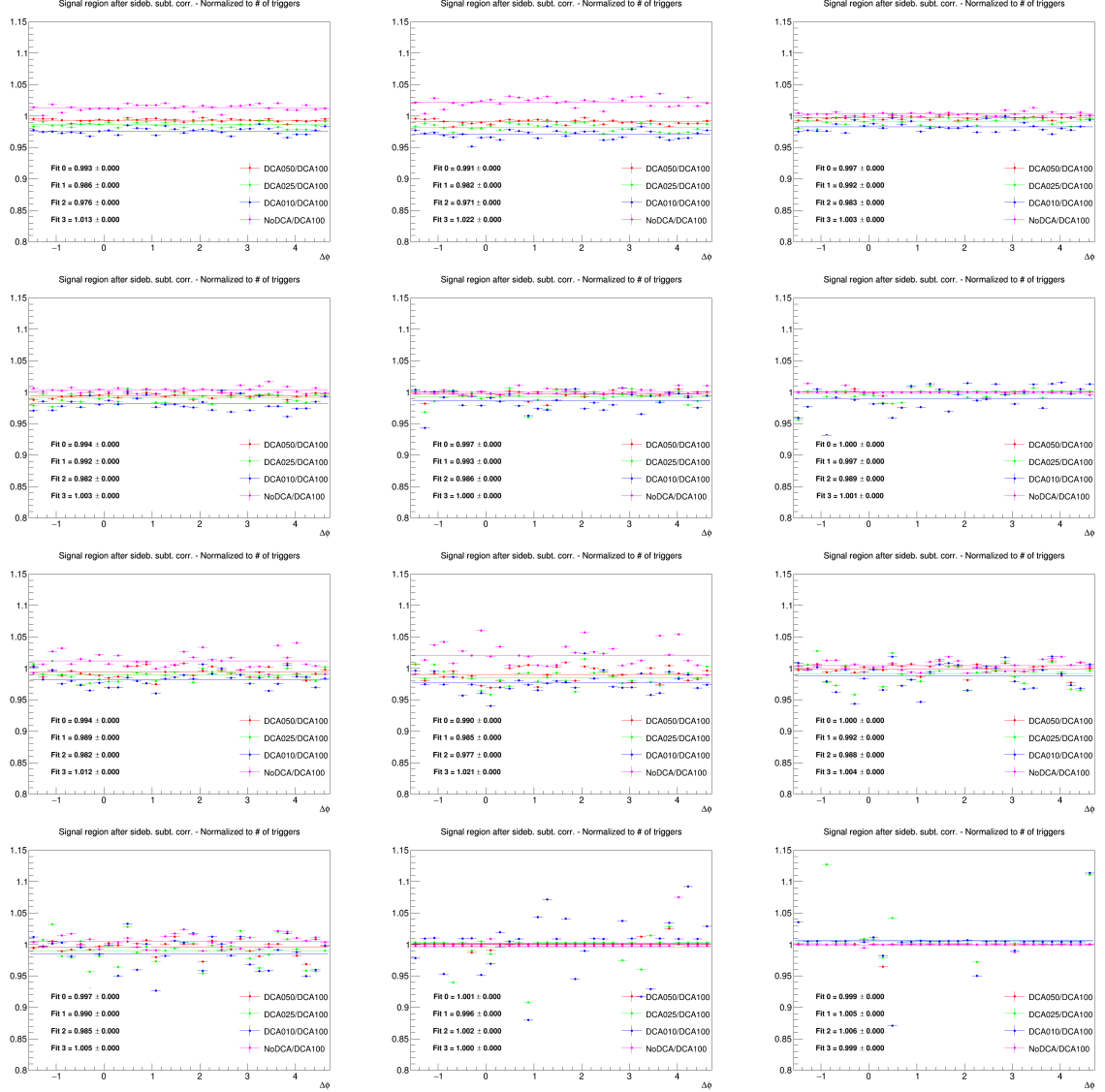


Figure 39: Ratios of correlation plots (with D^0 as trigger meson) obtained with different associated DCA selections, after purity correction. First 6 plots: $p_T(D)$ 8-16 GeV/c , next 6 plots: $p_T(D)$ 16-24 GeV/c . Each bunch of 6 plots has $p_T(\text{assoc})$ of >0.3 , $0.3-1$, >1 , $1-2$, $2-3$, $<3 \text{ GeV}/c$, respectively.

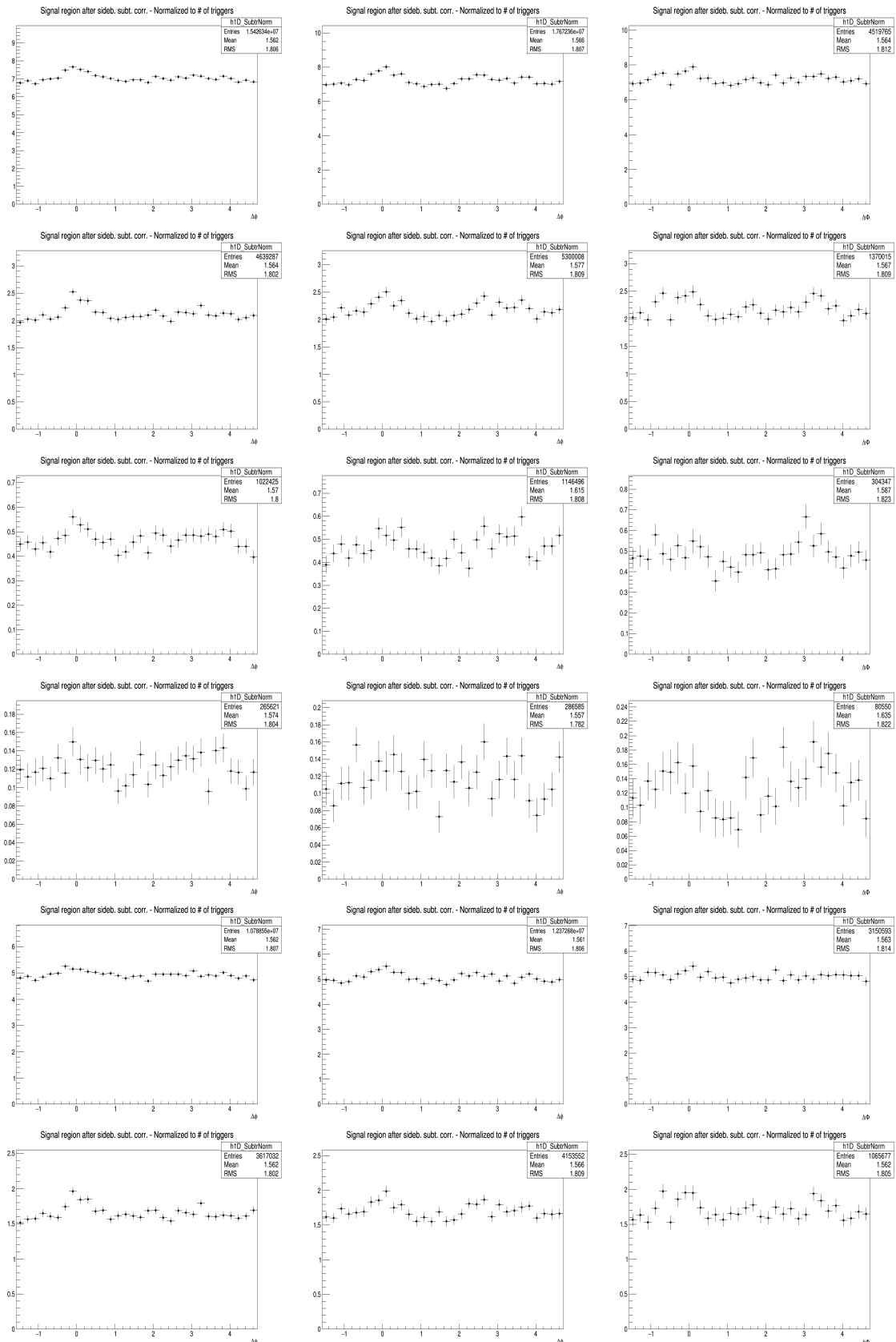
pPb Sample	D^0				D^*				D^+			
D Pt Range (GeV/c)	3-5	5-8	8-16	16-24	3-5	5-8	8-16	16-24	3-5	5-8	8-16	16-24
S and B Extraction	1%	1%	1%	3%	1%	1%	1%	2%	1%	1%	1%	2%
Background Correlation Shape	1%	1%	1%	3%	1%	1%	1%	3%	1%	1%	1%	3%
D meson Cut Variation	2%	2%	2%	2%	1.5%	1.5%	1%	1%	1%	1%	1%	3%

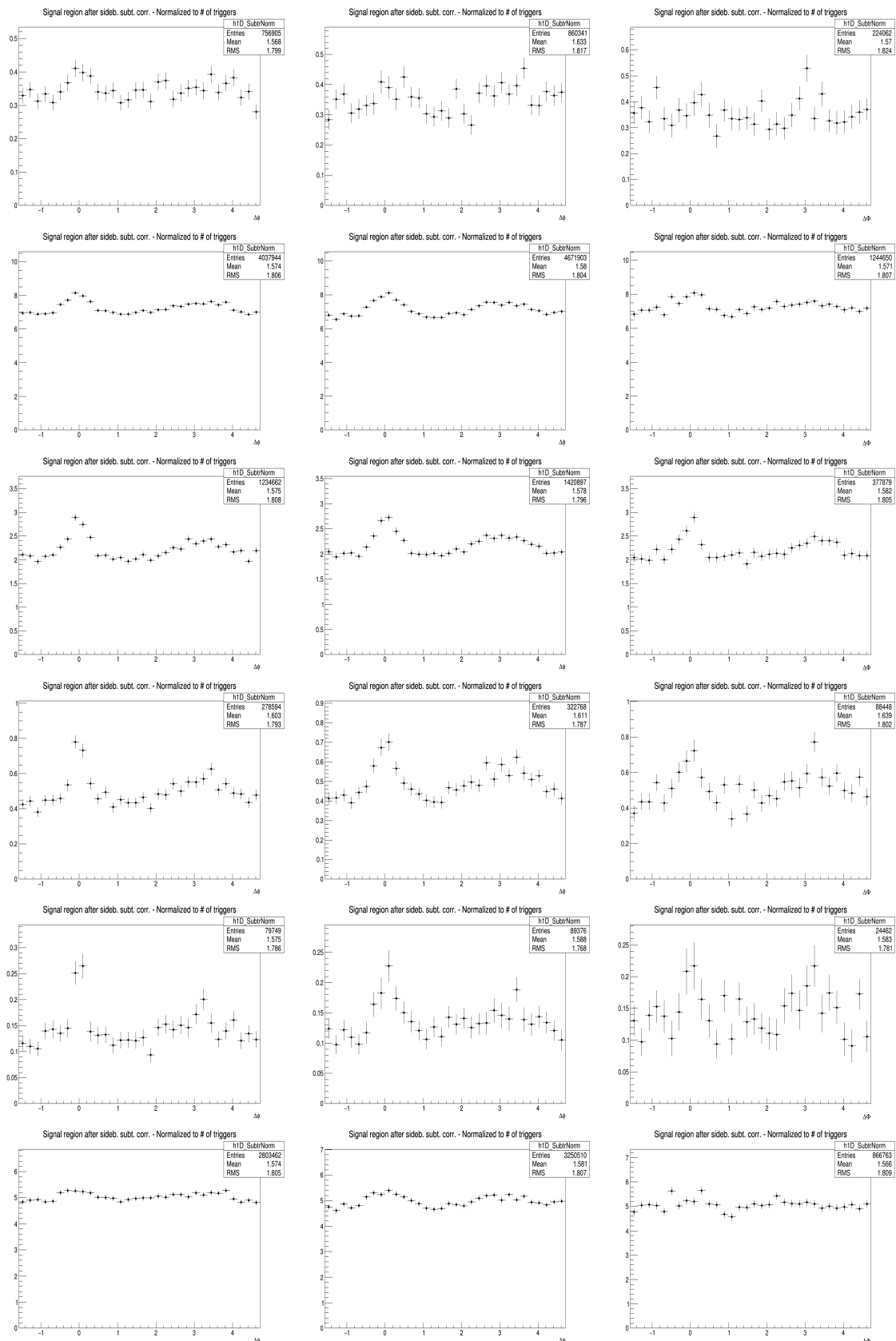
pPb Sample	D^0, D^* and D^+ (common for all the $p_T(D)$ ranges)						
Assoc (p_T) Ranges (GeV/c)	> 0.3	> 1.0	> 2.0	> 3.0	0.3-1.0	1.0-2.0	2.0-3.0
Track Efficiency	3.5%	3.5%	3.5%	3.5%	3.5%	3.5%	3.5%
Purity	2.5%	1.5%	1.5%	1.5%	3%	1.5%	1.5%

Figure 40: Summary of the $\Delta\phi$ -correlated uncertainties associated to the correlation distributions, for three D-mesons, in the different kinematic ranges of D meson and hadrons.

5.1 Comparing the three D meson correlation distributions

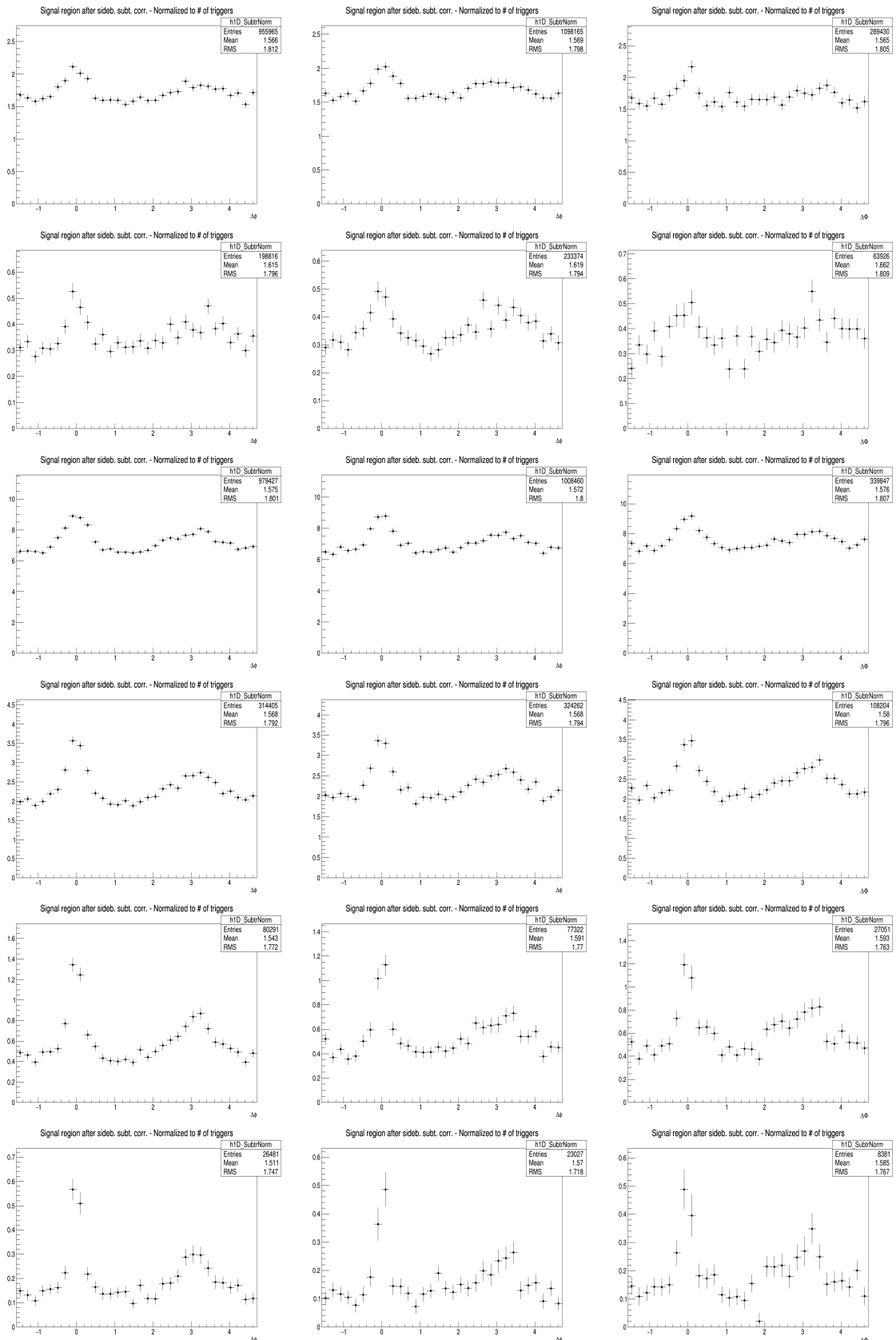
55

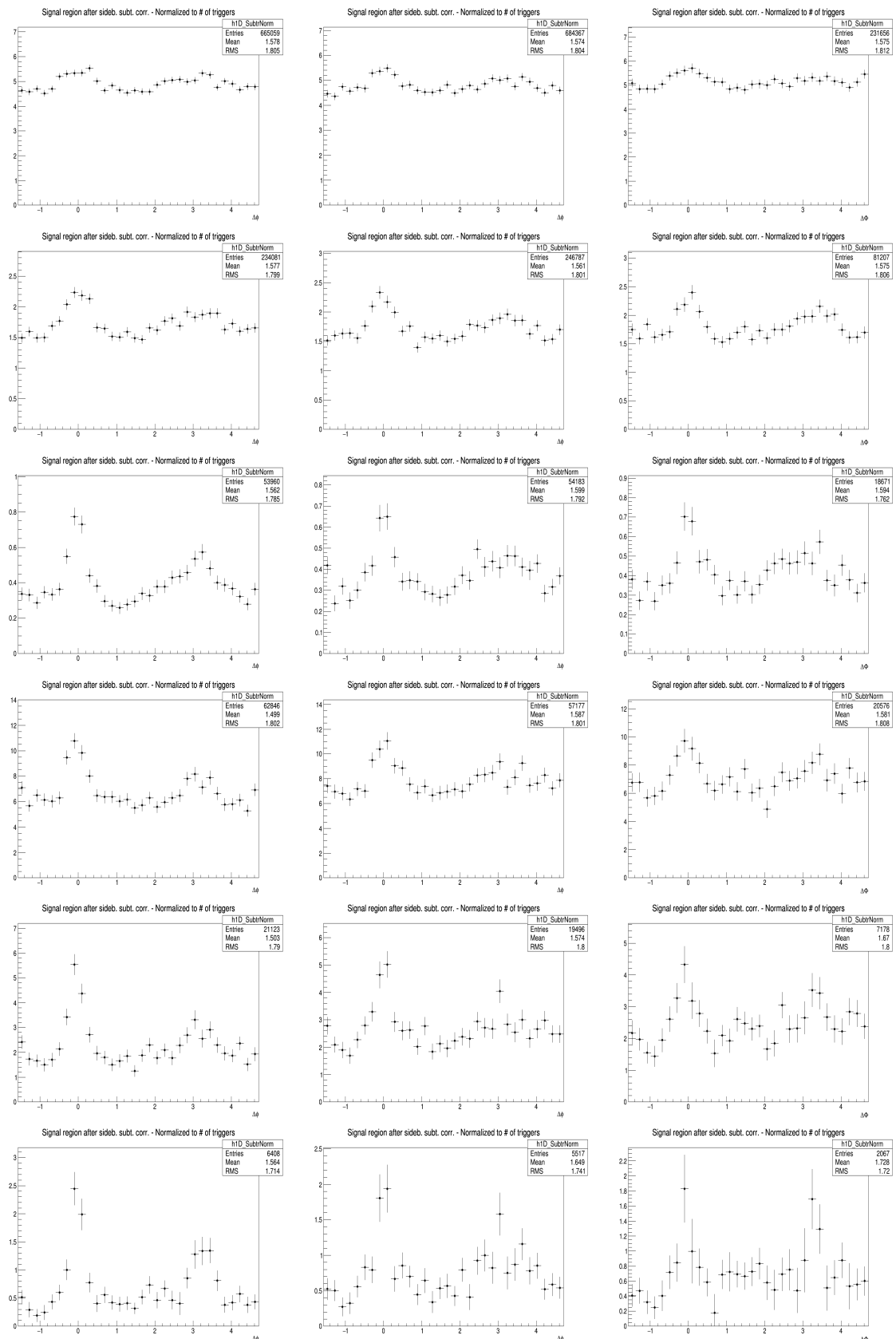




5.1 Comparing the three D meson correlation distributions

57





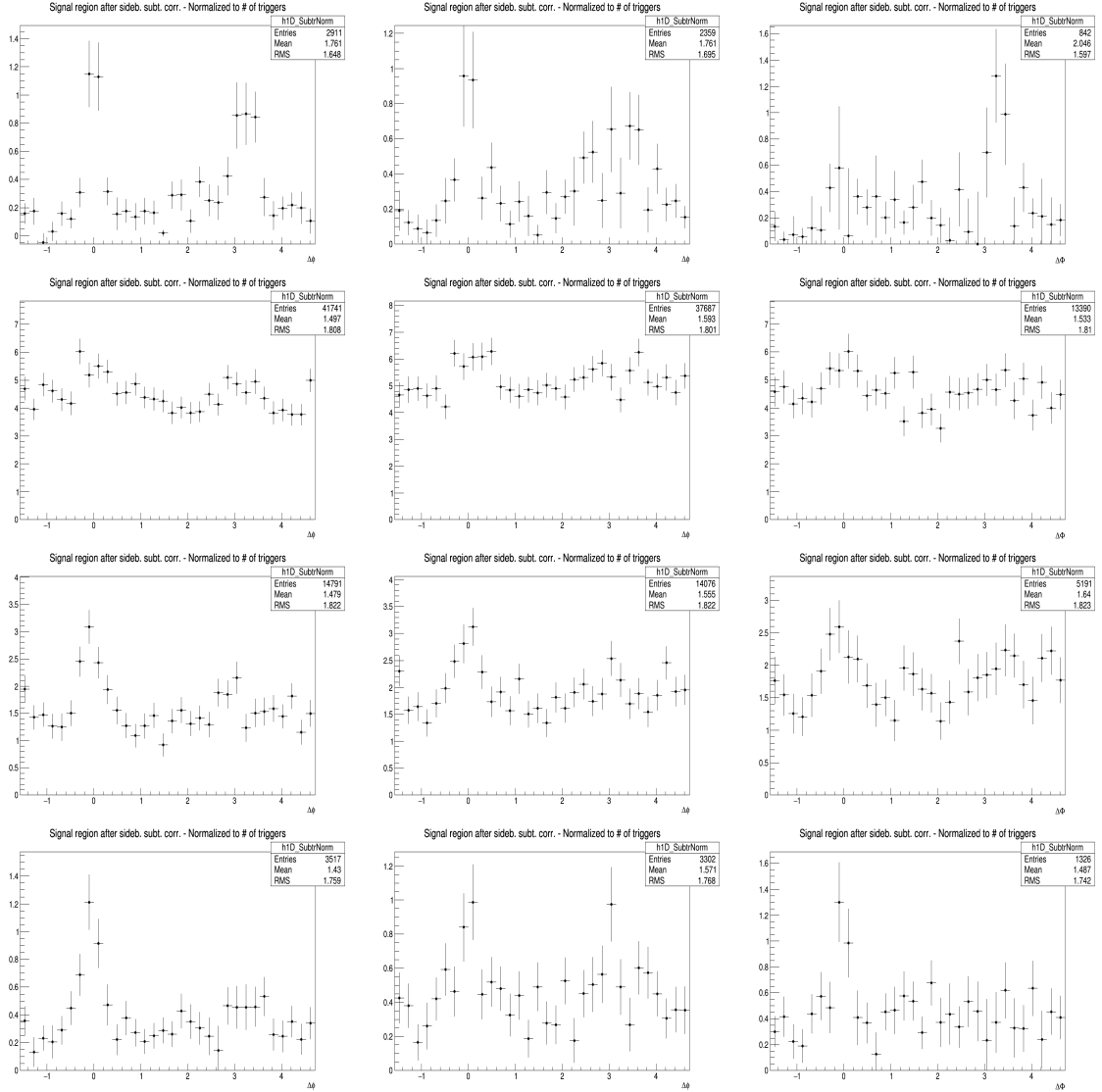


Figure 41: Corrected distribution of D-hadrons azimuthal correlations for the three species (apart from feed-down and purity), from analysis on the data sample, for the analyzed D-meson (**Column-Left:** D^0 , **Column-Middle:** D^+ and **Column-Right:** D^{*+}) and different associated tracks p_T ranges (**Row 1-7:** $3 < D_{pT} < 5 \text{ GeV}/c$, $p_T(\text{Assoc}) > 0.3, >1.0, >2.0, >3.0, 0.3-1.0, 1.0-2.0$ and $2.0-3.0 \text{ GeV}/c$ respectively), (**Row 8-14:** $5 < D_{pT} < 8 \text{ GeV}/c$, $p_T(\text{Assoc}) > 0.3, >1.0, >2.0, >3.0, 0.3-1.0, 1.0-2.0$ and $2.0-3.0 \text{ GeV}/c$ respectively), (**Row 15-21:** $8 < D_{pT} < 16 \text{ GeV}/c$, $p_T(\text{Assoc}) > 0.3, >1.0, >2.0, >3.0, 0.3-1.0, 1.0-2.0$ and $2.0-3.0 \text{ GeV}/c$ respectively) and (**Row 22-28:** $16 < D_{pT} < 24 \text{ GeV}/c$, $p_T(\text{Assoc}) > 0.3, >1.0, >2.0, >3.0, 0.3-1.0, 1.0-2.0$ and $2.0-3.0 \text{ GeV}/c$ respectively)

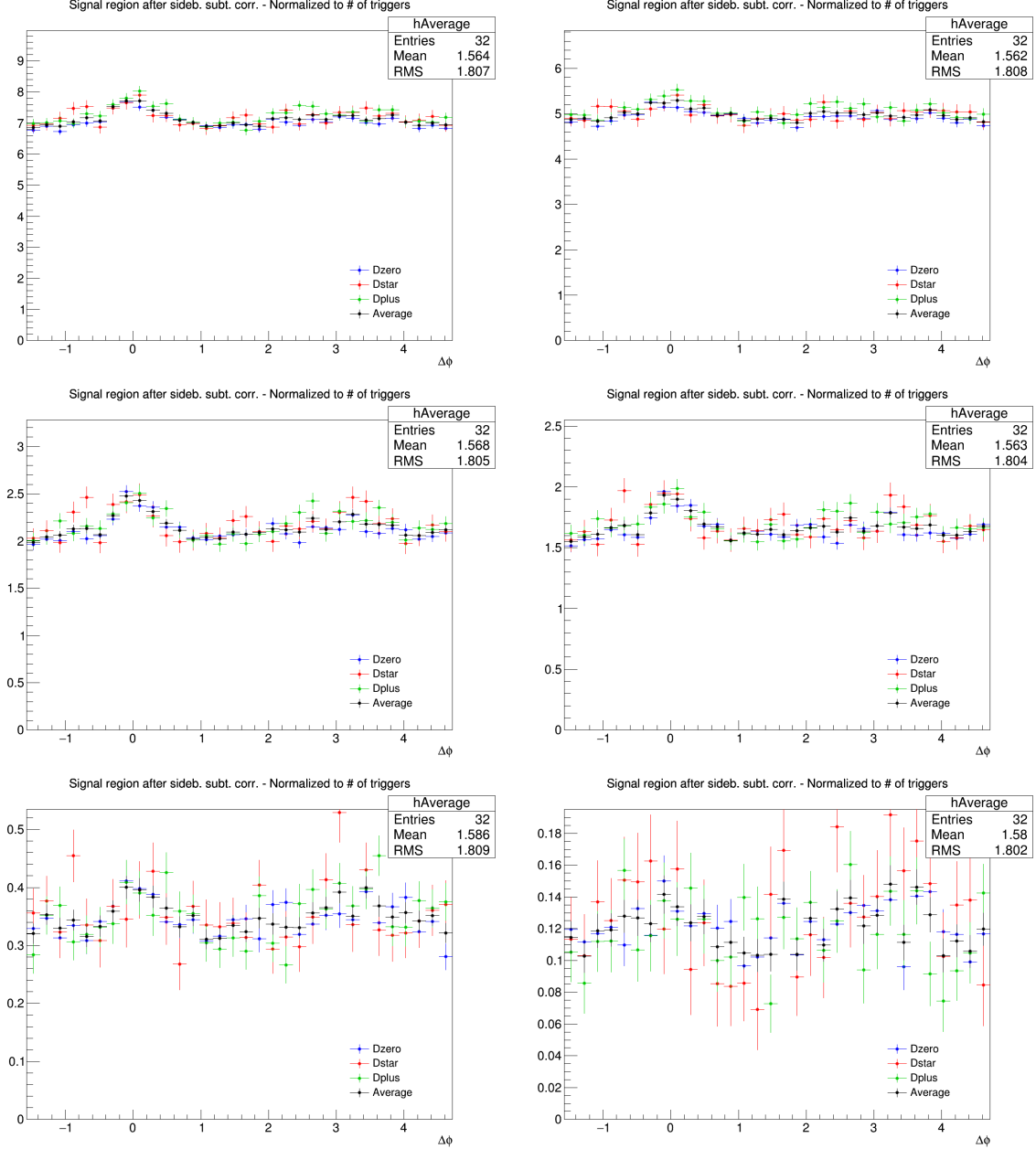


Figure 42: Superimposition of the corrected distribution of D-hadrons azimuthal correlations for the three species (apart from feed-down and purity), from analysis on the data sample, for the analyzed D-meson and different associated track p_T ranges, and D-meson p_T ranges (3-5 GeV/c on this page). **Panels from 1 to 6 of each page:** p_T (Assoc) > 0.3, 0.3-1.0, >1.0, 1.0-2.0, 2.0-3.0 and >3.0 GeV/c

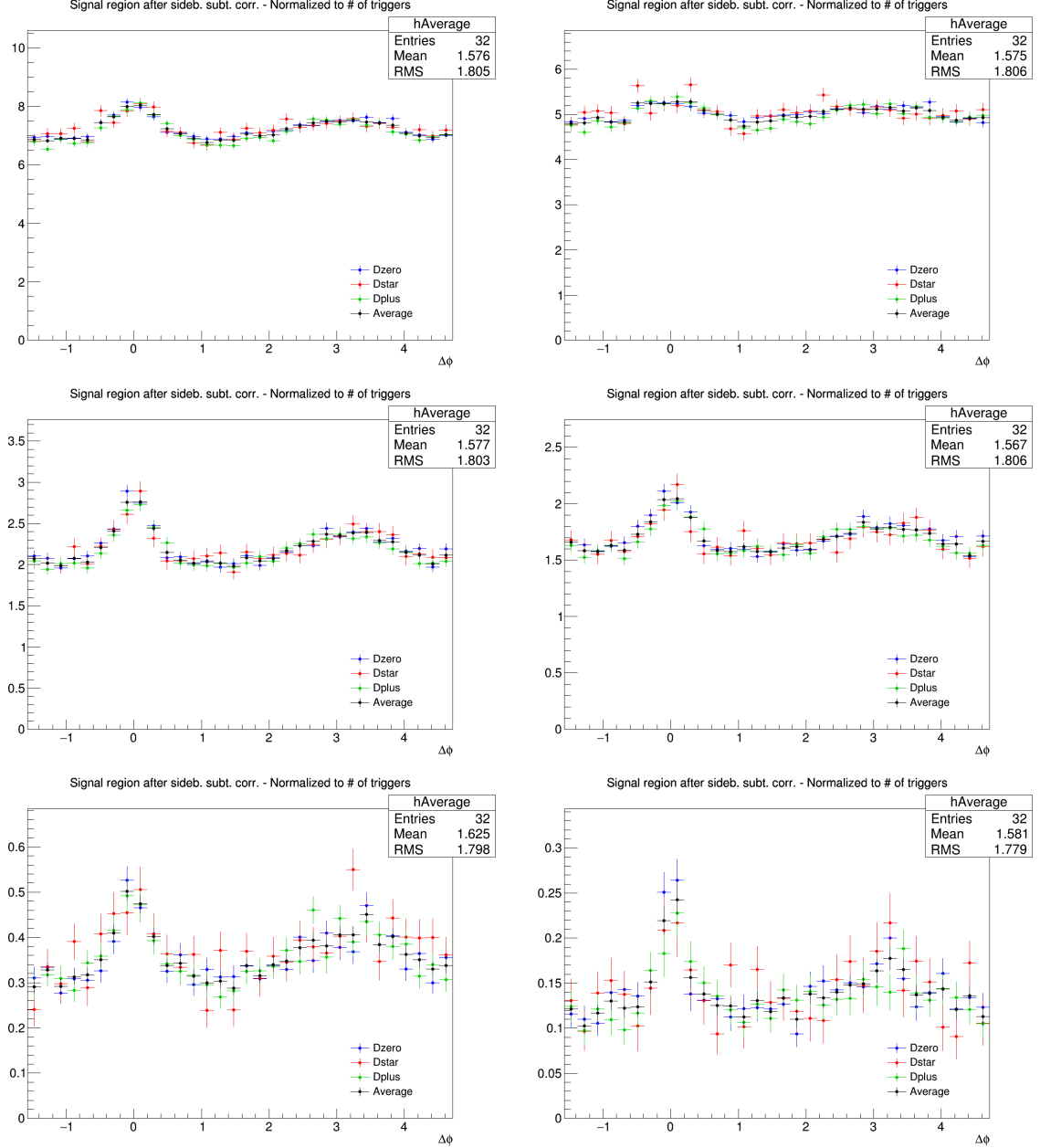


Figure 43: Superimposition of the corrected distribution of D-hadrons azimuthal correlations for the three species (apart from feed-down and purity), from analysis on the data sample, for the analyzed D-meson and different associated track p_T ranges, and D-meson p_T ranges (5-8 GeV/c on this page). **Panels from 1 to 6 of each page:** $p_T(\text{Assoc}) > 0.3, 0.3-1.0, >1.0, 1.0-2.0, 2.0-3.0$ and $>3.0 \text{ GeV}/c$

629 An agreement of the distributions from the three mesons within the uncertainties is found in all the
630 kinematic ranges.

631 Despite being evaluated in the full 2π range, the range of final results was then reduced to $[0, \pi]$ radians,
632 reflecting the points outside that range over the value of 0. This allowed to reduce the impact of statistical
633 fluctuations on the data points (supposing equal statistics for a pair of symmetric bins, after the reflection
634 the relative statistical uncertainty for the resulting bin is reduced by a factor $1/\sqrt{2}$).

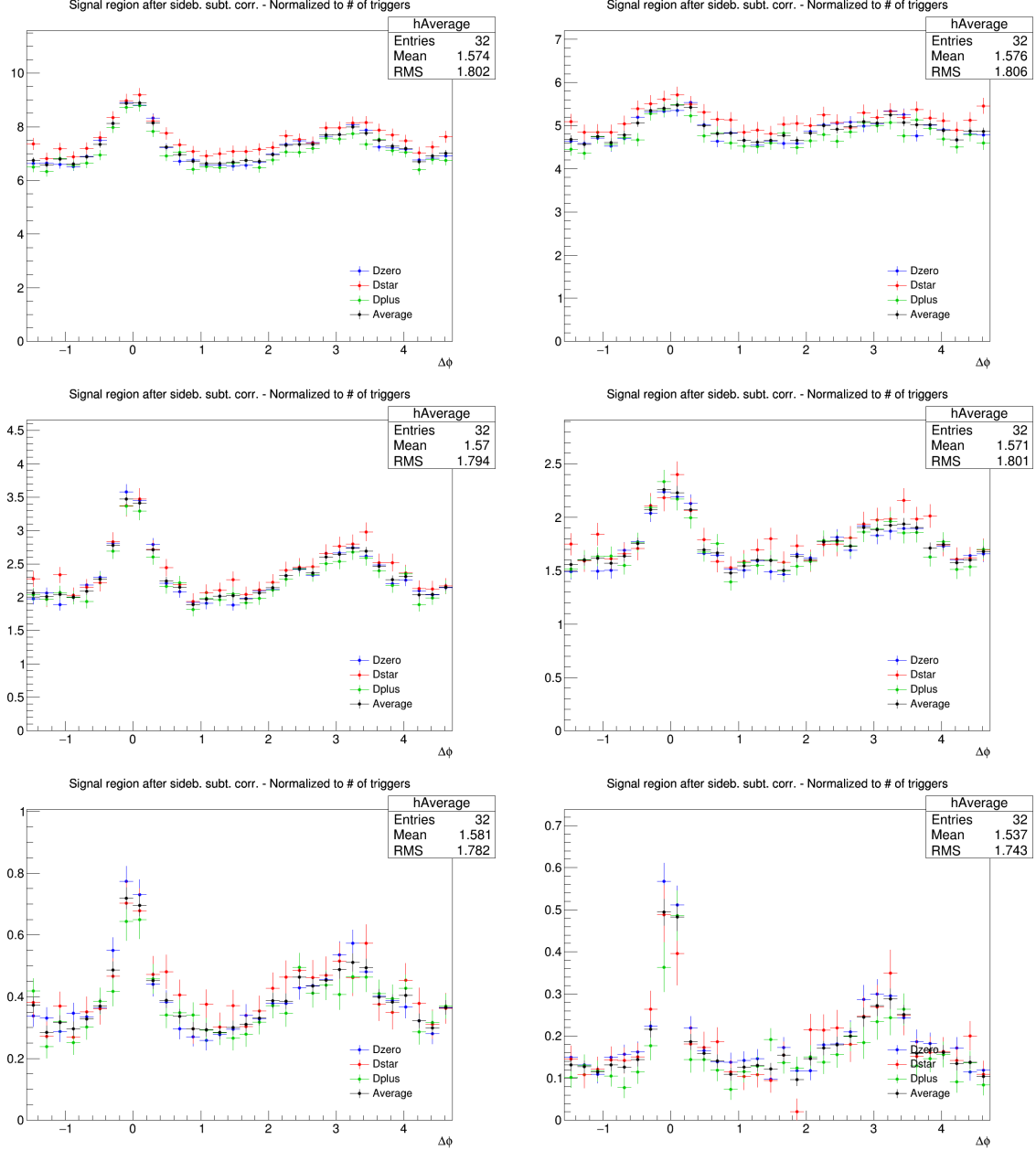


Figure 44: Superimposition of the corrected distribution of D-hadrons azimuthal correlations for the three species (apart from feed-down and purity), from analysis on the data sample, for the analyzed D-meson and different associated track p_T ranges, and D-meson p_T ranges (8-16 GeV/c on this page). **Panels from 1 to 6 of each page:** p_T (Assoc) > 0.3, 0.3-1.0, >1.0, 1.0-2.0, 2.0-3.0 and >3.0 GeV/c

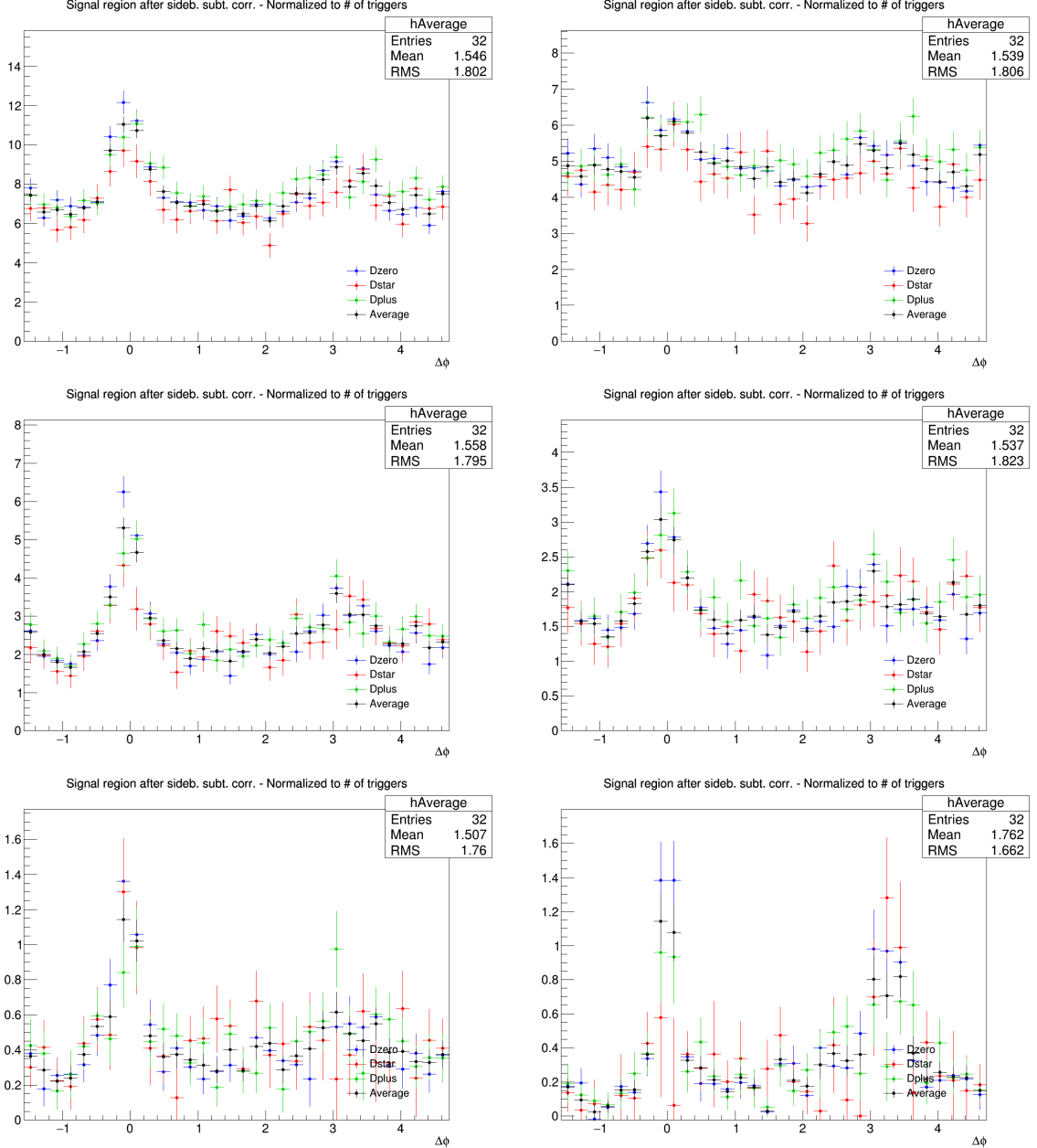


Figure 45: Superimposition of the corrected distribution of D-hadrons azimuthal correlations for the three species (apart from feed-down and purity), from analysis on the data sample, for the analyzed D-meson and different associated track p_T ranges, and D-meson p_T ranges (16-24 GeV/c on this page). **Panels from 1 to 6 of each page:** $p_T(\text{Assoc}) > 0.3, 0.3-1.0, >1.0, 1.0-2.0, 2.0-3.0$ and $>3.0 \text{ GeV}/c$

635 **5.2 Average of D⁰, D⁺ and D^{*+} results**

636 Given the compatibility within the uncertainties among the D⁰, D⁺ and D^{*+} azimuthal correlations, and
 637 since no large differences are visible in the correlation distributions observed in Monte Carlo simulations
 638 based on Pythia with Perugia0, 2010 and 2011 tunes¹, it was possible to perform a weighted average
 639 (eq. 5) of the azimuthal correlation distributions of D⁰, D⁺ and D^{*+}, in order to reduce the overall
 640 uncertainties. Although some correlation between the mesons could be present (about the 30% of the
 641 D⁰, and also part of the D⁺, come from D^{*+} decays), the three selected D-meson samples can be treated
 642 as uncorrelated. The sum of the statistical uncertainties; the systematics uncertainty on S and B extraction
 643 and on background shape, are added in quadrature and the inverse of this sum was used as weight, w_i .

$$\left\langle \frac{1}{N_D} \frac{dN_{\text{assoc}}}{dp_T} \right\rangle_{D\text{mesons}} = \frac{\sum_{i=\text{meson}} w_i \frac{1}{N_D} \frac{dN_i^{\text{assoc}}}{d\Delta\phi}}{\sum_{i=\text{meson}} w_i}, w_i = \frac{1}{\sigma_{i,\text{stat}}^2 + \sigma_{i,\text{uncorr.syst}}^2} \quad (5)$$

644 The statistical uncertainty and the uncertainties on S and B extraction and on background shape (those
 645 used for the weights) on the average were then recalculated using the following formula:

$$\sigma^2 = \frac{1}{n_D} \frac{\sum_{i=\text{meson}} w_i \sigma_i^2}{\sum_{i=\text{meson}} w_i} \quad (6)$$

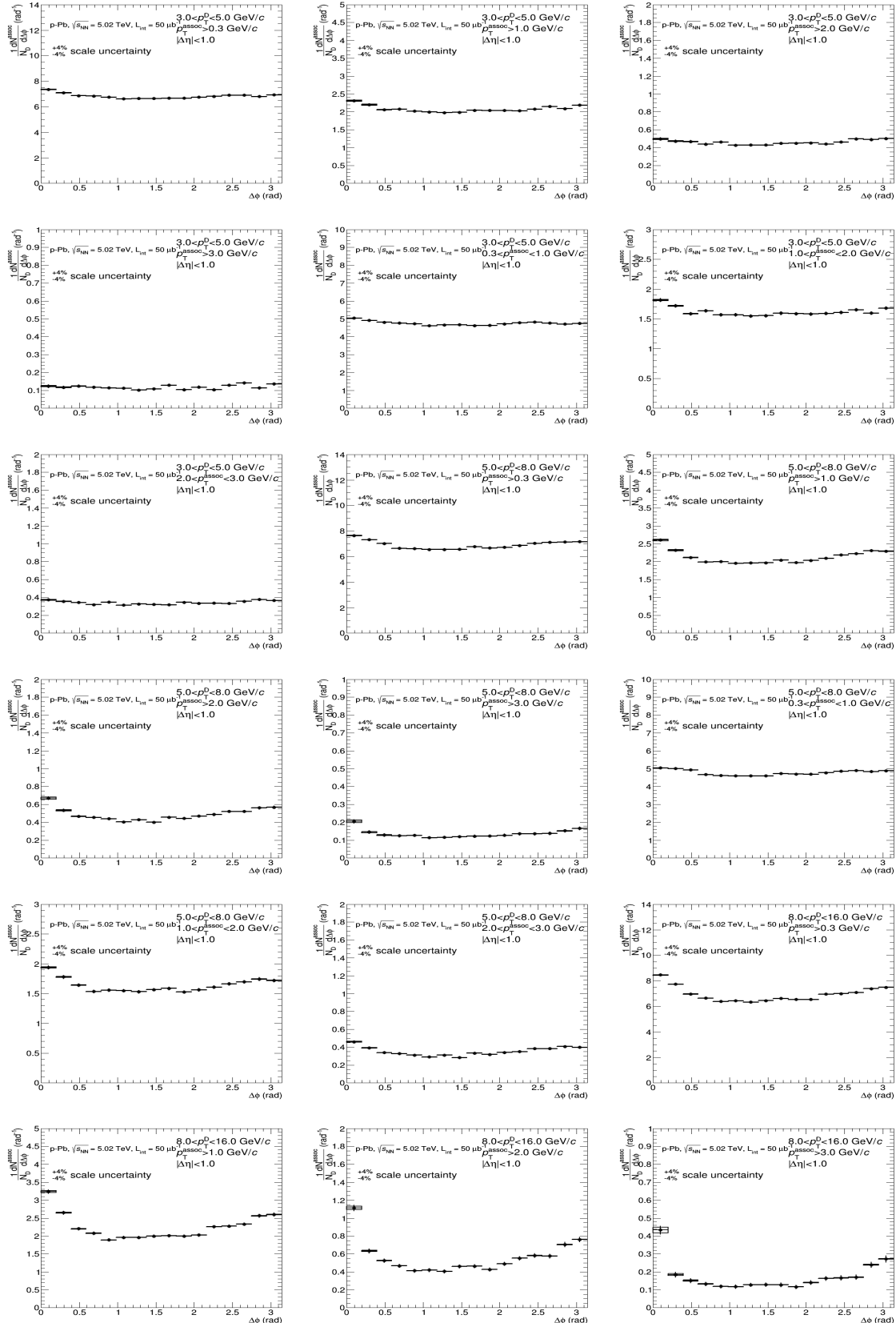
646 where n_D is the number of mesons considered in the average. It can be observed that for $\sigma_i^2 = 1/w_i$ the
 647 formula coincides with the standard one giving the uncertainty on a weighted average. The contribution
 648 to the average systematic uncertainty for those uncertainty sources not included in the weight definition,
 649 was evaluated via error propagation on the formula of the weighted average (5), resulting in equation
 650 (7) and (8) for sources considered uncorrelated and correlated among the mesons. In particular, the
 651 uncertainties on the associated track reconstruction efficiency, on the contamination from secondary, on
 652 the feed-down subtraction, and that resulting from the Monte Carlo closure test were considered fully
 653 correlated among the mesons, while those deriving from the yield extraction (included in the weight
 654 definition) and on the D meson reconstruction and selection efficiency were treated as uncorrelated.

$$\sigma^2 = \frac{\sum_{i=\text{meson}} w_i^2 \sigma_i^2}{(\sum_{i=\text{meson}} w_i)^2} \quad (7)$$

$$\sigma = \frac{\sum_{i=\text{meson}} w_i \sigma_i}{\sum_{i=\text{meson}} w_i} \quad (8)$$

655 Figure 46 shows the averages of the azimuthal correlation distributions of D⁰, D⁺ and D^{*+} and charged
 656 particles with $p_T > 0.3$ GeV/c, $0.3 < p_T < 1$ GeV/c, $p_T > 1$ GeV/c, $1 < p_T < 2$ GeV/c, $2 < p_T <$
 657 3 GeV/c, $p_T < 3$ GeV/c in the D meson p_T ranges $3 < p_T < 5$ GeV/c, $5 < p_T < 8$ GeV/c, $8 < p_T <$
 658 16 GeV/c and $16 < p_T < 24$ GeV/c. As expected, a rising trend of the height of the near-side peak
 659 with increasing D-meson p_T is observed, together with a decrease of the baseline level with increasing
 660 p_T of the associated tracks. To further increase the statistical precision on the averaged correlation
 661 distributions, given the symmetry around 0 on the azimuthal axis, the distributions were reflected and
 662 shown in the range $[0, \pi]$. This reduces the statistical uncertainty on the points by, approximately, a factor
 663 of $1/\sqrt{2}$.

¹A slight near side hierarchy is present among the three meson results, with D^{*+} meson having a lower peak amplitude than D⁰ and D⁺. It was verified that this is induced by the presence of D⁰ and D⁺ mesons coming from D^{*+}, the latter having on average a larger p_T and coming, hence, on average, from a larger p_T quark parton, which fragments in slightly more tracks in the near-side.



664 The usage of weighted average requires, as an underlying assumption, identical results expected for
 665 different species (or, at least, compatible within the uncertainties). Anyway, it was also verified that the
 666 usage of the arithmetic average instead of the weighted average increases the uncertainties on the points,

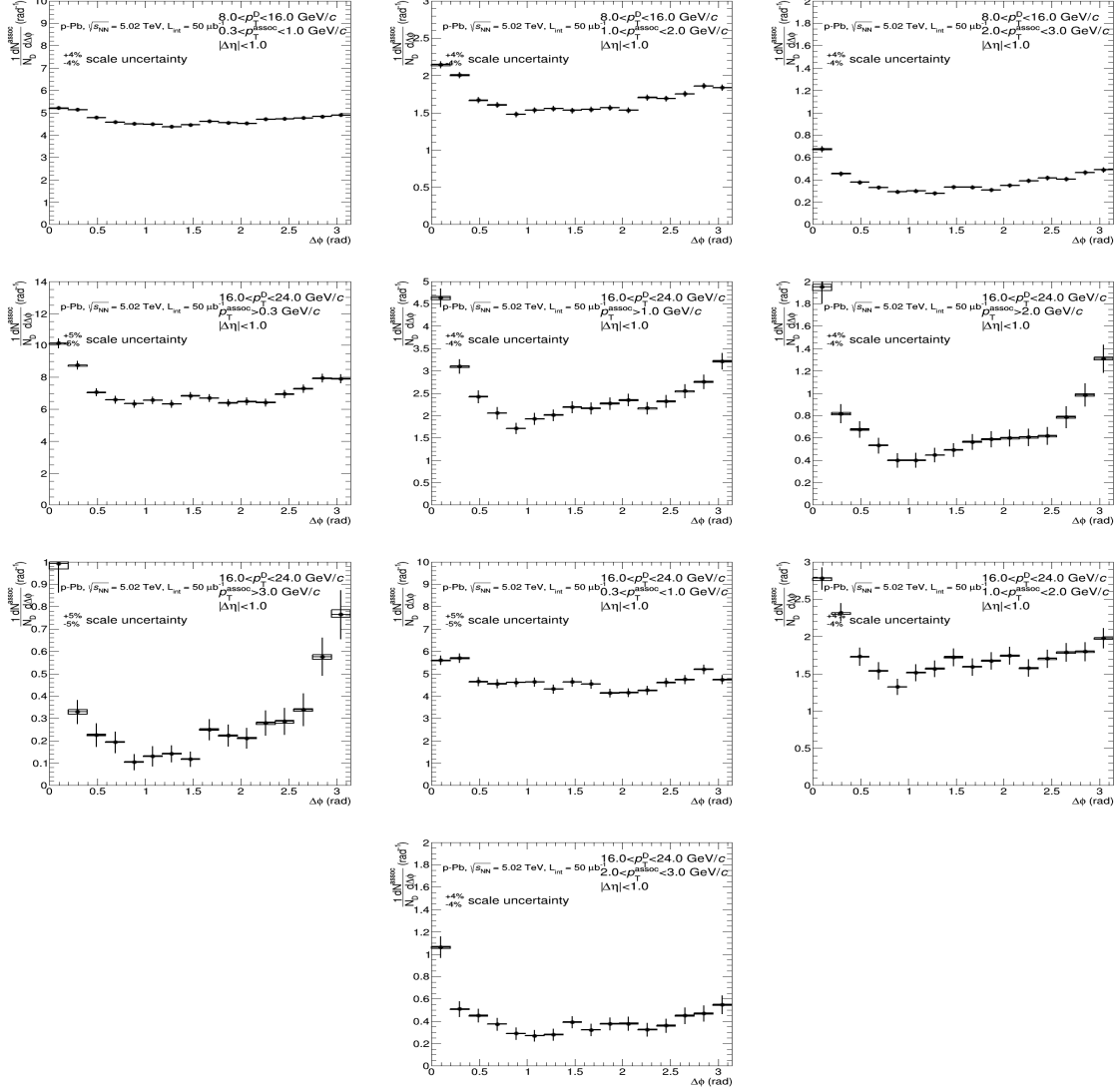


Figure 46: Average of D^0 , D^+ and D^{*+} azimuthal correlation distributions, in the D meson p_T ranges $3 < p_T < 5 \text{ GeV}/c$, $5 < p_T < 8 \text{ GeV}/c$, $8 < p_T < 16 \text{ GeV}/c$ and $16 < p_T < 24 \text{ GeV}/c$, with associated tracks with $p_T > 0.3 \text{ GeV}/c$, $p_T > 1 \text{ GeV}/c$ and $0.3 < p_T < 1 \text{ GeV}/c$.

667 but produces a negligible shift of their central values.

668 5.3 Fit observable p_T trends and uncertainties

669 In order to extract quantitative and physical information from the data correlation patterns, the averaged
 670 D-h correlation distributions are fitted with two Gaussian functions (with means fixed at $\Delta\varphi=0$ and $\Delta\varphi=\pi$
 671 values), plus a constant term (baseline). A periodicity condition is also applied to the fit function to obtain
 672 the same value at the bounds of 2π range. The expression of the fit function is reported below (equation
 673 9):

$$f(\Delta\varphi) = c + \frac{Y_{NS}}{\sqrt{2\pi}\sigma_{NS}} e^{-\frac{(\Delta\varphi-\mu_{NS})^2}{2\sigma_{NS}^2}} + \frac{Y_{AS}}{\sqrt{2\pi}\sigma_{AS}} e^{-\frac{(\Delta\varphi-\mu_{AS})^2}{2\sigma_{AS}^2}} \quad (9)$$

674 where baseline is calculated as the weighted average of the points lying in the so-called "transverse
 675 region", i.e. the interval $\frac{\pi}{4} < |\Delta\varphi| < \frac{\pi}{2}$.

676 An example of the results from the fit is shown in Figure 47

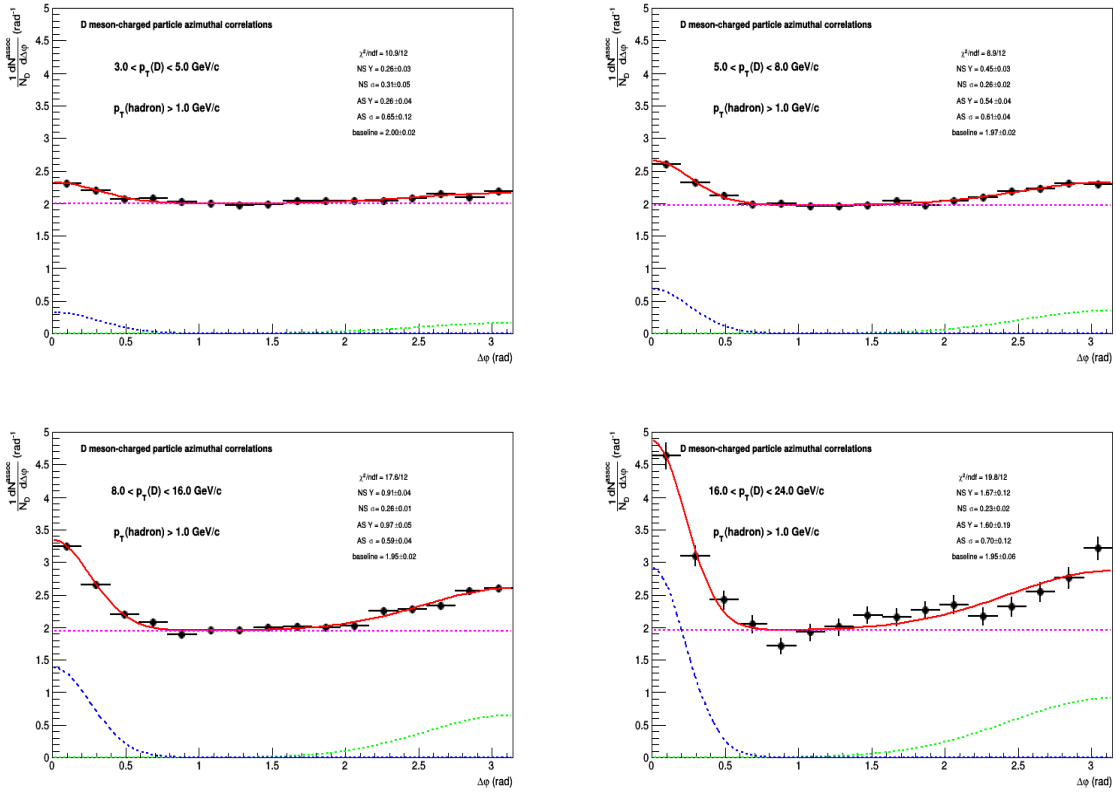


Figure 47: Example of fit to azimuthal correlation distributions and baseline estimation.

677 From the fit outcome, it is possible to retrieve the near-side and away-side yield and widths (integral
 678 and sigma of the Gaussian functions, respectively), as well as the baseline height of the correlation
 679 distribution. The near-side observables give information on the multiplicity and angular spread of the
 680 tracks from the fragmentation of the charm jet which gave birth to the D-meson trigger. At first order,
 681 instead, the away-side observables are related to the hadronization of the charm parton produced in the
 682 opposite direction (though the presence of NLO processes for charm production breaks the full validity
 683 of this assumption). The baseline value is a rough indicator of the underlying event multiplicity, though

below the baseline level also charm and beauty-related pairs are contained (especially in cases of NLO production for the heavy quarks).

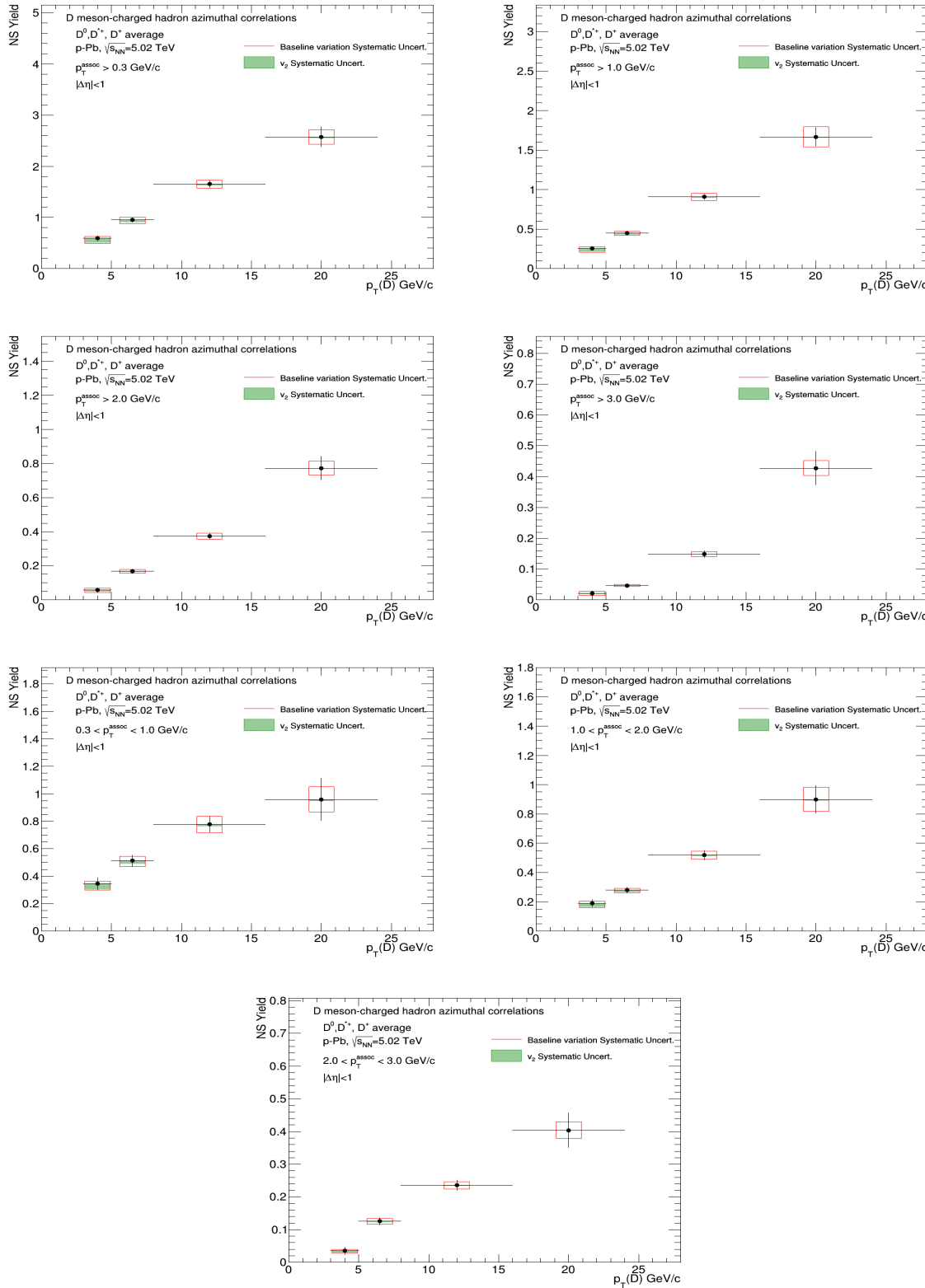
The evaluation of the systematic uncertainties on the observables obtained from the fits is performed as follows:

- The fits are repeated by changing the range of the transverse region in which the baseline is evaluated. Alternate definitions of $\frac{\pi}{4} < |\Delta\phi| < \frac{3\pi}{8}$, $\frac{3\pi}{8} < |\Delta\phi| < \frac{\pi}{2}$ and $\frac{\pi}{4} < |\Delta\phi| < \frac{5\pi}{8}$ are considered.
- In addition, $\Delta\phi$ correlation points are shifted to the upper and lower bounds of their uncorrelated systematic boxes, and refitted.
- The maximum variation of the parameters between the fit outcomes defined in the previous points is considered as systematic uncertainty for the near-side and away-side widths.
- For the estimation of the baseline and of the near-side and away-side yields, the previous value is added in quadrature with the $\Delta\phi$ -correlated systematics in the correlation distributions, since these values are affected by a change in the global normalization of the distributions.
- In addition, for all the fit observables, another fit variation is performed assuming, instead of a flat baseline, a $v_{2\Delta}$ -like modulation, with the following v_2 values for the associated tracks (assuming $v_{2\Delta} = v_2(h) \cdot v_2(D)$): 0.04 (0.3-1 GeV/c), 0.06 (>0.3 GeV/c), 0.08 (1-2 GeV/c), 0.09 (>1 GeV/c, 2-3 GeV/c), 0.1 (>3 GeV/c), on the basis of ATLAS preliminary results for heavy-flavour muons at 8 TeV; for the D-meson triggers the following v_2 values were instead assumed: 0.05 (3-5 GeV/c), 0.03 (5-8 GeV/c), 0.02 (8-24 GeV/c), on the basis of previous ALICE measurements in p-Pb collisions at 5 TeV [2]. The difference of the fit observables with respect to the standard fits is taken as uncertainty. Due to its peculiarity, this systematic uncertainty is summed in quadrature with the others to obtain the total uncertainty, but is also shown separately in the figures.

$$\sigma^{syst} = \sqrt{(Max(\Delta par^{ped.mode}, \Delta par^{\Delta\phi point}))^2 + (\sigma_{Syst}^{corr})^2} \quad (10)$$

5.3.1 Results for near-side yield and width, away-side yield and width, and baseline

Figures 48, 49, 50, 51 and 52 show the near-side associated yield, width (the sigma of the Gaussian part of the fit functions), away-side associated yield, width and the height of the baseline, for the average correlation distributions, in the kinematic ranges studied in the analysis, together with their statistical and systematic uncertainties. For each kinematic range, the correspondent plot showing the systematic uncertainty of the considered observable from the variation of the fit procedure is reported as well (which is the full systematic uncertainty for the widths). Figures 53, 54, 55, 56 and 57 show the full systematic uncertainties for near side yield and width, away side yield and width, and baseline, with the breakdown of fit variation, $v_{2\Delta}$ and $\Delta\phi$ correlated systematic uncertainties.



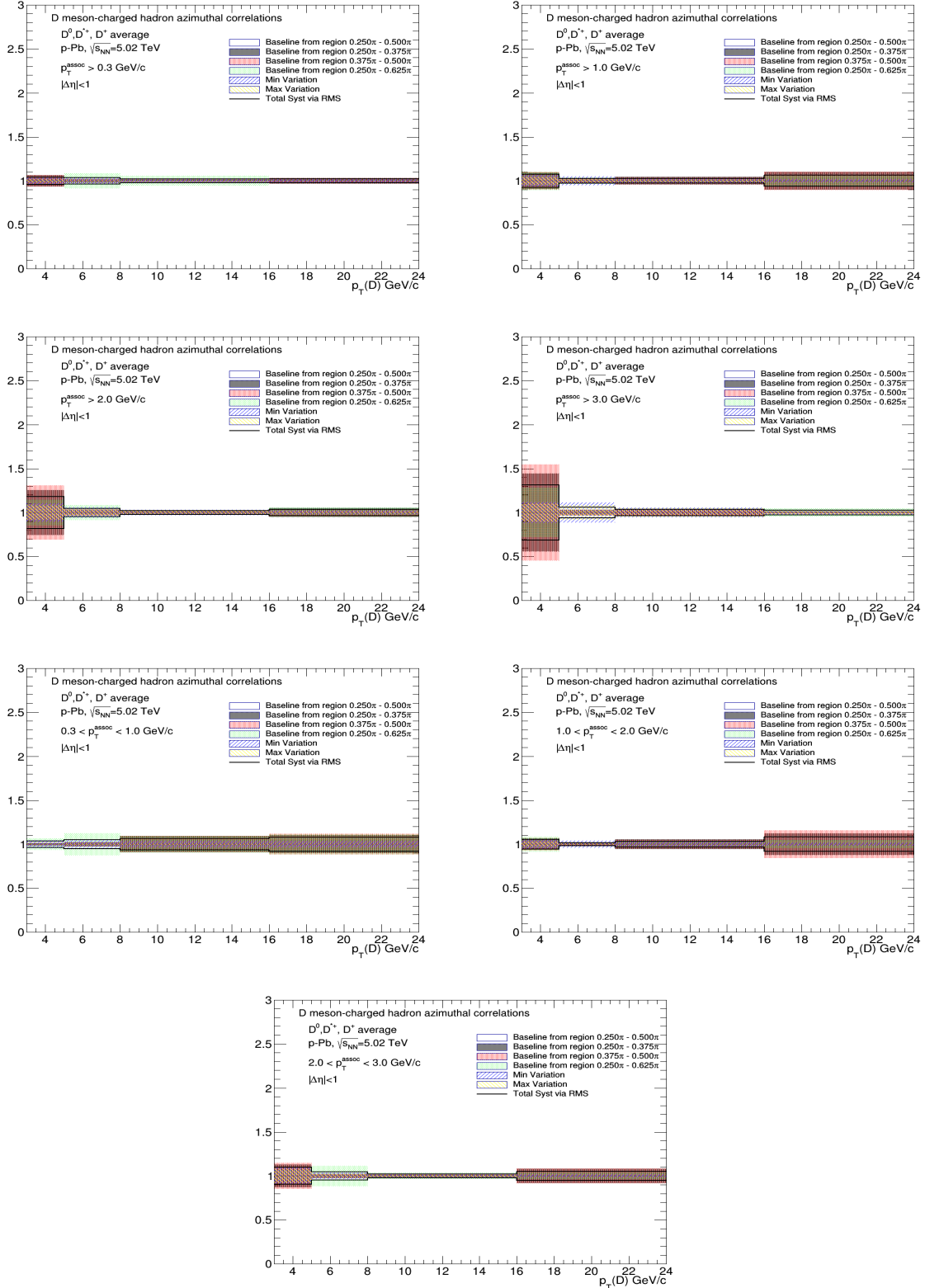
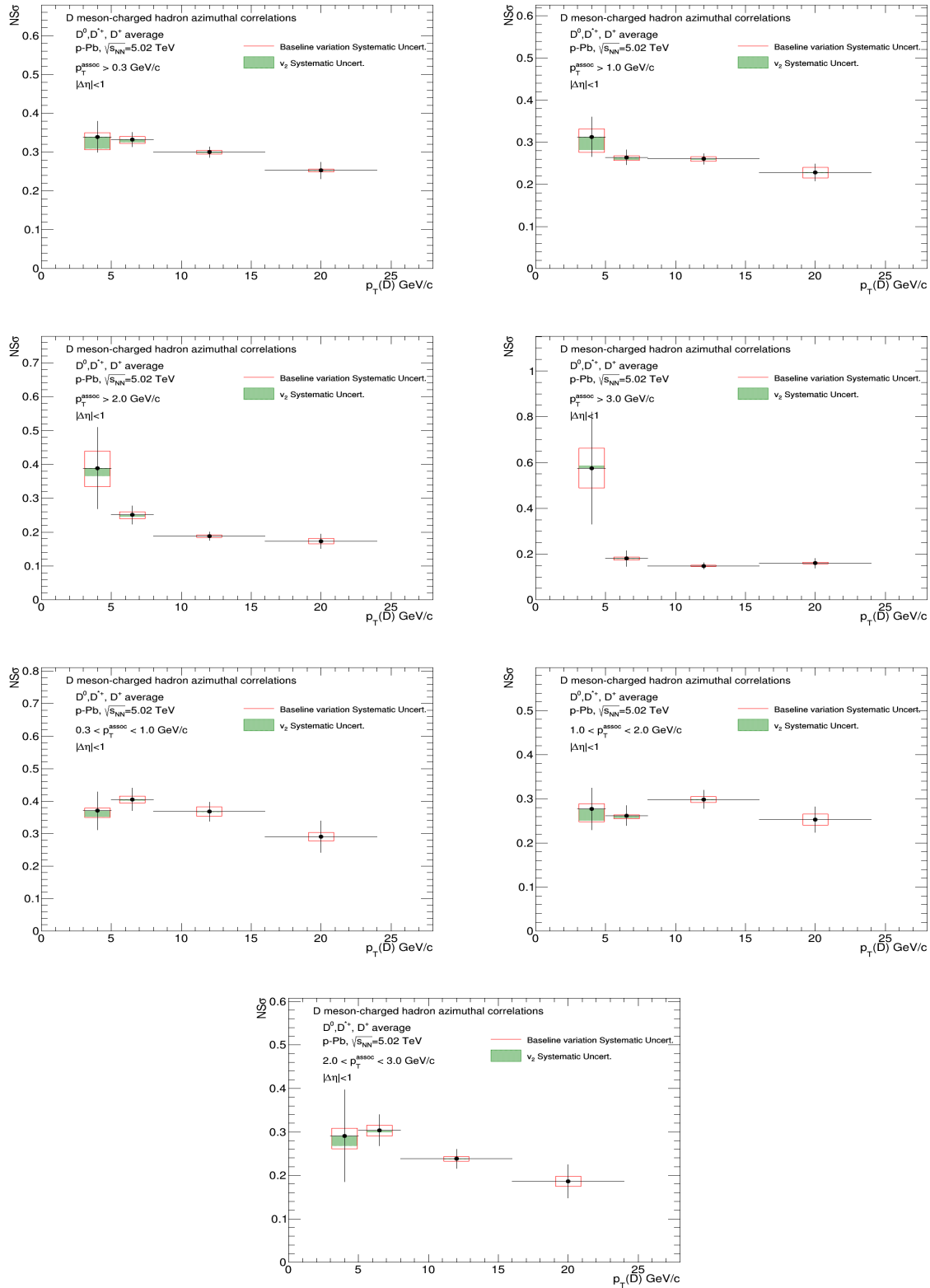


Figure 48: Top panels: near side yield $p_T(D)$ trend for the D-meson average, extracted from fit to the azimuthal correlation distributions, for all the analyzed kinematic ranges of associated track p_T . Bottom panels: for each kinematic region the systematic uncertainties coming from the variation of the fit procedure are shown.



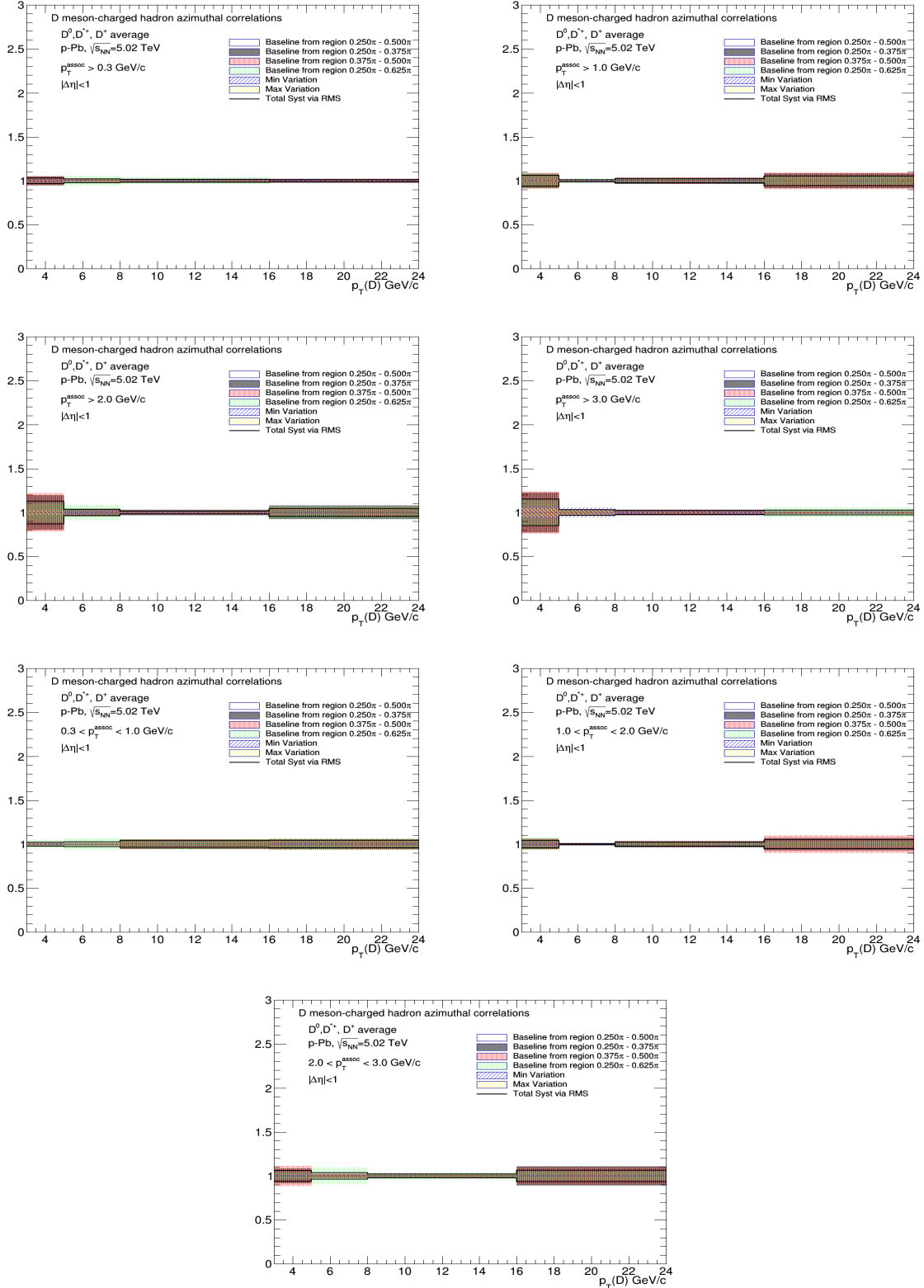
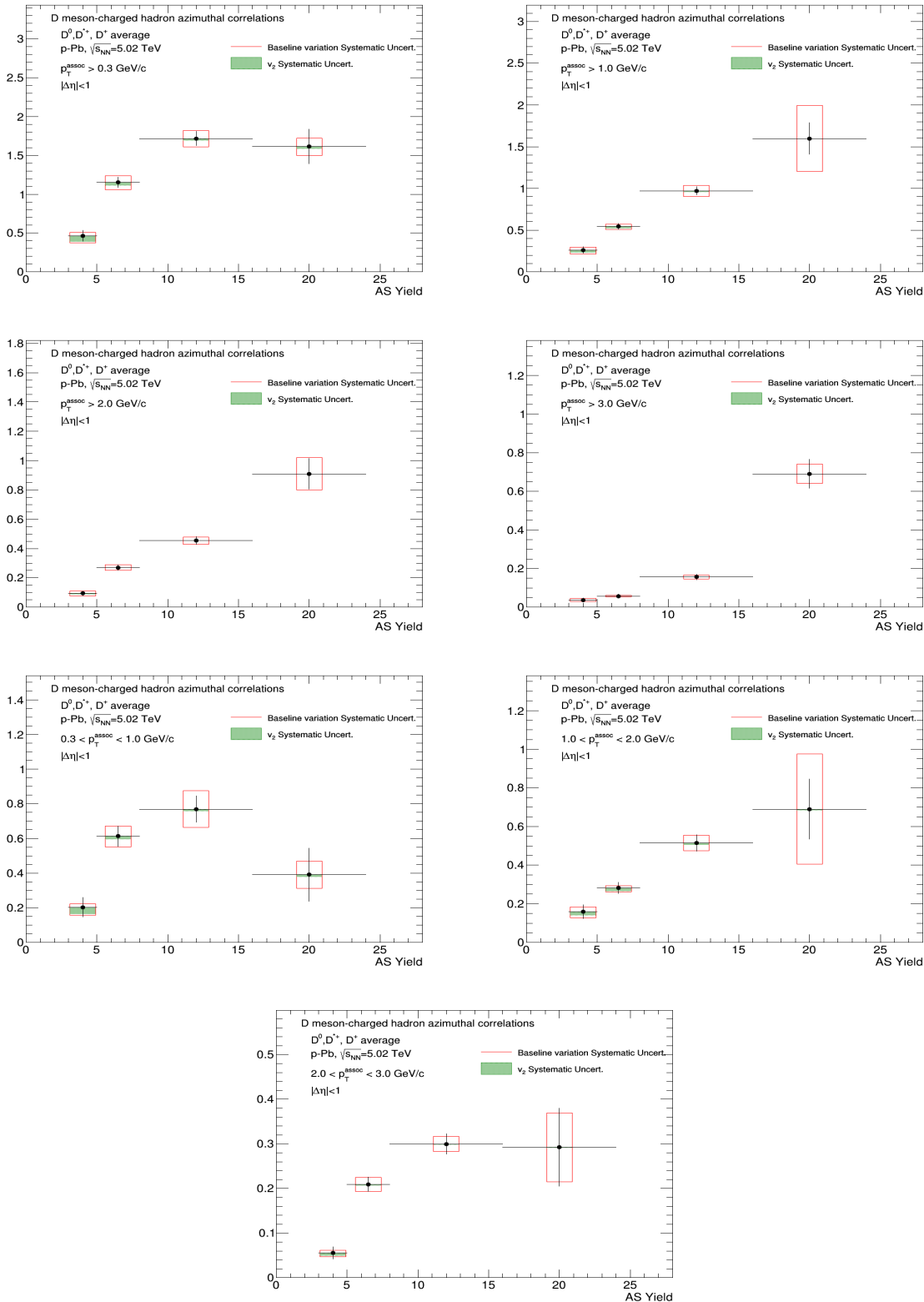


Figure 49: Top panels: near side width $p_T(D)$ trend for the D-meson average, extracted from fit to the azimuthal correlation distributions, for all the analyzed kinematic ranges of associated track p_T . Bottom panels: for each kinematic region the systematic uncertainties coming from the variation of the fit procedure are shown.



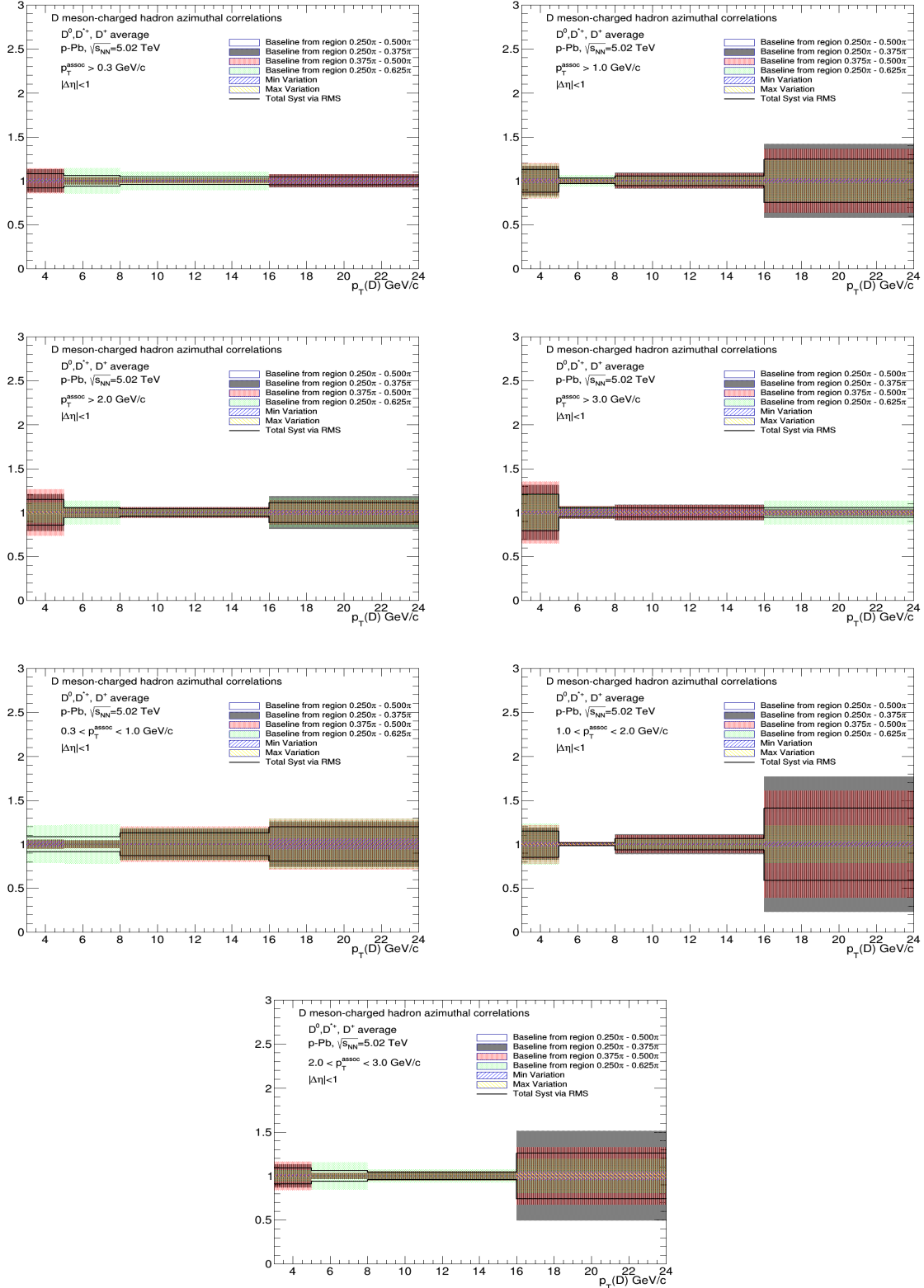
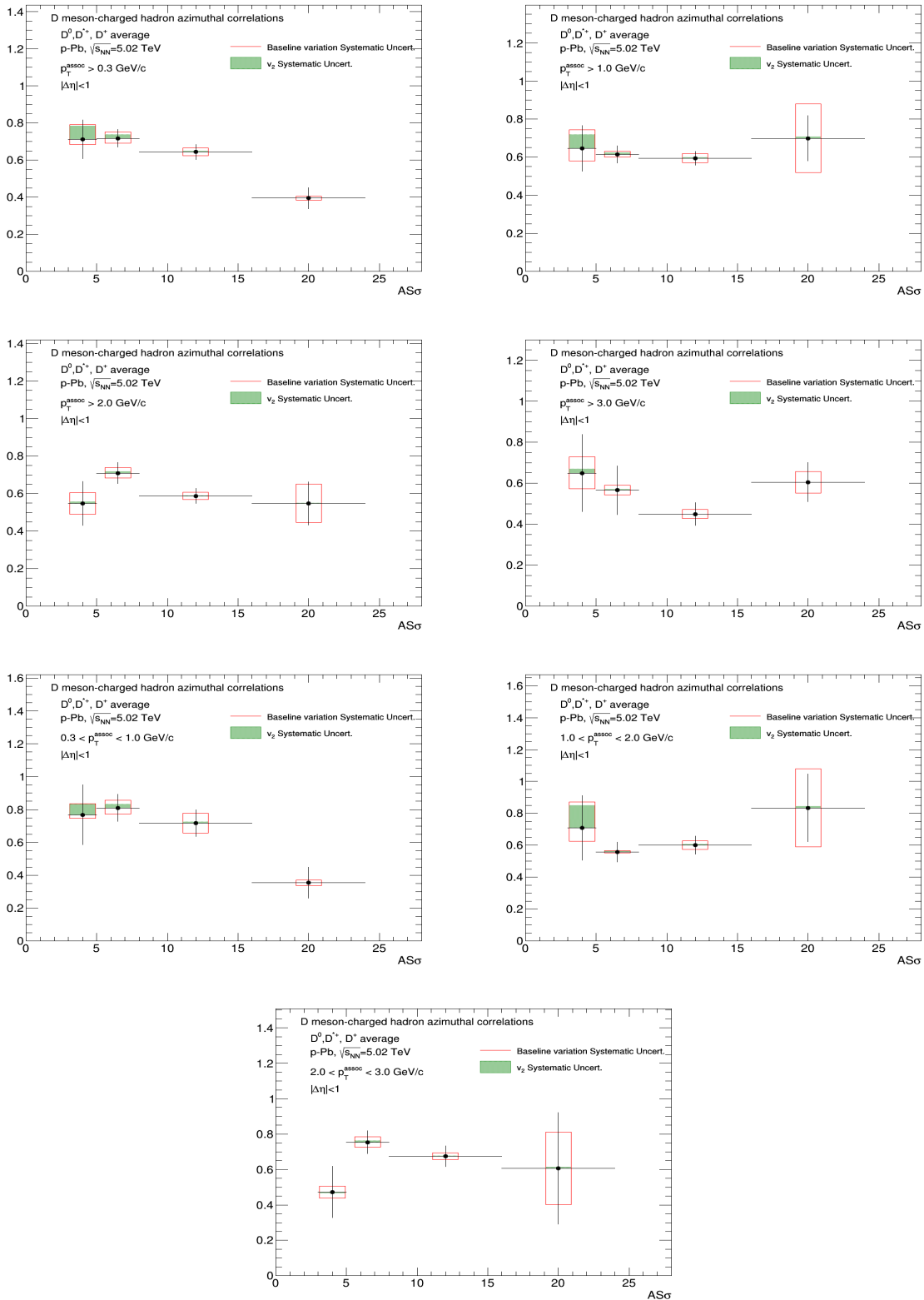


Figure 50: Top panels: away side yield $p_T(D)$ trend for the D-meson average, extracted from fit to the azimuthal correlation distributions, for all the analyzed kinematic ranges of associated track p_T . Bottom panels: for each kinematic region the systematic uncertainties coming from the variation of the fit procedure are shown.



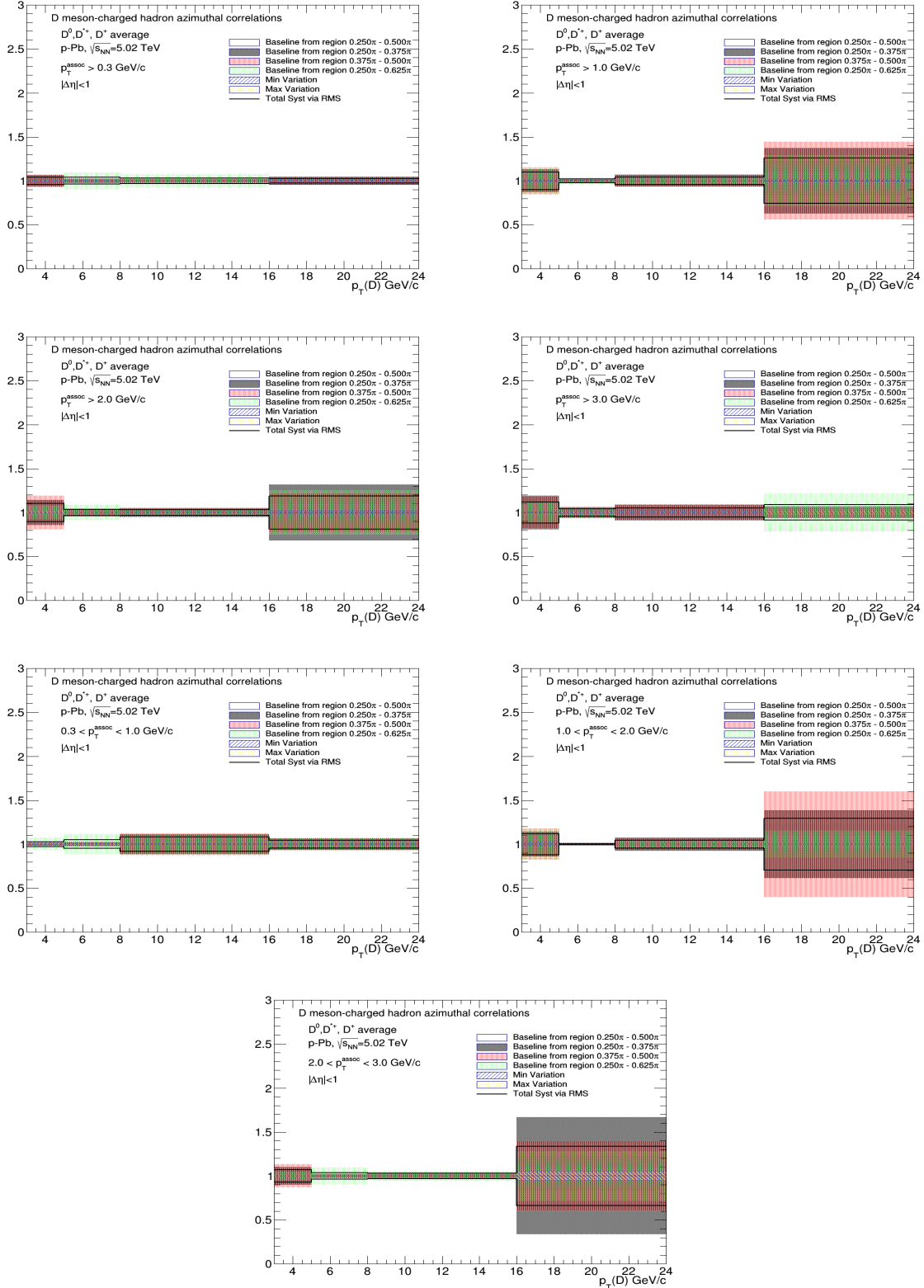
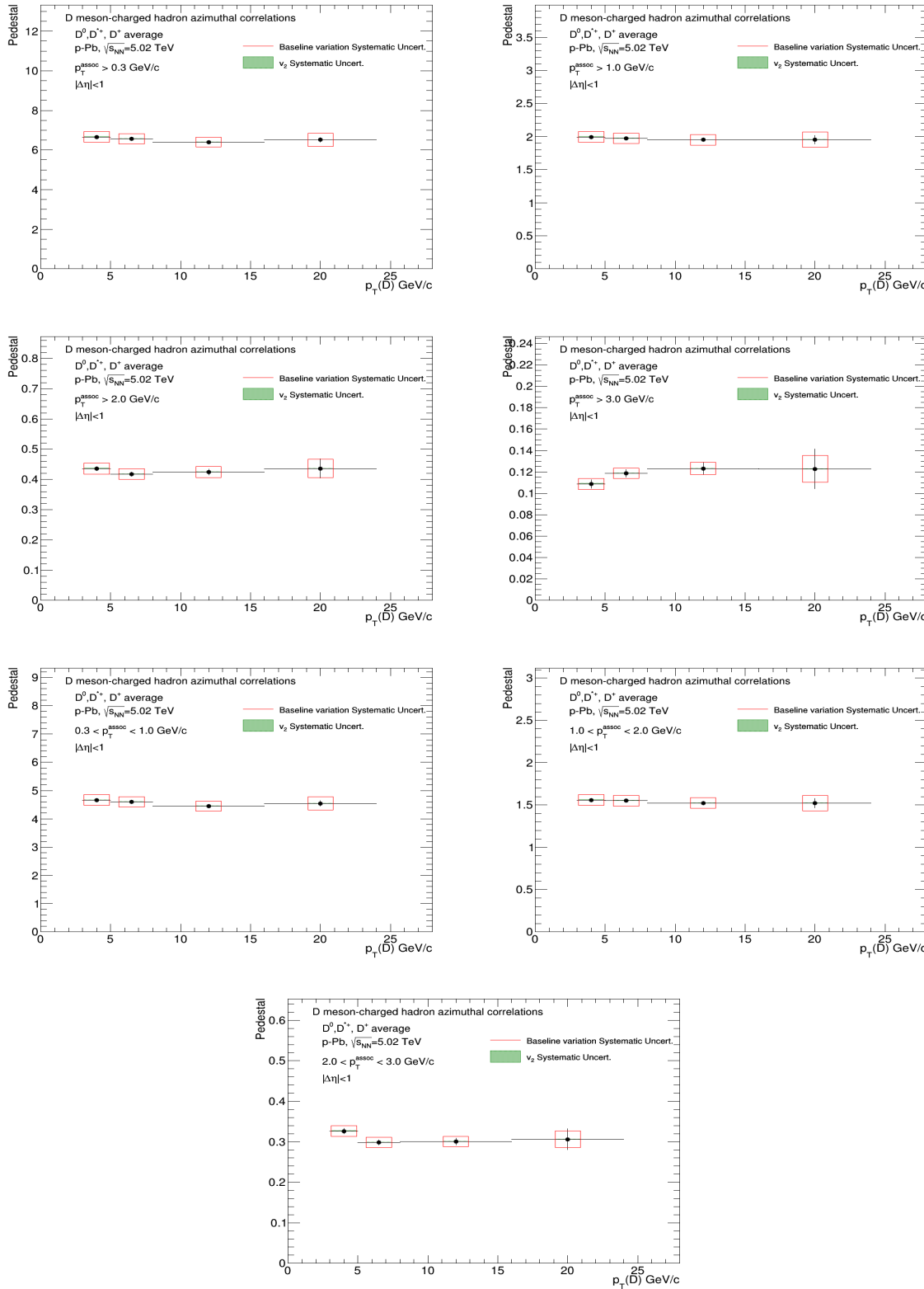


Figure 51: Top panels: away side width $p_T(D)$ trend for the D-meson average, extracted from fit to the azimuthal correlation distributions, for all the analyzed kinematic ranges of associated track p_T . Bottom panels: for each kinematic region the systematic uncertainties coming from the variation of the fit procedure are shown.



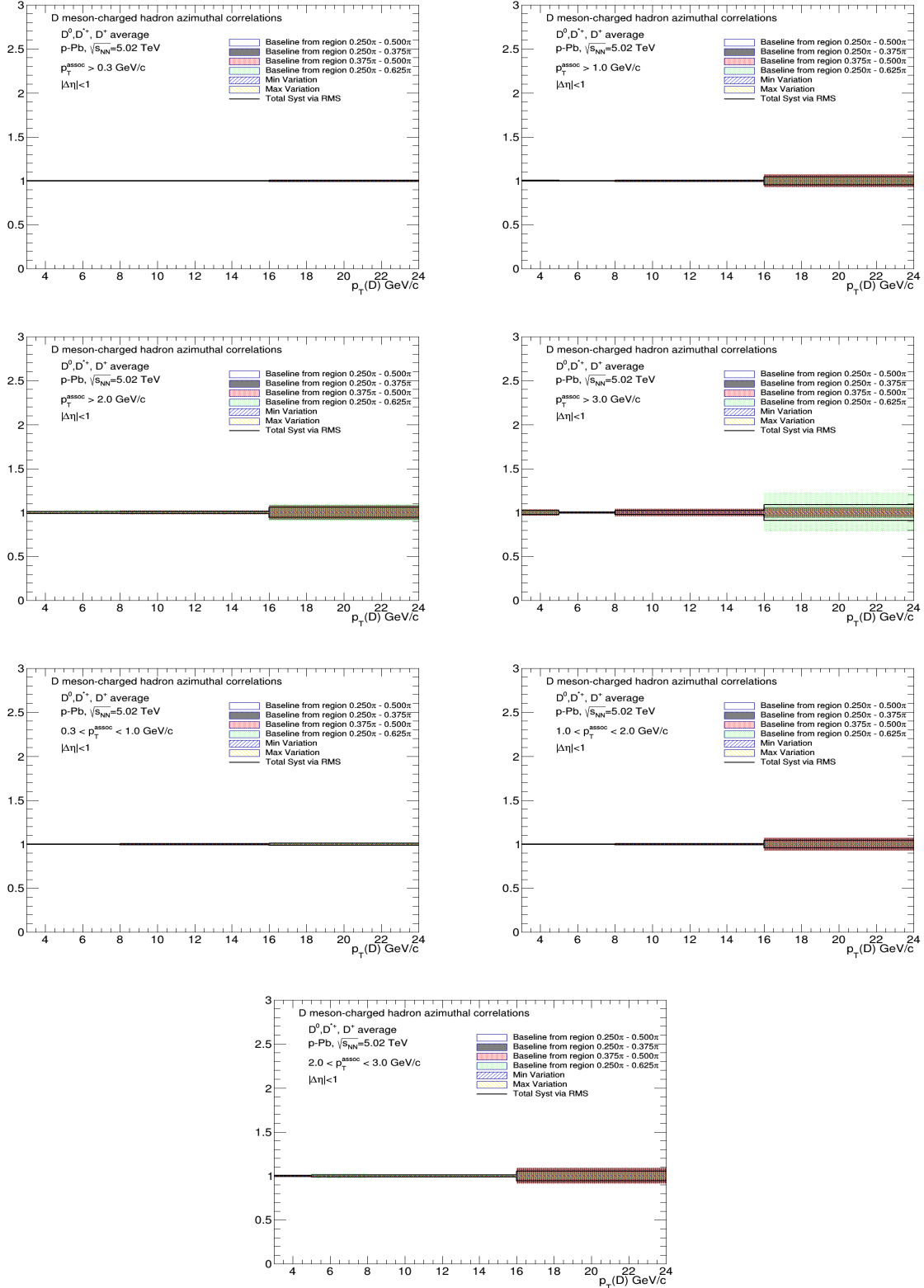


Figure 52: Top panels: baseline height trend for the D-meson average, extracted from fit to the azimuthal correlation distributions, for all the analyzed kinematic ranges of associated track p_T . Bottom panels: for each kinematic region the systematic uncertainties coming from the variation of the fit procedure are shown.

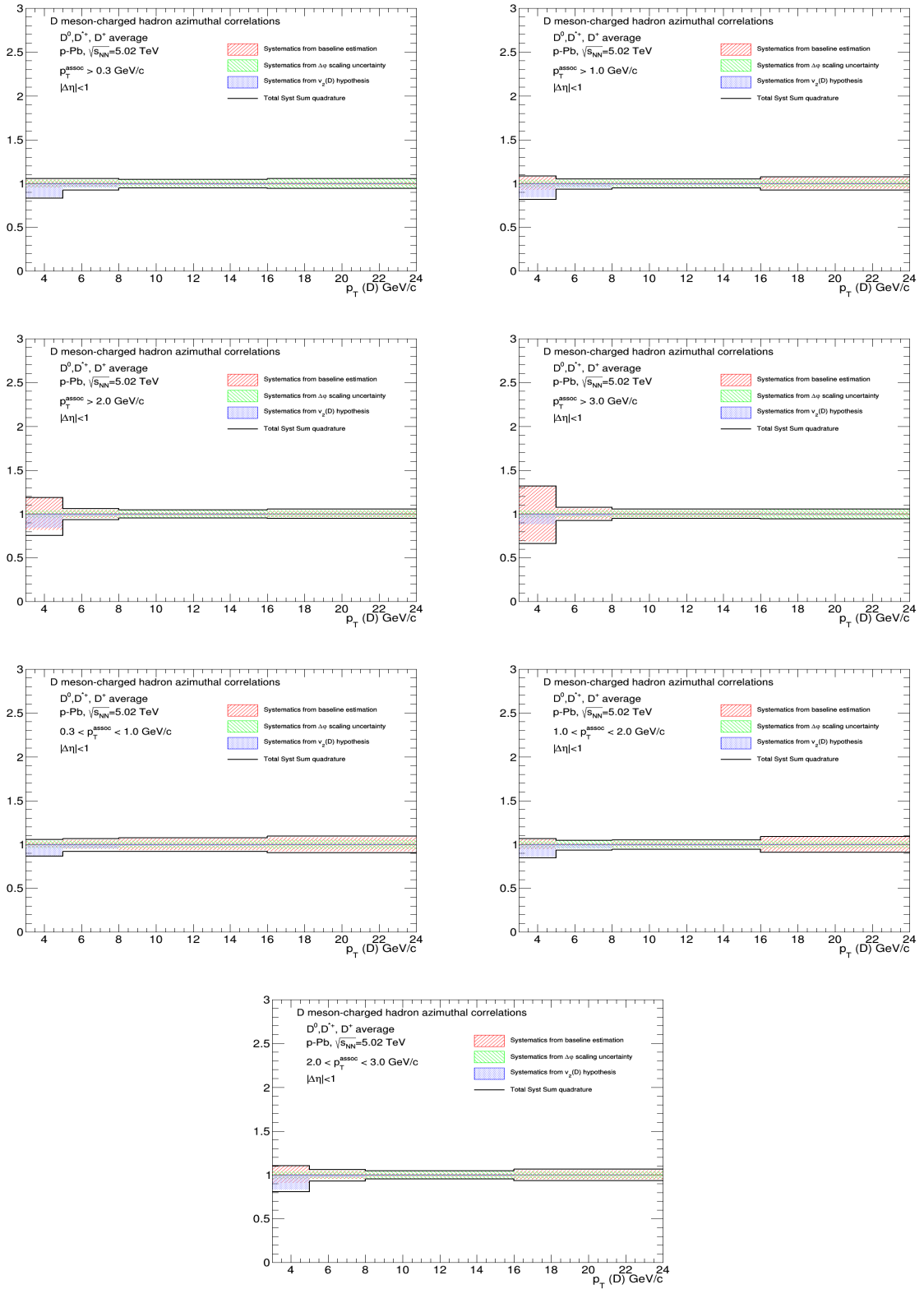


Figure 53: Total systematic uncertainty, and its components, for near-side yields in the different kinematic ranges analyzed

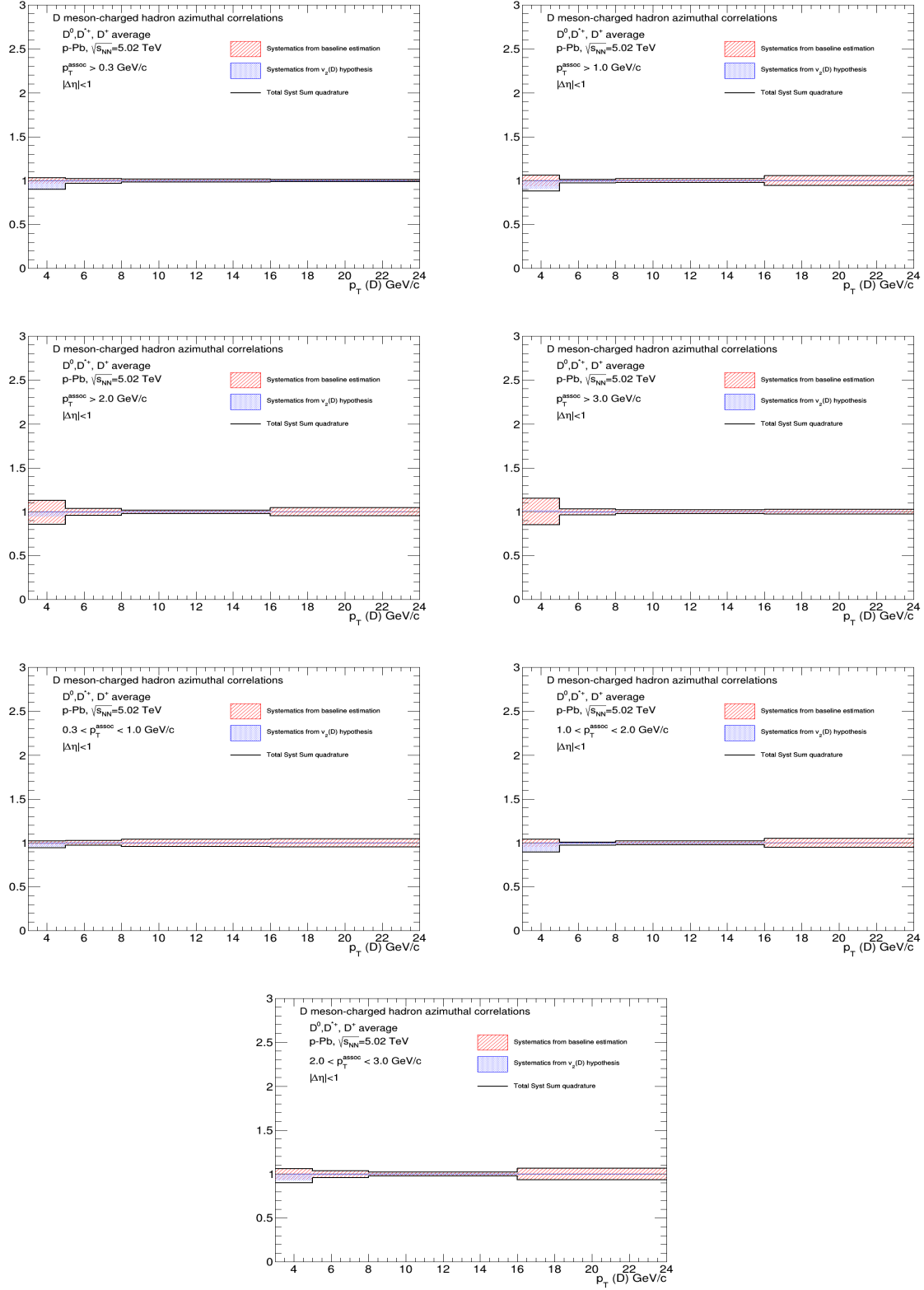


Figure 54: Total systematic uncertainty, and its components, for near-side sigma in the different kinematic ranges analyzed

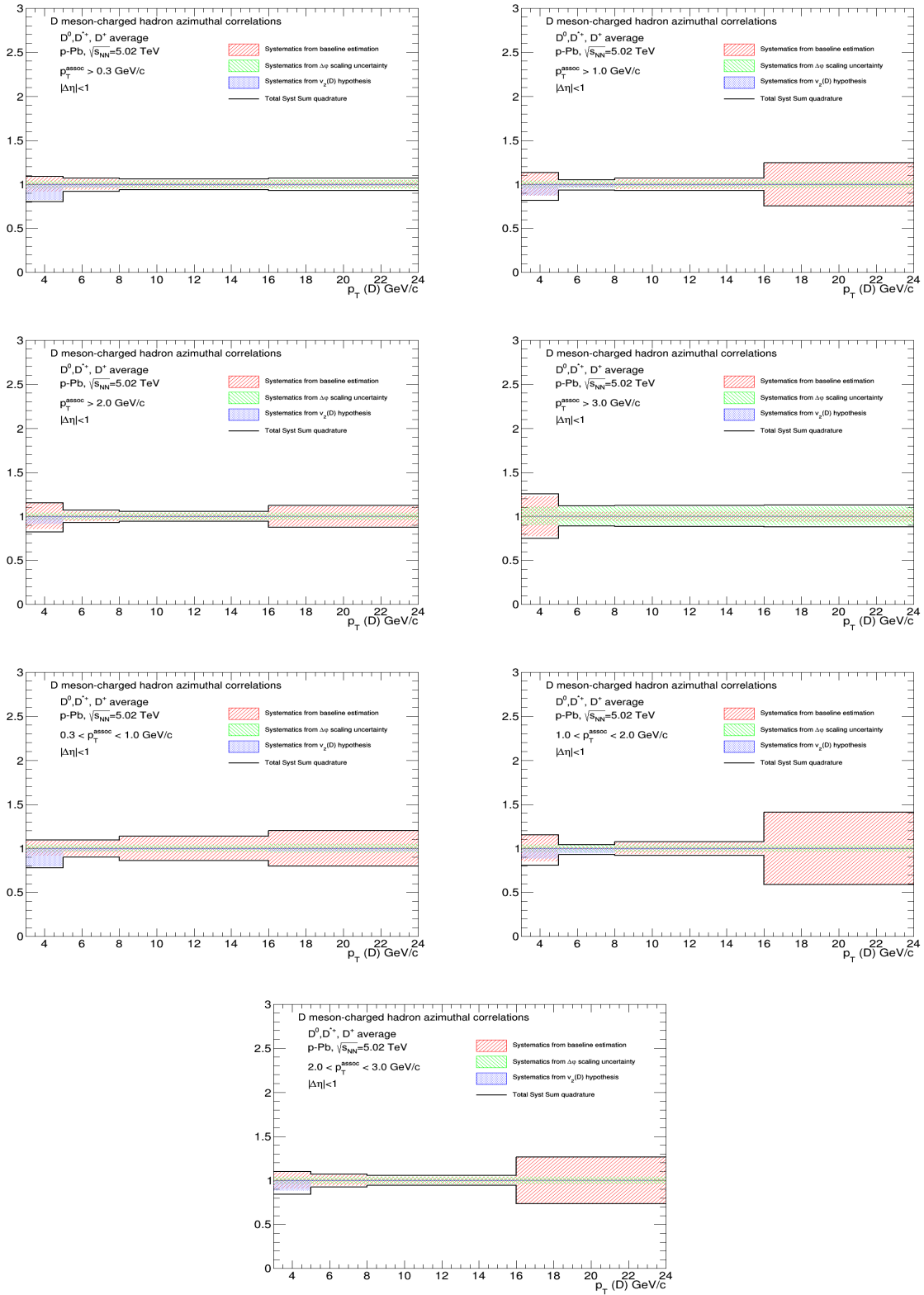


Figure 55: Total systematic uncertainty, and its components, for away-side yields in the different kinematic ranges analyzed

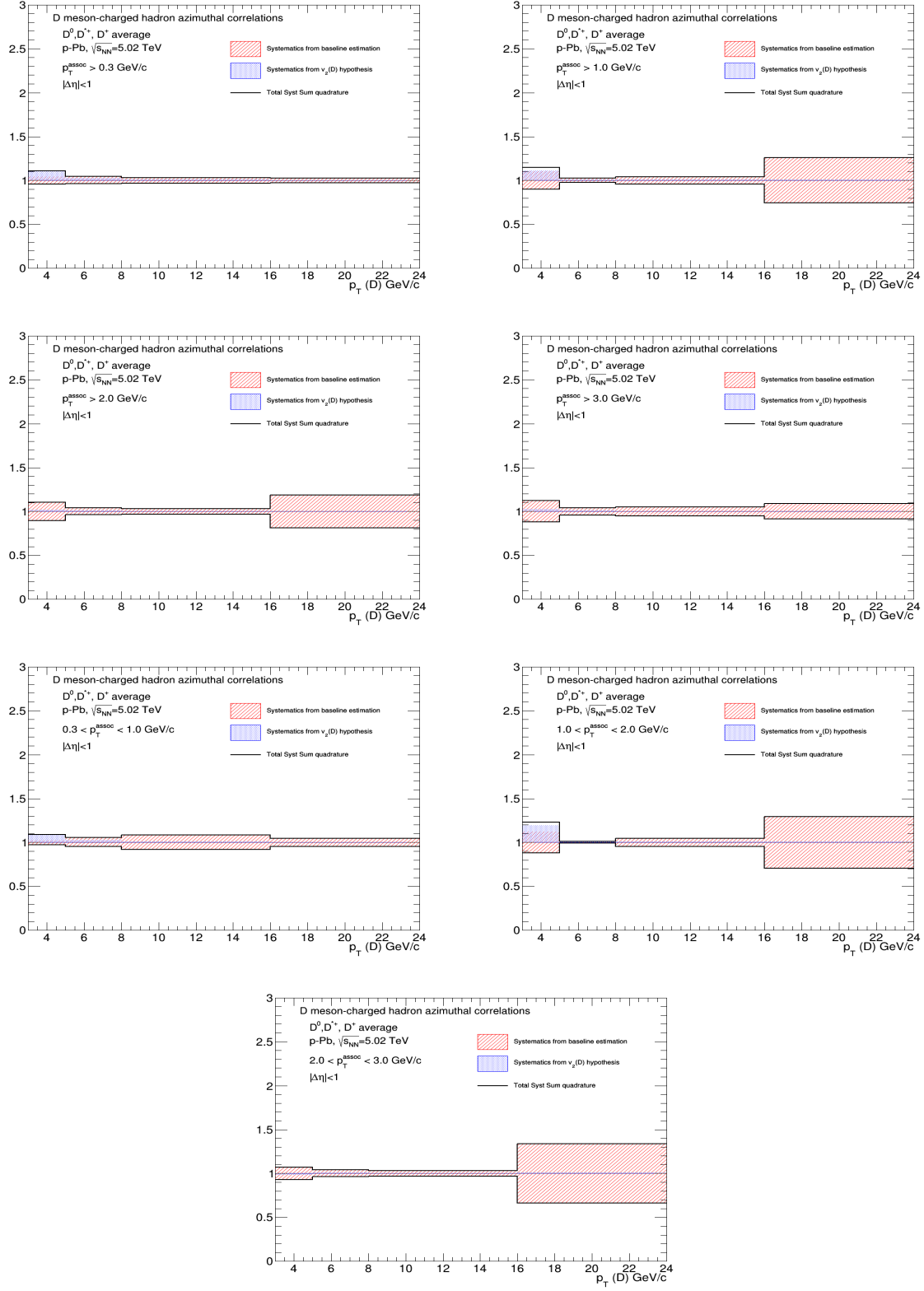


Figure 56: Total systematic uncertainty, and its components, for away-side sigma in the different kinematic ranges analyzed

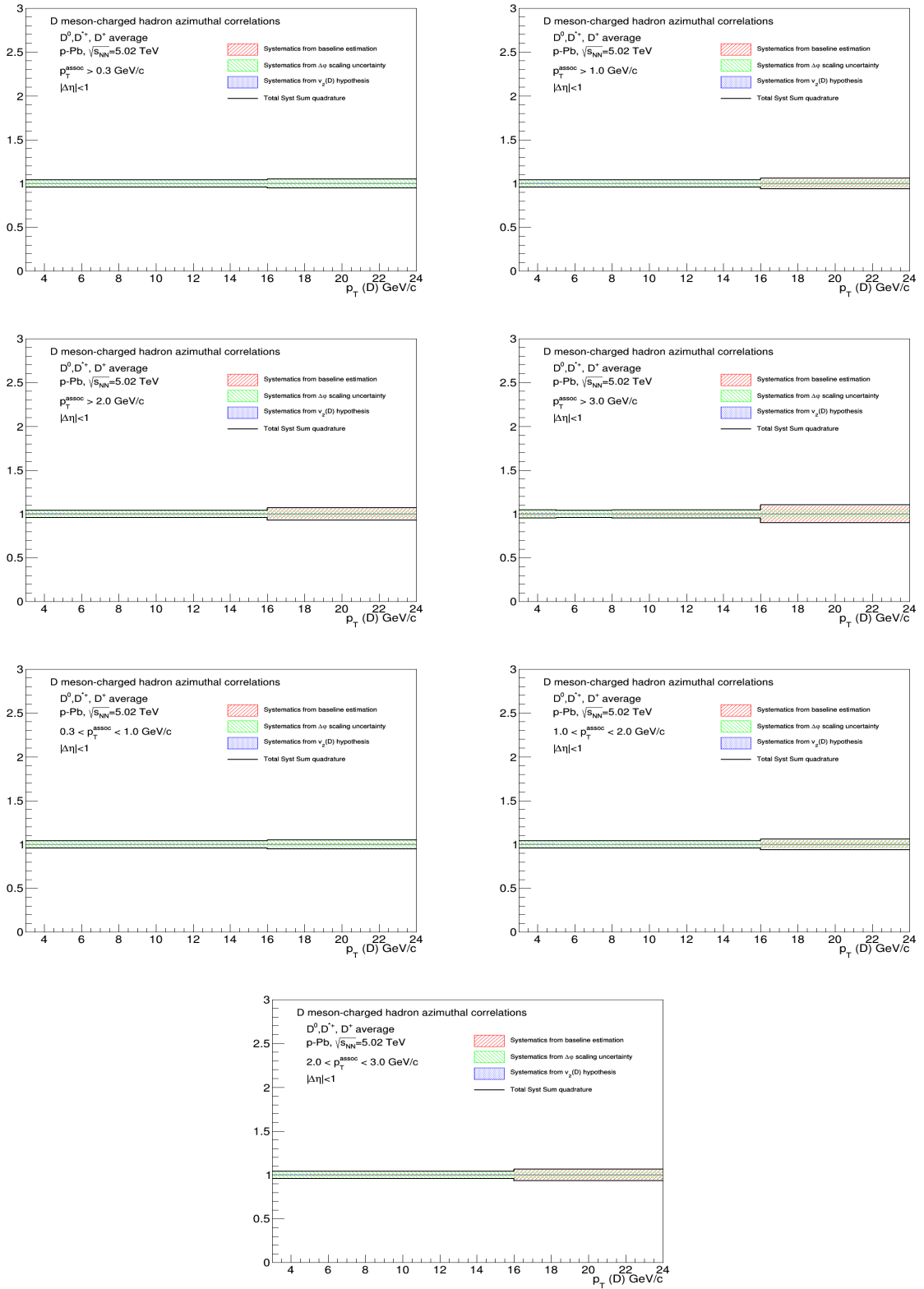


Figure 57: Total systematic uncertainty, and its components, for baseline heights in the different kinematic ranges analyzed.

715 5.4 Comparison of 2016 p-Pb and 2013 p-Pb results

716 In Figure 58, the average correlation distributions from the published analysis in p-Pb 2013 sample
 717 (black points) and the new p-Pb 2016 sample (red points), both at 5 TeV, are compared. As it's evident,
 718 the statistical and systematic uncertainties are largely reduced in the new data sample. The feature of
 719 the correlation distributions are the same in both systems, and an overall compatibility of the points is
 720 observed. Only in the near-side region, the 2016 data points have a tendency of being slightly below the
 721 2013 data points. In part, this can be partially explained with the different procedure for assessing the
 722 B to D decay topology bias (2016 data corrected, with a slight downward shift for the first two points,
 723 while for 2013 data only a downward systematic uncertainty was applied.

724 Figure 59 shows the same comparison for the fit observables. Also in this case the uncertainties are
 725 largely reduced for the 2016 analysis. While the away side features are compatible (but with large
 726 uncertainties) and the near-side widths are on top of each other, for the near-side yields a slight decrease
 727 of the 2016 results is observed (though well within the uncertainty). This is a direct consequence of
 728 the feature just observed in the comparison of the near-side peak point of the azimuthal correlation
 729 distributions (i.e. that the 2016 data points are slightly lower than the 2013 ones).

730 5.5 Comparison of 2016 p-Pb and 2010 pp results

731 Figure 60 shows the comparison of the average D-h correlation distributions in pp 2010 data sample at
 732 $\sqrt{s} = 7$ TeV (published in [4]) and in the new p-Pb 2016 sample at $\sqrt{s_{\text{NN}}} = 5.02$ TeV. The results are
 733 shown after the subtraction of the baseline. The precision of the new p-Pb results is much better than that
 734 of pp results; the correlation distributions show very similar features in the two collision systems.

735 In Figure 61 the comparison is performed for the near-side peak observables, again in the common
 736 kinematic ranges, where the same consideration about the uncertainties holds. The similarity of the
 737 correlation distributions is reflected also in the near-side yield and width values, which do not seem to
 738 differ within the uncertainties, pointing to the absence of strong effects from cold-nuclear matter effects
 739 on the correlation distributions.

740 It has to be said that, on the base of a study performed with Pythia6-Perugia2011 simulations, a scaling
 741 factor of about 0.93 is expected when passing from a center-of-mass energy of $\sqrt{s} = 7$ TeV to $\sqrt{s} = 5$
 742 TeV, difficult to be appreciated with the current uncertainties, especially the pp ones.

743 5.6 Comparison of 2016 p-Pb and model expectations

744 A comparison of the average D-h correlation distributions on the new p-Pb data samples with expec-
 745 tations from Monte Carlo simulations (currently Pythia6-Perugia2011, Pythia6-Perugia2010, Pythia6-
 746 Perugia0, PYTHIA8; POWHEG+PYTHIA and EPOS 3 will be added if they come in time) is shown in
 747 Figure 62, after the baseline subtraction (which differs strongly between data and simulations, due to he
 748 very different underlying event). The simulations, though being for pp, include the boost of the center-
 749 of-mass along the beam axis present in p-Pb collisions and nuclear PDF. The shape of the correlation
 750 distributions is well reproduced by all the models, together with their p_T trend and with the evolution of
 751 the correlation peaks.

752 Figures 63 and 64 show the same comparison for the fit observables (peak yields and widths for near-side
 753 and away-side, respectively), for all the addressed p_T ranges.

754 5.7 Planned results for SQM approvals

755 We are planning to approve the following results, all shown in the previous figures (the final graphical
 756 style of the plots is still to be finalized):

- 757 – Average D-h correlation distributions, in exemplary p_T range

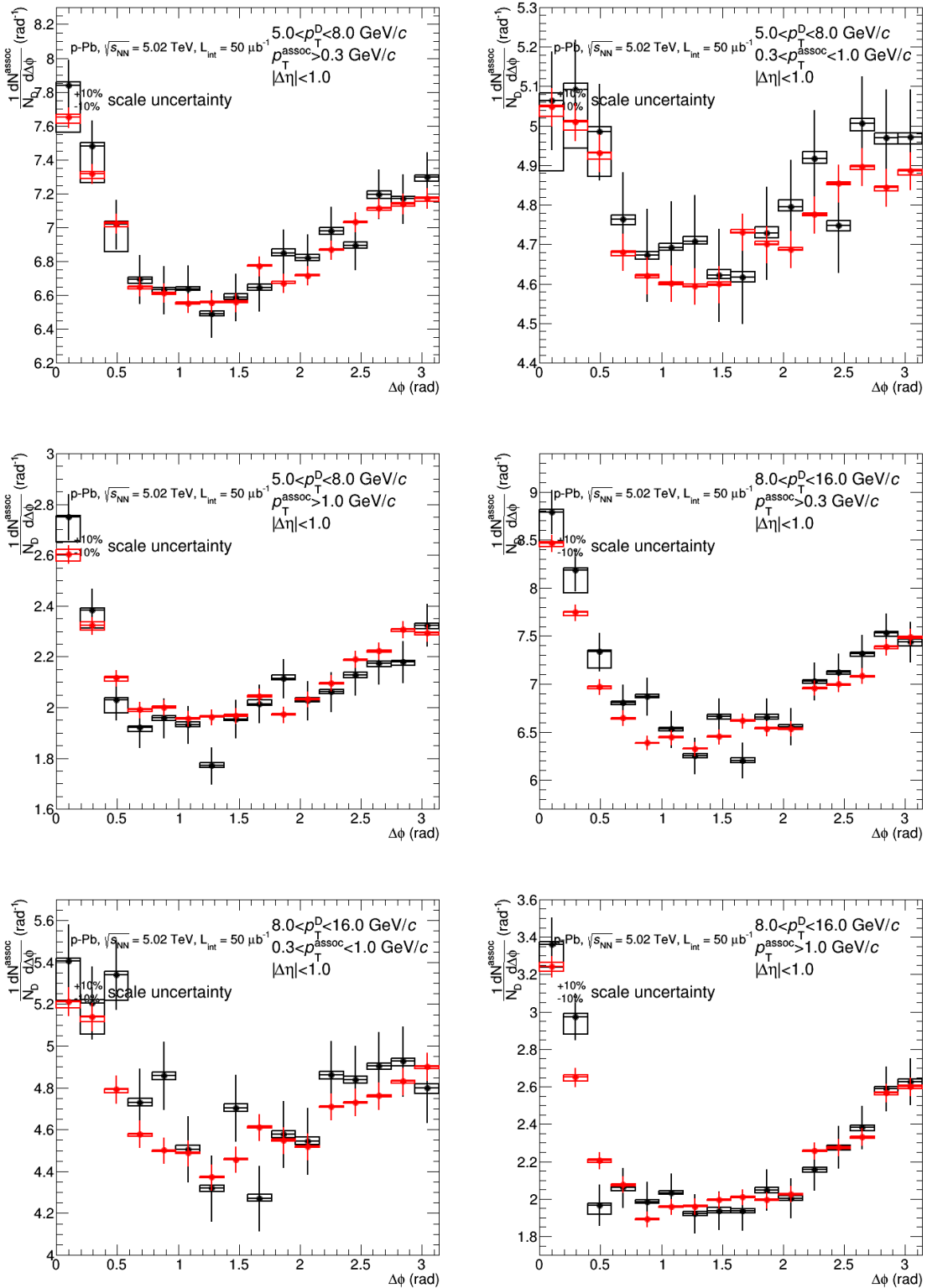


Figure 58: Comparison of 2016 (red) and 2013 (black) results for azimuthal correlation distributions, for the common p_T ranges.

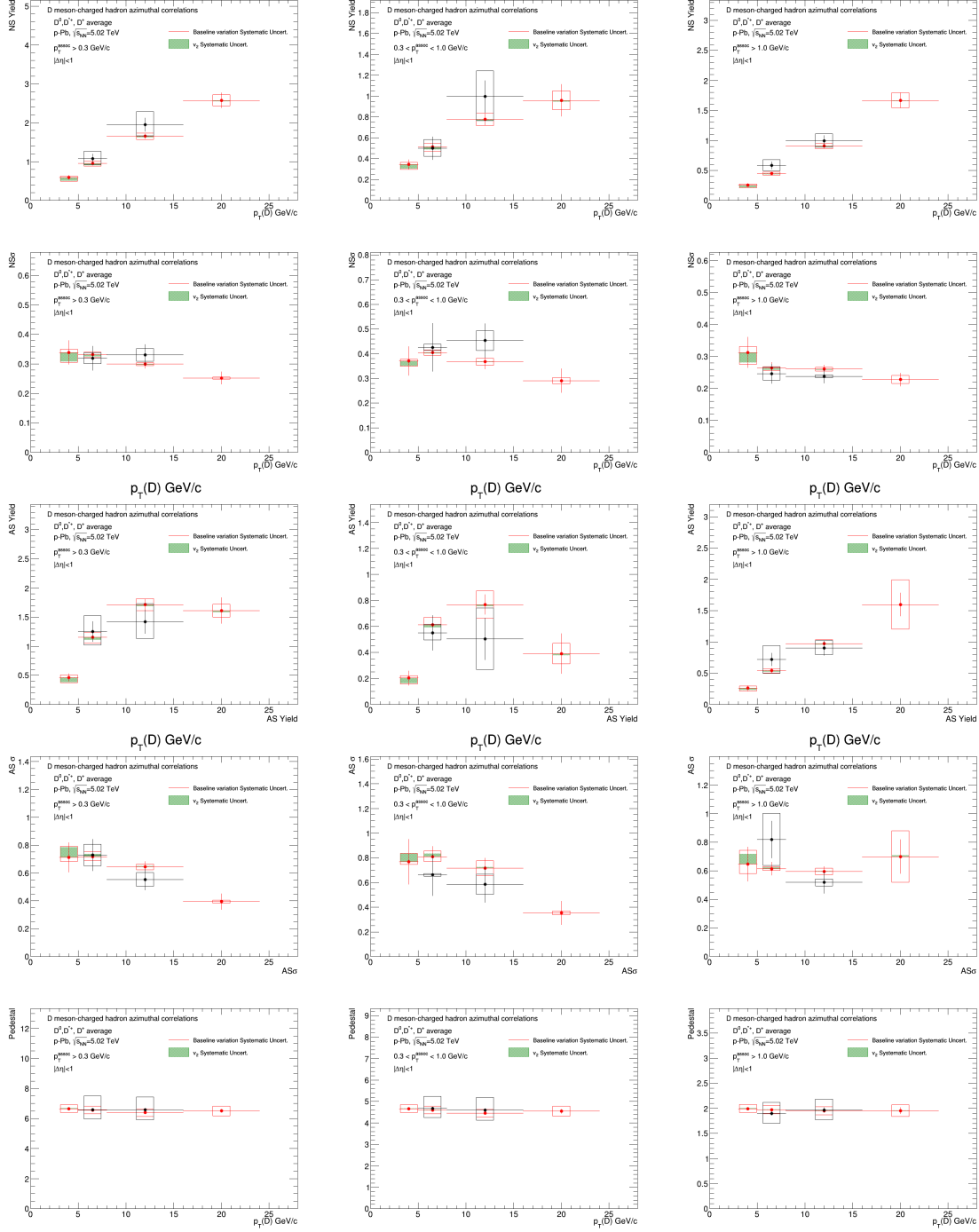


Figure 59: Comparison of the average D-h azimuthal correlation properties between 2016 p-Pb (red) and 2013 p-Pb (black) data analysis, for the common p_T ranges of D meson and associated particles.

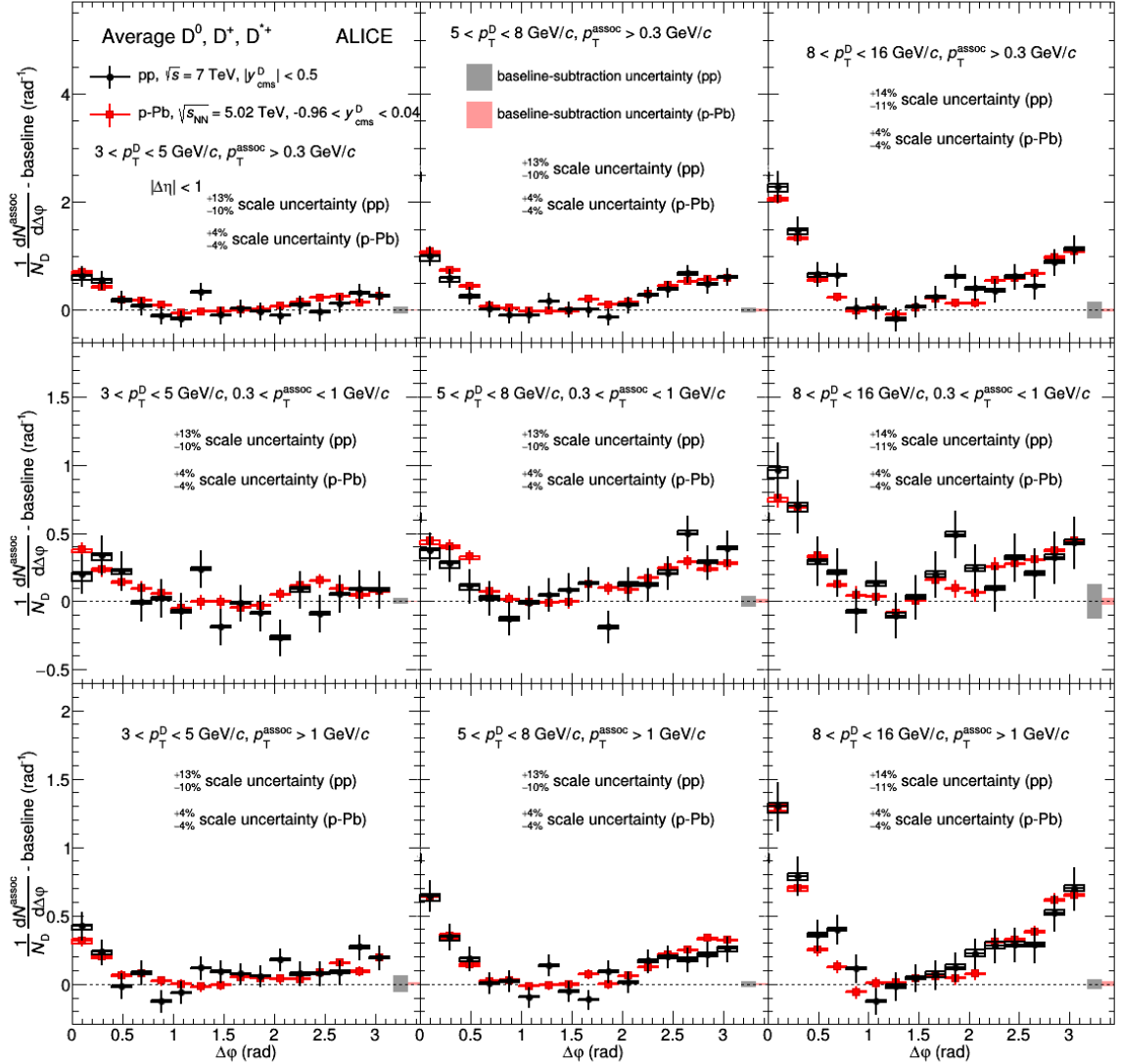


Figure 60: Comparison of pp 2010 (black) and p-Pb 2016 (red) average D-h azimuthal correlation distributions, for the common p_T ranges.

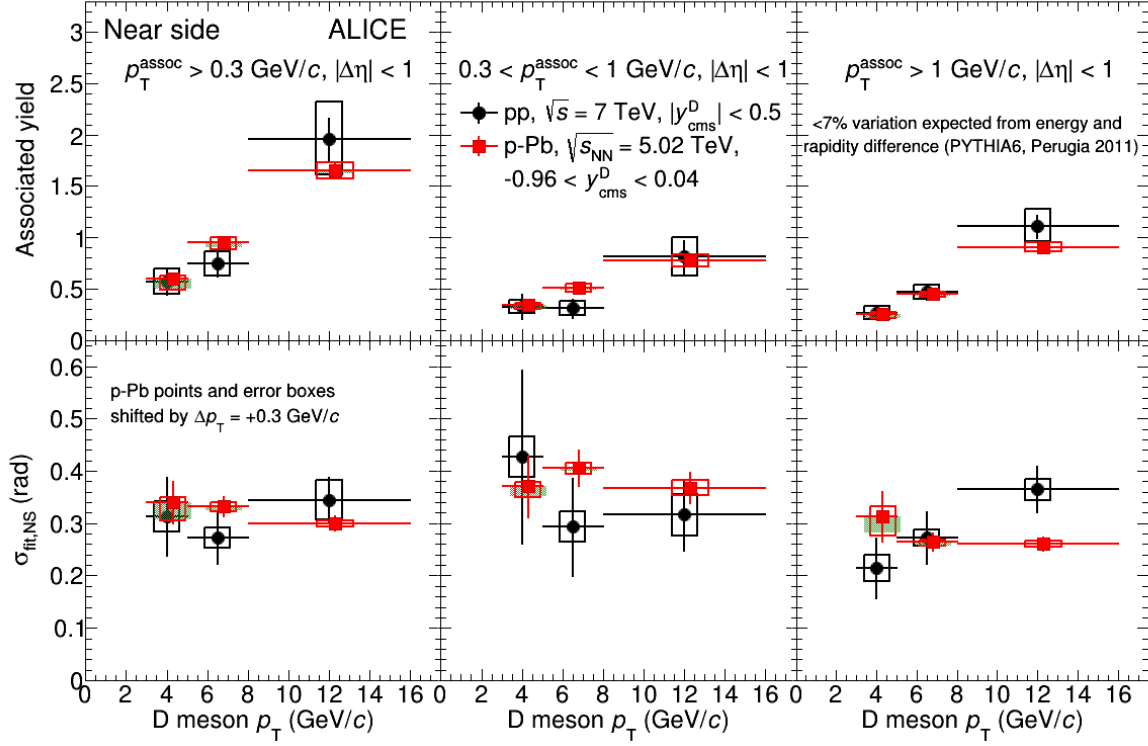
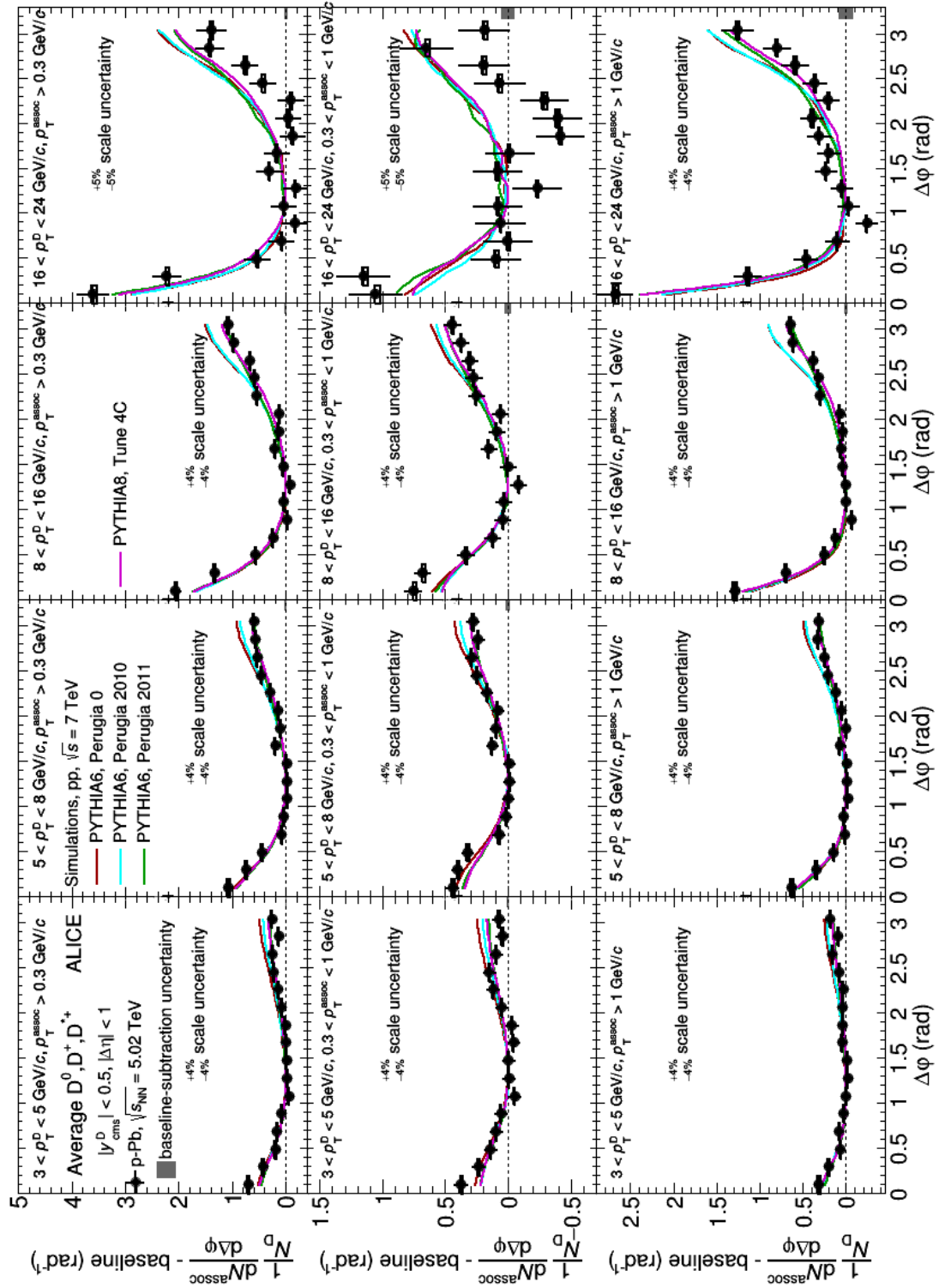


Figure 61: Comparison of pp 2010 (black) and p-Pb 2016 (red) near-side peak yields and widths, for the common p_T ranges.

- 758 – Fit of D-h correlation distributions, in exemplary p_T range
- 759 – $p_T(D)$, $p_T(\text{assoc})$ trend of NS yield, NS width, AS yield, AS sigma
- 760 – Comparison of correlation distributions with expectations from models (PYTHIA6, PYTHIA8, if
761 in time POWHEG, EPOS)
- 762 – Comparison of fit observables with expectations from models (PYTHIA6, PYTHIA8, if in time
763 POWHEG, EPOS)
- 764 – Comparison of correlation distributions with pp 2010 results
- 765 – Comparison of fit observables with pp 2010 results



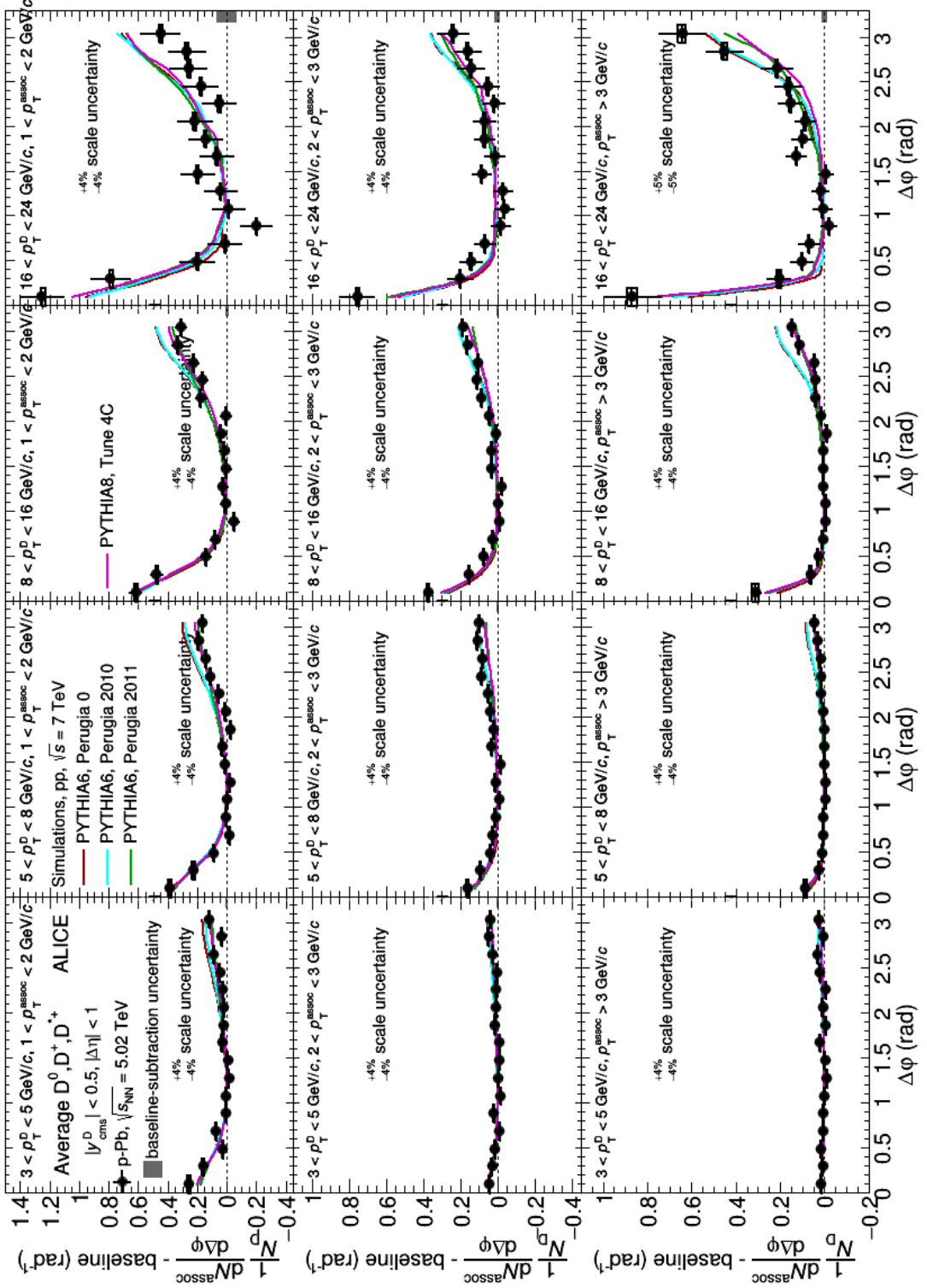
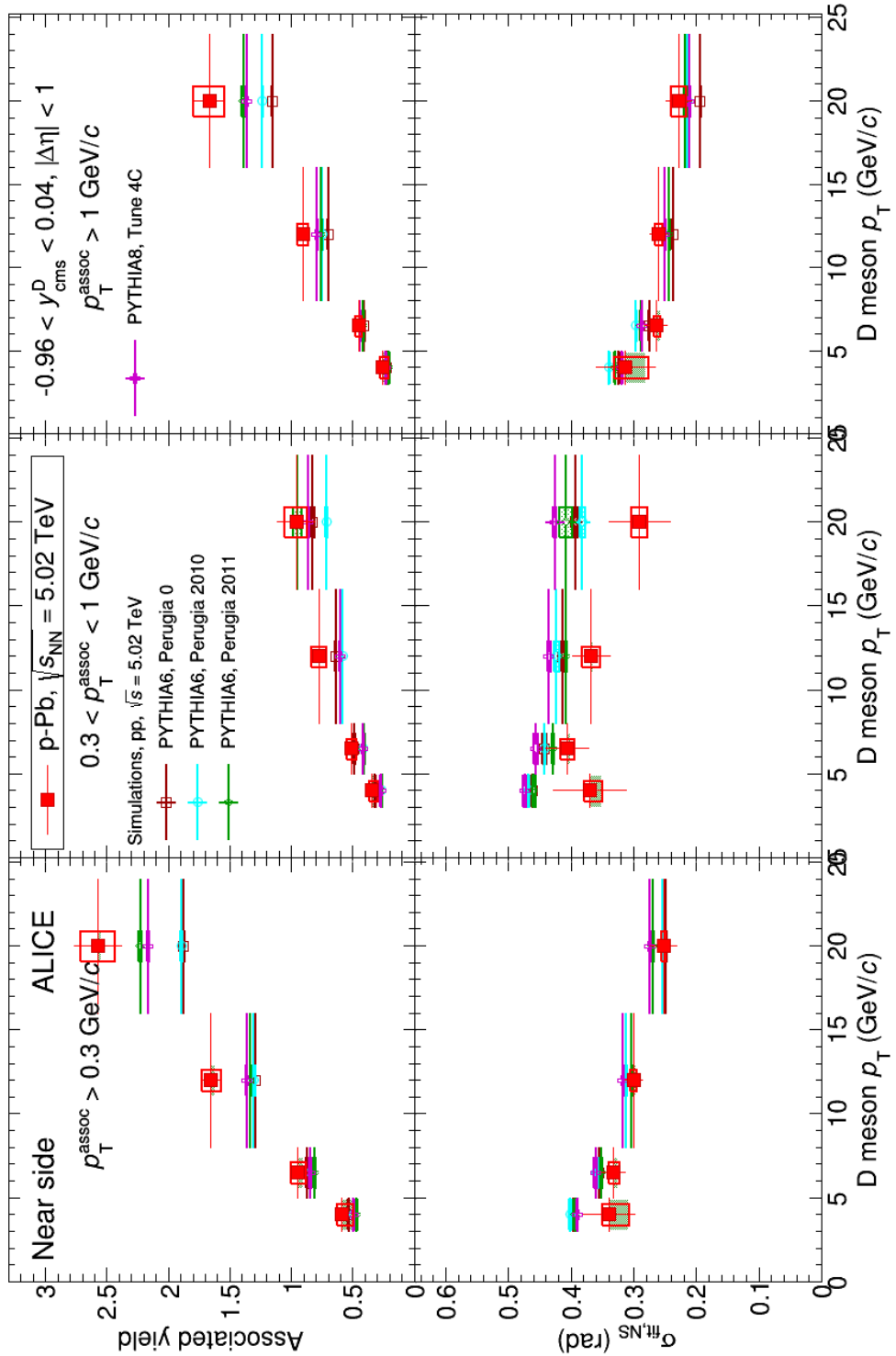


Figure 62: Comparison of p-Pb 2016 average D-h correlation distributions and model expectations, for all the studied kinematic ranges.



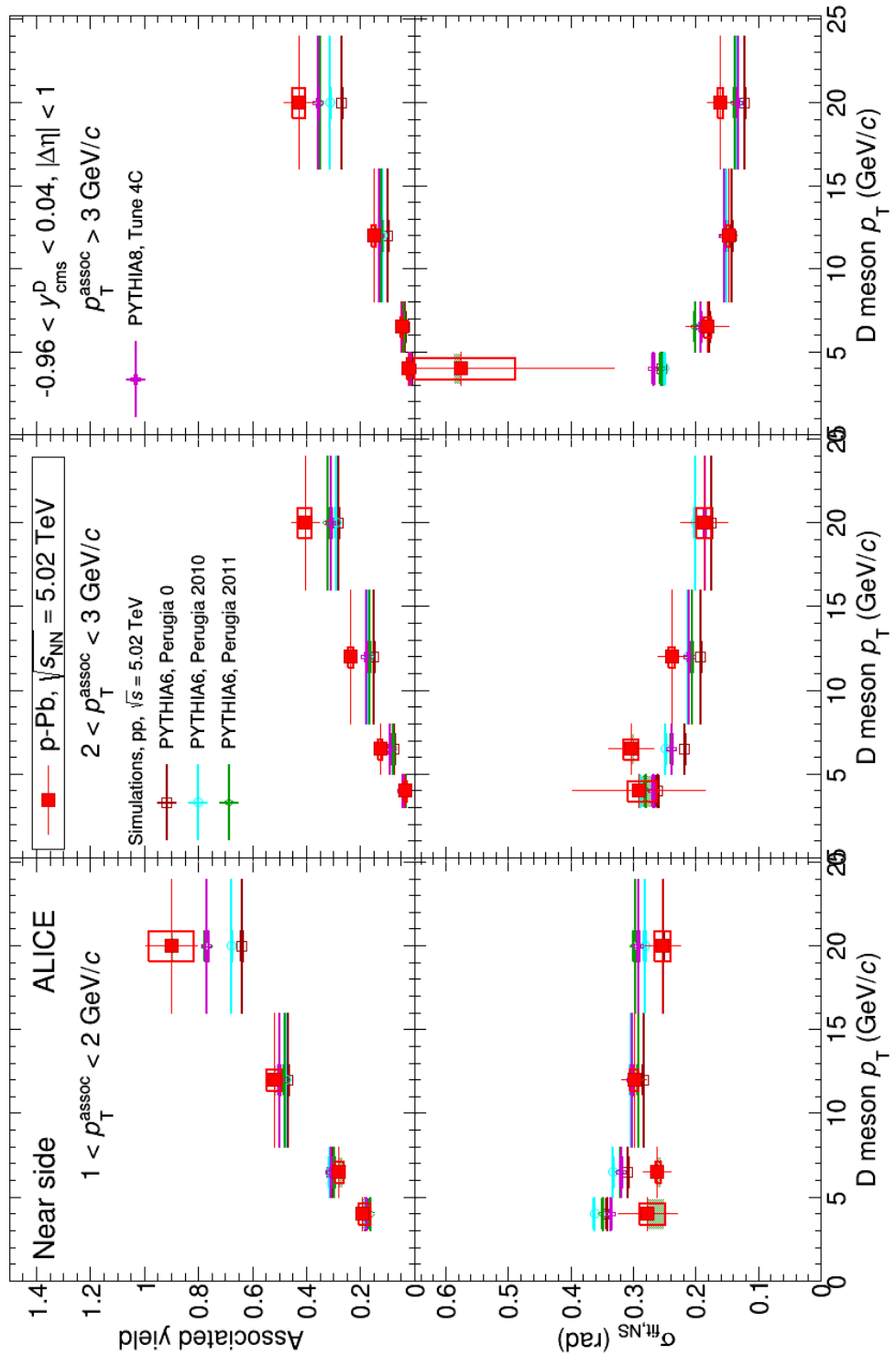
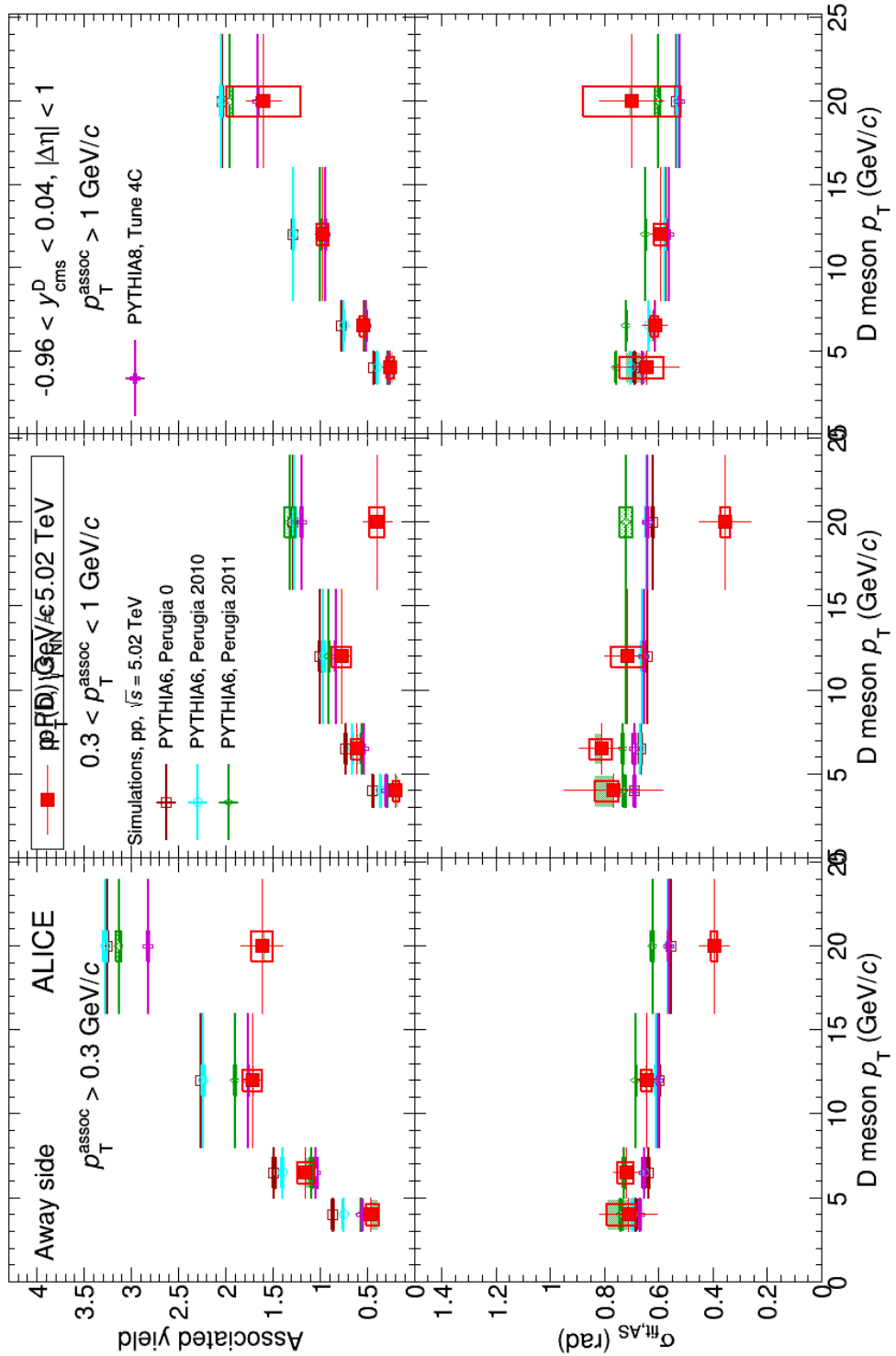


Figure 63: Comparison of near-side peak yields and widths from p-Pb 2016 results and model expectations, for all the studied kinematic ranges.



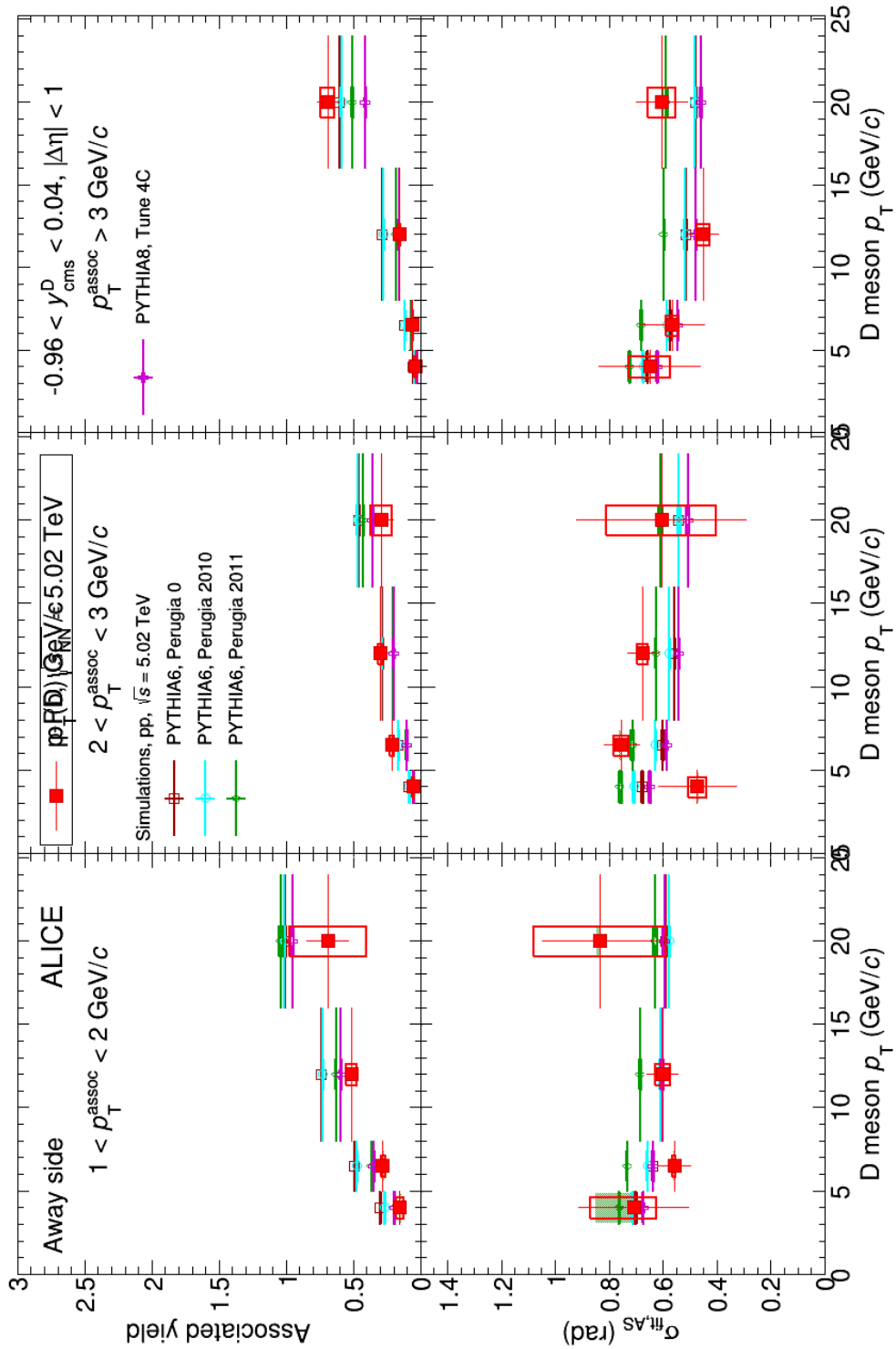


Figure 64: Comparison of away-side peak yields and widths from p-Pb 2016 results and model expectations, for all the studied kinematic ranges.

766 **6 Bibliography**

767 **References**

- 768 [1] ALICE Collaboration, arXiv:1609.06643 [nucl-ex]
769 [2] B. Abelev et al. [ALICE Collaboration], Phys.Lett. B719 (2013) 29-41
770 [3] B. Abelev et al. [ALICE Collaboration], Phys.Lett. B726 (2013) 164-177
771 [4] B. Abelev et al. [ALICE Collaboration], Eur. Phys. J. C (2017) 77:245
772 [5] B. Abelev et al. [ALICE Collaboration], JHEP **01** (2012) 128
773 [6] <https://aliceinfo.cern.ch/Notes/node/238>
774 [7] <https://aliceinfo.cern.ch/Notes/node/300>
775 [8] <https://aliceinfo.cern.ch/Notes/node/201>